


FULL PAPER

Reduced graphene oxide/iron oxide hybrid composite material as an efficient magnetically separable heterogeneous catalyst for transfer hydrogenation of ketones

Samim Sultana¹ | Shreemoyee Bordoloi^{1,2} | Surajit Konwer¹ |
Geetika Borah¹  | Pradip K. Gogoi¹

¹Department of Chemistry, Dibrugarh University, Dibrugarh, 786004 Assam, India

²Department of Chemistry, MDKG College, Dibrugarh, 786004, India

Correspondence

Surajit Konwer, Geetika Borah and Pradip K. Gogoi, Department of Chemistry, Dibrugarh University, Dibrugarh 786004, Assam, India.

Email: surajitkonwer@dibru.ac.in, geetikachem@yahoo.co.in, dr.pradip54@gmail.com

Funding information

UGC-Maulana Azad National Fellowship, Delhi; DST-SERB, India; Sophisticated Test and Instrumentation Centre

Reduced graphene oxide was synthesized and functionalized with FeSO₄·7H₂O to form a reduced graphene oxide/iron oxide hybrid composite. The hybrid composite was extensively characterized using various techniques. Its application for transfer hydrogenation of various ketones was studied. The investigation showed that it serves as a good catalyst for transfer hydrogenation of aromatic and some aliphatic ketones resulting in excellent isolated yields (97–99%) of products. It is magnetically separable showing good reusability. The products were characterized and compared with authentic ones.

KEYWORDS

aliphatic, aromatic, composite, reduced graphene oxide, transfer hydrogenation

1 | INTRODUCTION

Over the last few years, graphene oxide (GO) has been considered as an attractive supporting material for the heterogenization of catalysts because of its high surface area, edge reactivity, excellent thermal, mechanical and electrical properties and chemical stability,^[1] and most significantly GO has a unique two-dimensional structure with numerous oxygen-containing functional groups, i.e. hydroxyl, epoxy, carboxyl and carbonyl groups.^[2] Due to the presence of oxygenated functional groups on the GO surface, they can easily bind with metals and serve as activation sites for the growth of crystals onto the surface of GO.^[3–6] In addition, the combination of GO and metals (like iron) can create new micropores at the interface of both components, which improve the accessibility of reactants to the active sites and therefore reduce the mass-transfer-limitation effects during catalysis.^[5,6]

Furthermore, GO is able to promote the internal electron transfer process in such composites and induce a synergistic effect between both components to improve catalytic activity.^[3,5,7,8]

The combination of reduced GO (rGO) with iron oxide nanocomposites has attracted the interest of the scientific community as promising materials for catalysis because such combination allows adsorption through π - π conjugation. In addition the unique surface properties of rGO allow it to accept electrons to hinder the recombination of photo-induced electrons and holes.^[9] Though iron oxide is a significant transition metal oxide that has been extensively used as a catalyst in various fields, the catalytic activity is not so satisfactory because of aggregation which greatly decreases the surface area. Therefore the intercalation of iron oxide into rGO may solve this problem by enhancing the properties especially in the field of catalysis.^[10]

Transfer hydrogenation of ketones to their corresponding alcohols catalyzed by transition metal complexes is an interesting research area in modern synthetic chemistry. It is a powerful and convenient route for reducing carbonyl compounds without the use of hazardous hydrogen gas or moisture-sensitive hydride reagents under mild reaction condition and hence is considered as an alternative to direct hydrogenation.^[11-16] Nowadays, the synthesis of chiral alcohols, important intermediates for the synthesis of chiral drugs and fine chemicals, is indispensable,^[17] and hence discovering green and effective approaches for the synthesis of chiral alcohols is of great concern, transfer hydrogenation of ketones being one of them. Transfer hydrogenation reactions are environmentally benign and sustainable compared to catalytic hydrogenation reactions (using molecular hydrogen and high pressure) as there is no generation of hazardous wastes at the end of the reaction and the use of suitable hydrogen donors control the reaction rate and selectivity of the reaction.^[18] Commonly used hydrogen donors are formic acid, aqueous sodium formate, azeotropic mixtures of formic acid/triethylamine and 2-propanol,^[19] but 2-propanol is mostly used as hydrogen donor because it is inexpensive, safe, non-toxic and environment friendly.^[20] Generally, in academic and industrial operations, noble, precious and highly toxic metals such as Pd,^[21] Rh,^[22,23] Ru^[17,24-29] and Ir^[30] are typically used for transfer hydrogenation reactions. Therefore, in recent years, transfer hydrogenation reactions using abundant and environmentally benign metals such as Fe, Co, Ni, etc., replacing the precious and highly toxic metals are gaining much attention.^[31] Transfer hydrogenation reactions of ketones using Fe,^[32] Mn^[33] and Mo^[34] have also been reported.

Hence, in continuation of our previous work on heterogeneous catalysis,^[32,35] we are interested in developing a simple, environmentally benign protocol for transfer hydrogenation of ketones catalyzed by such eco-friendly and nontoxic metals. Herein, we report the synthesis and characterization of rGO/iron oxide hybrid composite material and its application in transfer hydrogenation of ketones.

2 | EXPERIMENTAL

2.1 | Materials

Chemical reagents such as sulfuric acid (H₂SO₄, 98%), sodium nitrate (NaNO₃), potassium permanganate (KMnO₄, 99.9%), hydrogen peroxide (H₂O₂, 30%), iron(II) sulfate (FeSO₄·7H₂O, 99.5%) and ammonium

hydroxide (NH₄OH, 25%) were of analytical reagent grade and used as received. Graphite flakes were purchased from Shanker Graphites and Chemical, New Delhi, India. For all purposes, double-distilled water was used.

2-Propanol, sodium hydroxide and potassium hydroxide were procured from Merck. Acetophenone, 4-hydroxy acetophenone, 4-chloro acetophenone, 4-nitro acetophenone, 4-bromo acetophenone, benzophenone, 4-bromo benzophenone, 2-pentanone, 3-pentanone and cyclohexanone were obtained from Tokyo Chemical Industry. All the reagents were of analytical reagent grade and used as received without further purification.

2.2 | Preparation of GO

GO was synthesized from graphite by adopting a simplified Hummers method as reported elsewhere.^[36] Here graphite powder (3 g) was treated with H₂SO₄ (120 ml) and NaNO₃ (2.5 g) followed by addition of KMnO₄ (15 g) with vigorous stirring maintaining the temperature at less than 20°C. To ensure complete oxidation of the graphite, the solution was stirred at room temperature for more than 24 hours. Then water (150 ml) was added slowly with vigorous agitation at 98°C for one day, and finally H₂O₂ (50 ml) solution was added to stop the oxidation process, during which the color of the solution become bright yellow, indicating the highly oxidized level of the graphite. The resulting GO was washed by rinsing and centrifugation with an aqueous solution containing 1 M HCl followed by deionized water several times. After filtration and drying under vacuum, the GO was obtained as grey powder.

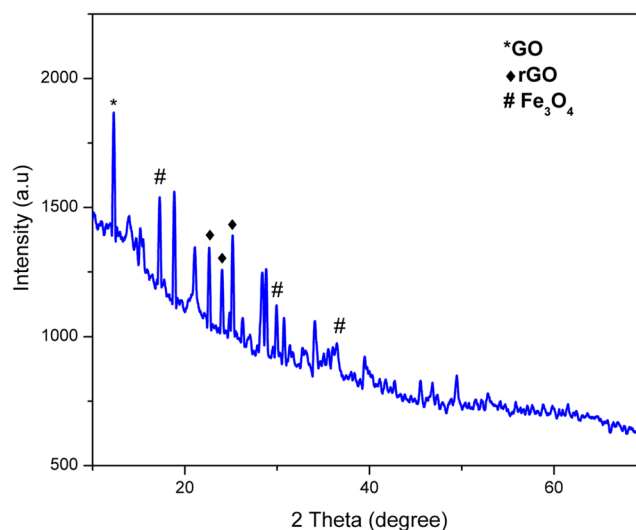


FIGURE 1 XRD pattern of rGO/Fe₃O₄ composite

2.3 | Preparation of rGO/iron oxide (rGO/Fe₃O₄) composite

The rGO/Fe₃O₄ composite was prepared using a simple *in situ* chemical synthesis method. A mixture of GO (200 mg) and deionized double-distilled water (50 ml) in a round-bottom flask was subjected to

ultrasonication about 30 minutes. To this dispersed solution, FeSO₄·7H₂O (50 mg) was added and the mixture was stirred for 24 hours at room temperature. To this mixture, 2 ml of 25% ammonium hydroxide was added dropwise to maintain the pH at 8. Upon addition of ammonium hydroxide, the color of the mixture turned reddish and finally became a deep red color

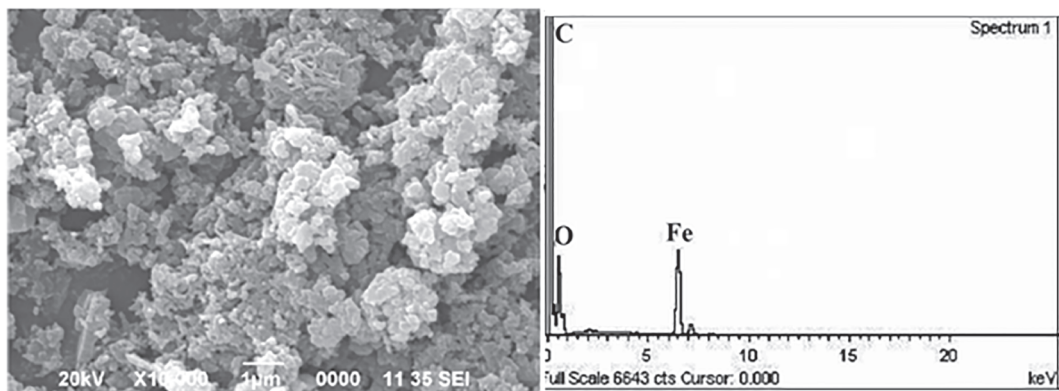


FIGURE 2 SEM image and energy-dispersive X-ray spectrum of rGO/Fe₃O₄

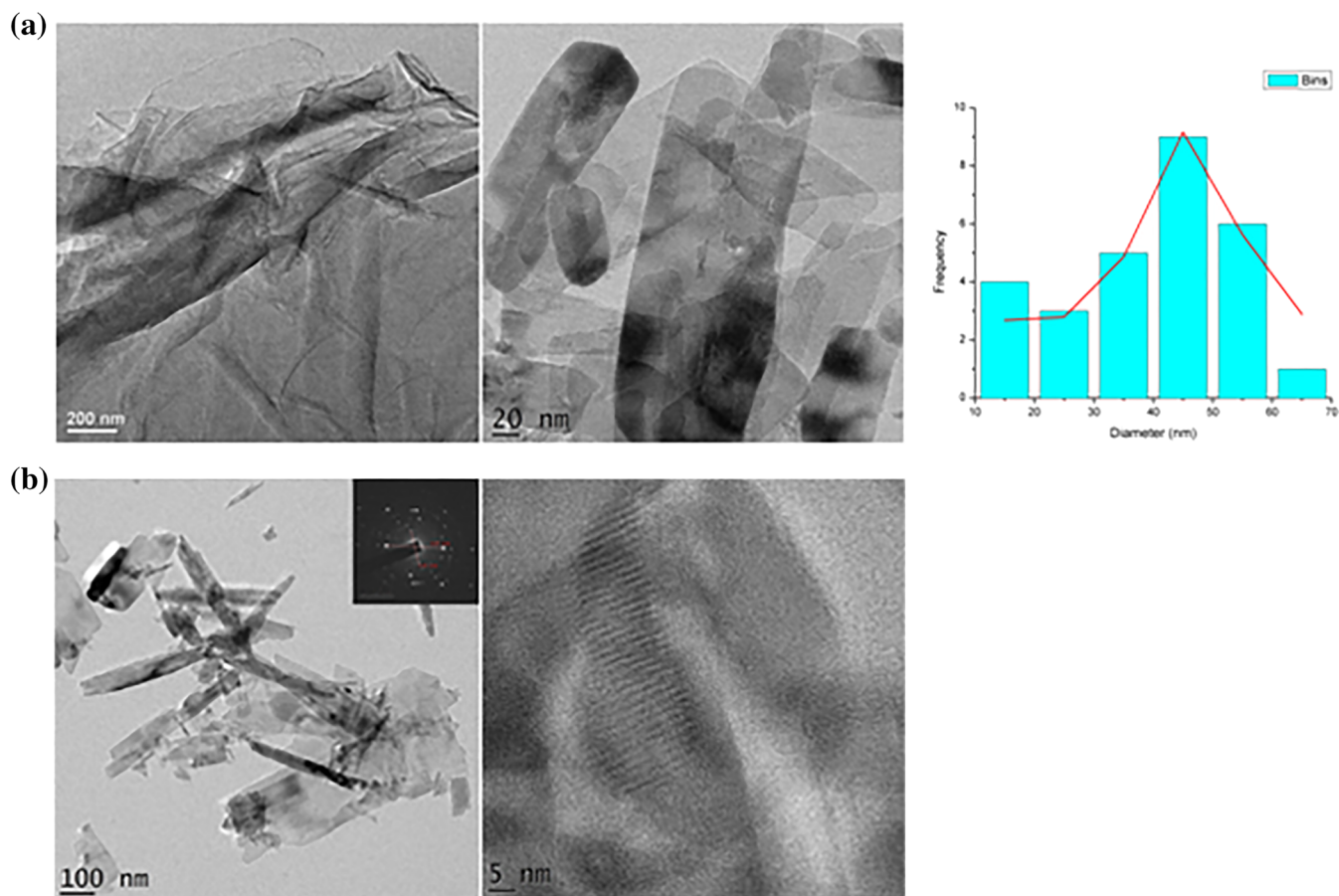


FIGURE 3 (a) TEM images of GO and rGO/Fe₃O₄ composite. (b) High-resolution TEM images of rGO/Fe₃O₄ composite with selected area electron diffraction pattern (inset)

because of the formation of ferric hydroxide. Then 0.7 ml of hydrazine hydrate was added dropwise and the mixture was kept for 24 hours at *ca* 90°C. The resulting mixture was finally washed with ethanol and water and then dried in a vacuum oven at 60°C.

2.4 | General characterization

Fourier transform infrared (FT-IR) spectroscopy was conducted with an Impact 410 (Nicolet, USA), using KBr pellets (400–4000 cm^{-1}). Scanning electron microscopy (SEM) images were recorded using a JSM-6390LV (JEOL, Japan) at 20 kV. TEM images were recorded at STIC Cochin and SAIC, Tezpur University using a Jeol/JEM 2100 and Tecnai G2 20 S-Twin (200 kV), at a resolution of 2.4 Å, respectively. A powder X-ray diffraction (XRD) study was carried out at room temperature (*ca* 25°C) using a Rigaku X-ray diffractometer with Cu $K\alpha$ radiation ($\lambda = 0.15418$ nm) at 30 kV and 15 mA using a scanning rate of $0.050^\circ \text{ s}^{-1}$ in the range $2\theta = 10\text{--}70^\circ$. X-ray photoelectron spectroscopy (XPS) was performed at ACMS, IIT Kanpur with an XPS-AES Module, model PHI 5000 Versa Prob II (FEI Inc.). Gas chromatography–mass spectrometry (GC–MS) analysis of the products was conducted using an Agilent Technologies GC system (7820) coupled with a mass detector (5975) and SHRXI-5MS column. ^1H NMR spectra of the products were recorded in CDCl_3 using a JEOL ECS-400. The magnetic hysteresis behavior of as-synthesized $\text{rGO}/\text{Fe}_3\text{O}_4$ composite material was investigated at room temperature against variable field using a Lakeshore 7410 series magnetometer.

2.5 | General procedure for transfer hydrogenation of ketones using $\text{rGO}/\text{Fe}_3\text{O}_4$ composite material as catalyst

The transfer hydrogenation reaction was carried out taking ketone (1 mmol), $\text{rGO}/\text{Fe}_3\text{O}_4$ composite catalyst (10 mg, 6.1 mol% of Fe), *i*-PrOH (5 ml) and Na-*i*-OPr (5 ml) in a round-bottomed flask and refluxing at 80°C for the required amount of time. The progress of the reaction was monitored continuously using TLC with 5% ethyl acetate–hexane. At the completion of the reaction (monitored using GC–MS), stirring was stopped and the catalyst was separated from the reaction mixture using a magnet. The remaining reaction mixture was diluted with water (10 ml) and then extracted with ethyl acetate (10 ml). The combined

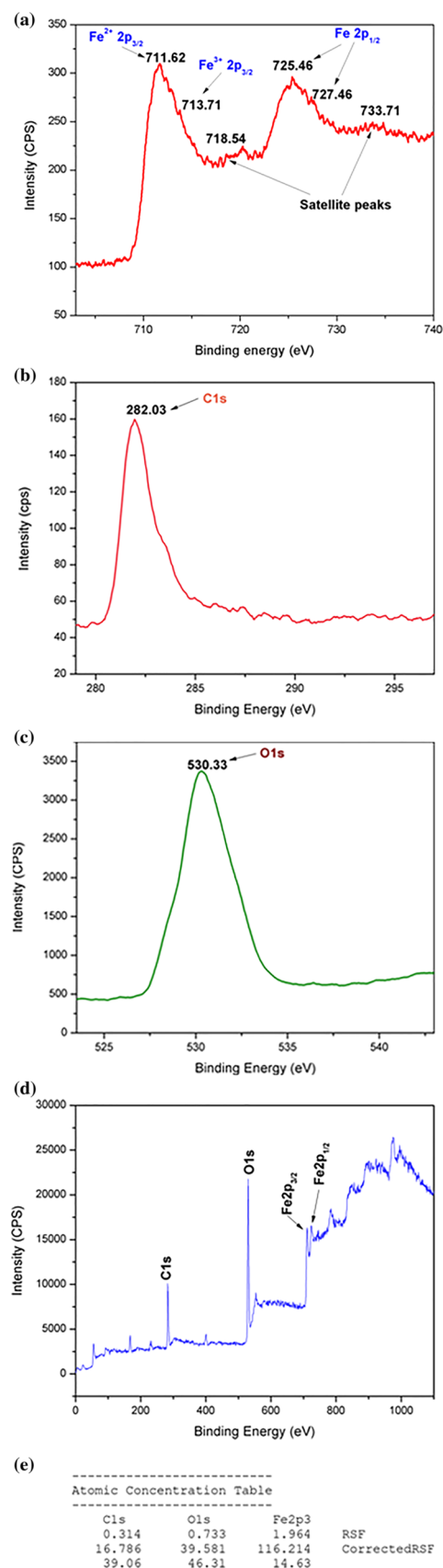


FIGURE 4 XPS spectra of $\text{rGO}/\text{Fe}_3\text{O}_4$ composite for (a) Fe 2p_{3/2}, (b) C 1s, (c) O 1s and (d) Fe 2p_{3/2}, C 1s and O 1s together. (e) Quantitative analysis

extract was washed with brine and dehydrated over anhydrous Na_2SO_4 . It was then purified by column chromatography (silica gel chromatography using ethyl acetate–hexane, 5:95) to afford the desired pure products. For recycling of the catalyst, after completion of the reaction the catalyst was isolated from the reaction mixture using a magnet and washed several times with water and ethyl acetate after each cycle. It was then dried at 110°C in an oven overnight. The recovered catalyst was subjected to subsequent runs under the same reaction conditions.

3 | RESULTS AND DISCUSSION

3.1 | Preparation of composite

The brownish-grey GO is mainly composed of carbon and oxygen with a C:O ratio of between 2.1 and 2.9 and it consists of loosely bound carbon layers. The surface of the GO sheet is bonded with various oxygen-containing functional groups, i.e. carboxyl, hydroxyl, etc., due to which it forms a stable aqueous suspension upon ultrasonication and stirring. Moreover, the oxygen-containing functional groups can be used to cross-link carbon with iron compounds to form the $\text{rGO}/\text{Fe}_3\text{O}_4$ composite.^[37]

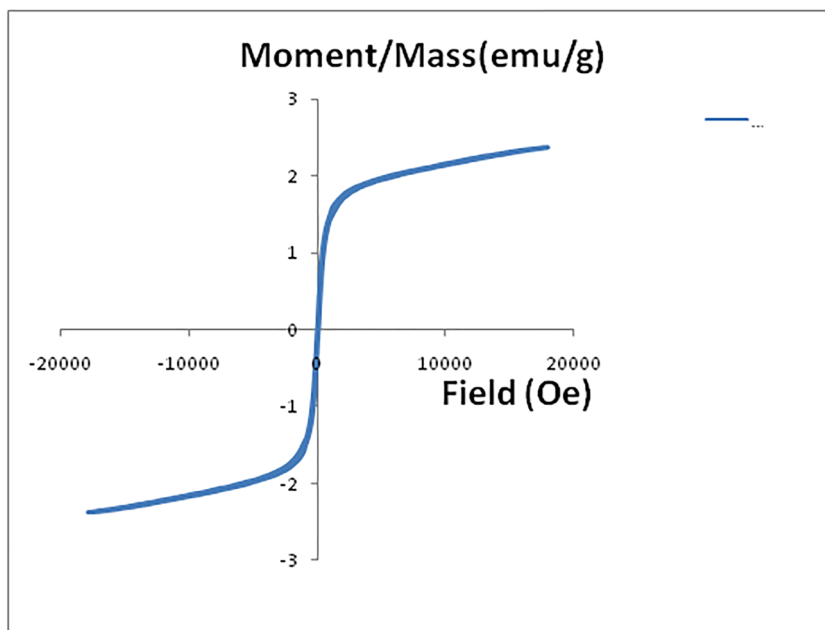
3.2 | Characterization of composite

3.2.1 | FT-IR study

In the FT-IR spectrum of GO (Figure S1a), the peaks at 3434 cm^{-1} (broad) and 1730 cm^{-1} correspond to the O–H and C=O stretching vibrations, respectively. The peaks at 1222 and 1485 cm^{-1} could be assigned to the C–O–C and C–OH stretching vibrations, respectively.^[38] The band at 1077 cm^{-1} corresponds to the C–O stretching vibration, indicating the presence of epoxide group in the GO layers. In the FT-IR spectrum of the $\text{rGO}/\text{Fe}_3\text{O}_4$ composite (Figure S1b), the peaks at 3159 , 3093 , 1520 and 1100 cm^{-1} could be attributed to the O–H, C–H, C–OH and C–O stretching vibrations, respectively. The broad peak at about 707 cm^{-1} could be due to stretching of Fe–O bond in bulk Fe_3O_4 indicating that Fe_3O_4 is bound to –COO on the GO surface, while that at 561 cm^{-1} might be assigned to the Fe–O bending vibration resulting from the formation of the $\text{rGO}/\text{Fe}_3\text{O}_4$ composite.^[39,40]

3.2.2 | XRD analysis

Figure 1 depicts a representative XRD pattern of the $\text{rGO}/\text{Fe}_3\text{O}_4$ composite, which coincides with the results from the TEM images (Figure 3) and supporting the formation of crystalline $\text{rGO}/\text{iron oxide}$ (i.e. Fe_3O_4)



Coercivity (Hci)	53.476 Oe
Magnetization (Ms)	2.3780 emu/g
Retentivity (Mr)	0.12777 emu/g

FIGURE 5 Magnetic hysteresis loop of $\text{rGO}/\text{Fe}_3\text{O}_4$

composite. The XRD pattern of the composite displays a series of diffraction peaks at $2\theta = 17.21^\circ$, 30.85° and 36.55° due to (111), (220) and (311) crystal planes of cubic spinel structure of magnetite Fe_3O_4 .^[41] The sharp peak at 2θ of 12.28° is the characteristic peak of GO, while the peaks at 2θ of 22.65° , 24.05° and 25.16° could be assigned to rGO.^[42–44]

3.2.3 | SEM analysis

In the SEM micrographs of the rGO/ Fe_3O_4 composite (Figure 2), smooth surfaces are observed. Since the iron particles are grown in the pores and galleries of GO sheets, the identification of individual phases is difficult from the SEM micrograph. However, from the energy-dispersive X-ray spectrum of the composite, the presence of a high level of iron particles with oxygen molecules is

observed which indicates the homogeneous distribution of iron oxide onto GO sheets. This structure enables a good connection and intimate contact between the components.

3.2.4 | TEM analysis

The morphologies of GO and rGO/ Fe_3O_4 composite are shown in TEM images (Figure 3a) along with particle size distribution. The as-prepared rGO/ Fe_3O_4 has a typically curved, layer-like structure with average sheet thickness of 40–50 nm. For the rGO/ Fe_3O_4 composite, the high-resolution TEM images (Figure 3b) show that all the GO sheets are homogeneously coated with iron oxide particles that are mainly grown on the surface or intercalate between the rGO sheets. SEM and TEM images reveal the uniform adsorption of iron oxide particles onto the

TABLE 1 Optimization of reaction conditions for transfer hydrogenation of benzophenone using rGO/ Fe_3O_4 composite catalyst^a

Entry	Catalyst (mol% of Fe)	Hydrogen donor	Base	Time (h)	Isolated yield (%)
1	—	<i>i</i> -PrOH	KOH	24	—
2	3.05 in 5 mg	<i>i</i> -PrOH	—	24	—
3	3.05 in 5 mg	<i>i</i> -PrOH	K- <i>i</i> -OPr	24	—
4	6.1 in 10 mg	<i>i</i> -PrOH	K- <i>i</i> -OPr	24	—
5	9.15 in 15 mg	<i>i</i> -PrOH	K- <i>i</i> -OPr	24	—
6	12.2 in 20 mg	<i>i</i> -PrOH	K- <i>i</i> -OPr	24	—
7	12.2 in 20 mg	<i>i</i> -PrOH	KOH	24	— ^b
8	3.05 in 5 mg	<i>i</i> -PrOH	K- <i>i</i> -OPr	5	63 ^b
9	6.1 in 10 mg	HCOOH	K- <i>i</i> -OPr	6	— ^c
10	12.2 in 20 mg	HCOOH	Et ₃ N	6	— ^c
11	12.2 in 20 mg	HCOOH	Et ₃ N	6	— ^d
12	3.05 in 5 mg	<i>i</i> -PrOH	K- <i>i</i> -OPr	3	86 ^d
13	6.1 in 10 mg	<i>i</i> -PrOH	K- <i>i</i> -OPr	3	86 ^d
14	12.2 in 20 mg	<i>i</i> -PrOH	K- <i>i</i> -OPr	3	86 ^d
15	6.1 in 10 mg	<i>i</i>-PrOH	Na-<i>i</i>-OPr	3	99^d
16	9.15 in 15 mg	<i>i</i> -PrOH	Na- <i>i</i> -OPr	3	99 ^d
17	12.2 in 20 mg	<i>i</i> -PrOH	Na- <i>i</i> -OPr	3	99 ^d

^aReaction conditions: benzophenone (1 mmol), hydrogen donor (5 ml), base (2 mmol or 5 ml Na-*i*-OPr/K-*i*-OPr prepared by refluxing 2 mmol of base in 20 ml of *i*-PrOH), catalyst (rGO/ Fe_3O_4), room temperature (25°C) in air unless otherwise noted.

^bAt 60°C.

^cAt 70°C.

^dAt 80°C.

chemically modified rGO surface and/or filled between the rGO nanosheets.

3.2.5 | XPS analysis

In the XPS spectrum of the composite (Figure 4a), two peaks at binding energies of 711.62 and 713.71 eV correspond to $\text{Fe}^{2+} 2p_{3/2}$ and $\text{Fe}^{3+} 2p_{3/2}$, respectively, which are indicative of structural configuration of Fe_3O_4 . Two satellite peaks at 718.54 and 733.71 eV confirm that the Fe in the composite is in the divalent state. In addition, peaks at 725.46 and 727.46 eV corresponding to Fe $2p_{1/2}$ of Fe are also observed. The XPS spectra for C 1s (Figure 4b) and O 1s (Figure 4c) are also shown. For O 1s, a peak at binding energy of 530.33 eV is observed which is the typical state of Fe–O corresponding to Fe_3O_4 .^[45,46]

3.2.6 | Vibrating sample magnetometry

The room temperature magnetic hysteresis behavior (magnetization and field) of $\text{rGO}/\text{Fe}_3\text{O}_4$ shown in Figure 5 was studied using a vibrating sample magnetometer. It exhibited a characteristic pattern of a ferromagnetic component. As the driving magnetic field was decreased to zero, the composite had still a remanence value of 0.128 emu g^{-1} with coercivity value of 53.476 Oe . The saturation magnetization was found to be $2.3780 \text{ emu g}^{-1}$. This behavior of the synthesized material unambiguously supports the presence of a ferromagnetic component.

3.3 | Transfer hydrogenation of ketones catalyzed by $\text{rGO}/\text{Fe}_3\text{O}_4$ composite material

To optimize the reaction conditions such as temperature, reaction time, catalyst loading, base, etc., for excellent catalytic performance, a number of runs were carried out using benzophenone as the starting substrate (Table 1). Initially, benzophenone (1 mmol), *i*-PrOH (5 ml) and KOH (2 mmol) were taken in the absence of the catalyst and stirred for 24 hours at room temperature, which resulted in no product formation (Table 1, entry 1). In the next move, 5 mg of $\text{rGO}/\text{Fe}_3\text{O}_4$ composite catalyst (3.05 mol% of Fe) was introduced in the absence of any base followed by stirring for 24 hours (Table 1, entry 2), which also showed no product formation. This clearly shows the importance of both catalyst and base for the reaction to proceed. It has been observed that using *K-i*-OPr (base) and *i*-PrOH (hydrogen donor) at 60°C results in 63% product formation (Table 1, entry 8), while raising temperature to 80°C afforded 86% product formation, which does not increase further even on increasing the amount of the catalyst (Table 1, entries 12–14). But use of *Na-i*-OPr (base) in *i*-PrOH (hydrogen donor) at 80°C gives the best result within 3 hours (99%) (Table 1, entry 15). Hence, after careful investigation of a wide range of catalytic reaction parameters, 10 mg of the $\text{rGO}/\text{Fe}_3\text{O}_4$ composite catalyst (6.1 mol% of Fe), *Na-i*-OPr in *i*-PrOH at 80°C seemed the most suitable for further catalytic reactions.

Since the role of base is very important in transfer hydrogenation of benzophenone, we investigated the

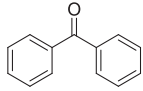
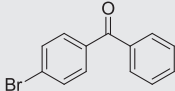
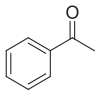
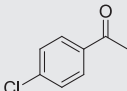
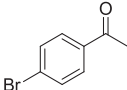
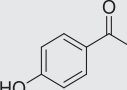
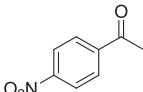
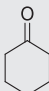
TABLE 2 Optimization of base for transfer hydrogenation of benzophenone^a

Entry	Base	Isolated yield (%)
1	KOH	—
2	<i>K-i</i> -OPr	86 ^b
3	NaOH	—
4	<i>Na-i</i> -OPr	93
5	<i>Na-i</i>-OPr	99^b
6	Na_2CO_3	—
7	Et_3N	—
8	NaHCO_3	—
9	K_2CO_3	—

^aReaction conditions: benzophenone (1 mmol), hydrogen donor (*i*-PrOH, 5 ml), base (1 mmol), catalyst ($\text{rGO}/\text{Fe}_3\text{O}_4$ composite, 6.1 mol% of Fe, 10 mg), 80°C .

^b2 mmol of base.

TABLE 3 Transfer hydrogenation of various substrates using rGO/Fe₃O₄ composite catalyst^a

Entry	Substrate	Time (h)	Isolated yield (%)	Conversion (GC-MS) (%)	TON	TOF ($\times 10^{-3} \text{ h}^{-1}$)
1		3	99	100	16.23	5410
2		2	99	100	16.23	8115
3		2.5	99	100	16.23	6492
4		2	97	100	15.9	7951
5		2	98	99	16.06	8033
6		3	—	—	—	—
7		3	—	—	—	—
8		3	99	100	16.23	5410

(Continues)

TABLE 3 (Continued)

Entry	Substrate	Time (h)	Isolated yield (%)	Conversion (GC-MS) (%)	TON	TOF ($\times 10^{-3} \text{ h}^{-1}$)
9		3	—	—	—	—
10		3	—	—	—	—

^aReaction conditions: ketone (1 mmol), *i*-PrOH (5 ml), Na-*i*-OPr (5 ml), rGO/Fe₃O₄ composite (10 mg, 6.1 mol% of Fe) at 80°C in air. Formation of products was confirmed using FT-IR, ¹H NMR and GC-MS analyses and then compared authentically. TON, turnover number; TOF, turnover frequency.

reaction using bases such as KOH, K-*i*-OPr, NaOH, Na-*i*-OPr, Na₂CO₃, Et₃N, NaHCO₃ and K₂CO₃ (Table 2) and observed that 2 mmol of Na-*i*-OPr gives best result at 80 C in 3 hours (Table 2, entry 5).

With the optimized reaction conditions (i.e. 10 mg of rGO/Fe₃O₄ composite as catalyst, 5 ml of *i*-PrOH as hydrogen donor and 5 ml of Na-*i*-OPr as the base at 80 C for 3 hours) in hand, we studied the scope and efficiency of this methodology and hence employed various substrates to investigate the scope of the catalyst (Table 3). It was observed that hydrogenation of benzophenone (Table 3, entry 1) is slower than that of acetophenone (Table 3, entry 3) which may be attributed to increased ring strain due to two bulky phenyl rings in the benzophenone substrate.^[47] 4-Bromo benzophenone (Table 3, entry 2) gives a better result than benzophenone which may be due to the electron-withdrawing effect of Br at *p*-position. A similar effect is also observed in the case of 4-chloro acetophenone and 4-bromo acetophenone (Table 3, entries 4 and 5) which reduces the electron density on the carbonyl group increasing the affinity of the substrates towards easier hydrogenation. On the other hand, 4-hydroxy acetophenone (Table 3, entry 6) with its electron-donating OH group decelerates the reaction resulting in no product formation.^[24] 4-Nitro acetophenone (Table 3, entry 7)^[48] and aliphatic substrates (Table 3, entries 9–15) except cyclohexanone (Table 3, entry 8)^[13] were difficult to reduce using our catalyst.

It is pertinent to mention that a comparative study was carried out of various Fe-based catalysts for transfer hydrogenation of carbonyl compounds (Table 4), and it was observed that in most cases high temperature or

inert atmosphere were used and afforded highest isolated yield of 99% with 3–6 reuse cycles. However, our rGO/Fe₃O₄ composite catalyst gave 97–99% isolated yield at 80°C. Moreover, our catalyst could be easily separated from the reaction mixture using a magnet and reused for at least five times without compromising its activity. To the best of our knowledge, our rGO/Fe₃O₄ composite material system represents one of the best magnetically recyclable catalytic systems reported so far for transfer hydrogenation of ketones. Hence, the results in Table 4 show the superior efficacy of our catalyst over other previously reported Fe-based catalysts.

3.3.1 | Probable mechanism

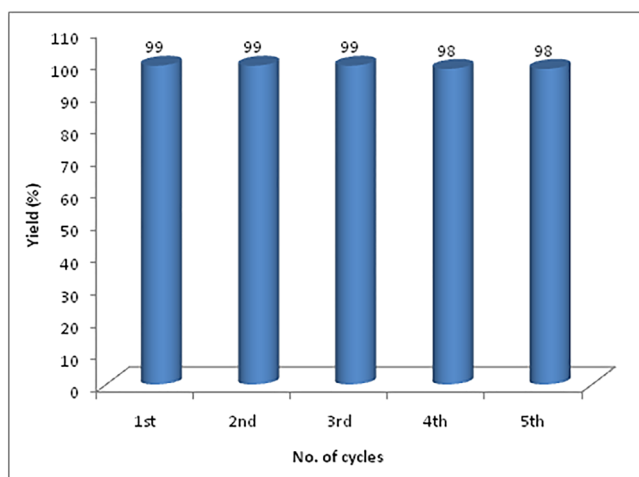
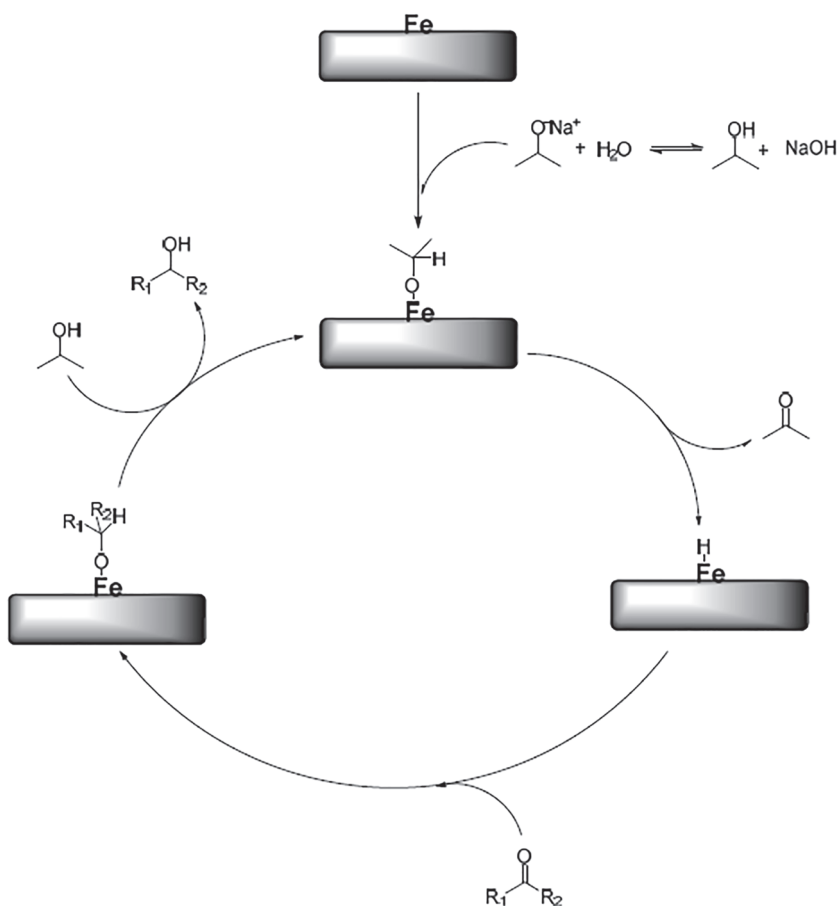
A plausible mechanism for hydrogenation of ketones^[56,57] using the rGO/Fe₃O₄ catalyst is demonstrated in Scheme 1.

3.3.2 | Catalyst recycling

The most important advantage of immobilized complexes is their recyclability. In order to study its sustainability, recyclability of the catalyst was investigated using benzophenone as the model substrate. At reaction completion, the catalyst was easily separated from the reaction mixture using a magnet, washed several times with distilled water, dried and reused in a subsequent reaction. To our delight, the catalyst could be recycled at least five times without compromising its catalytic efficiency or product yield (Figure 6).

TABLE 4 Comparative study

Entry	Catalyst	Reactants	Temperature (°C); reaction conditions	Reaction time (reusability)	Solvent	Isolated yield (%)	Ref.
1	rGO/Fe ₃ O ₄ composite	Aromatic ketones with derivatives, cyclohexanone	80; Magnetic stirring	2–3 h (Magnetically separable; 5 cycles)	i-PrOH	97–99	This
2	Fe@imine-mont-K10	Both aromatic and aliphatic ketones	80; Magnetic stirring	30 min–5 h (5 cycles)	i-PrOH/CH ₃ CN (1:1)	51–99	[31]
3	2-[1-(3,5-Dimethylpyrazol-1-yl)ethyl]pyridine Fe(II)Cl ₂	Acetophenone	82; Magnetic stirring	48 h	i-PrOH	67	[47]
4	FePc/Al ₂ O ₃	Benzaldehyde, acetophenone and derivatives	80; Magnetic stirring	6–12 h (3 cycles)	i-PrOH	33–99	[49]
5	N-heterocyclic carbene iron(II) complexes	aromatic, cyclic and aliphatic ketones	82; Magnetic stirring, inert atmosphere	12 h	i-PrOH	3–87	[50]
6	Iron phthalocyanine, Fe(Pc)	<i>trans</i> -Cinnamaldehyde, benzaldehyde and derivatives	80; Magnetic stirring, Ar atmosphere	6 or 12 h (3 cycles)	i-PrOH	25–99	[51]
7	γ -Fe ₂ O ₃ @HAP	Furfural, hydroxyl methylfurfural, ethyl levulinate, acetophenone, benzaldehyde	180; Magnetic stirring	10 h (6 cycles)	i-PrOH	80–95.3	[52]
8	(Pyrazole)pyridine iron(II)	Benzophenone, acetophenone and derivative, 2-methylcyclohexanone, 3-pentanone, 2-acetylpyridine	82; Magnetic stirring	48 h	i-PrOH	56–99	[53]
9	Nitrogen-doped carbon-supported iron catalyst	Furfural	180; Magnetic stirring	6 h (5 cycles)	i-PrOH	91.6	[54]
10	ImmFe-IL	Nitroarenes	110; Magnetic stirring	12 h (4 cycles)	Hydrazine hydrate and ethylene glycol	20–99	[55]

SCHEME 1 Plausible mechanism for transfer hydrogenation of ketones**FIGURE 6** Recycling of the catalyst

4 | CONCLUSIONS

The present study reports the formulation of a new Fe-based hybrid composite material obtained by immobilization on synthesized GO. The composite material was found to be crystalline and showed excellent catalytic activity for transfer hydrogenation of ketones in *i*-PrOH. The advantages of the catalyst are that it is magnetically

separable and could be recycled at least five times without significant loss in activity.

ACKNOWLEDGEMENTS

The authors thank STIC, Cochin for high-resolution TEM, IIT Kanpur for XPS, CIF, IIT Guwahati for vibrating sample magnetometry, and SAIC, Tezpur University for TEM and ^1H NMR analytical facilities and UGC-SAP-DRS-I program (2016-2021). S.B. thanks DST-SERB, India for financial support of the research work under DST Women Scientist Scheme A (no. SR/WOS-A/CS-161/2016). S.S. is grateful to UGC-Maulana Azad National Fellowship, Delhi for financial support.

DECLARATION OF INTEREST STATEMENT

The authors declare that there is no conflict of interest regarding the publication of this article.

ORCID

Geetika Borah  <https://orcid.org/0000-0002-5781-1694>

REFERENCES

- [1] H. Wang, H. S. Casalongue, Y. Liang, H. Dai, *J. Am. Chem. Soc.* **2010**, *132*, 7472.

- [2] D. R. Dreyer, S. Park, C. W. Bielawski, R. S. Ruoff, *Chem. Soc. Rev.* **2010**, 39, 228.
- [3] Y. Zhang, G. Li, H. Lu, Q. Lv, Z. Sun, *RSC Adv.* **2014**, 4, 7594.
- [4] R. Kumar, K. Jayaramulu, T. K. Maji, C. N. R. Rao, *Chem. Commun.* **2013**, 49, 4947.
- [5] C. Petit, T. J. Bandosz, *Adv. Mater.* **2009**, 21, 4753.
- [6] N. A. Zubir, C. Yacou, J. Motuzas, X. Zhang, X. S. Zhao, J. C. D. da Costa, *Chem. Commun.* **2015**, 51, 9291.
- [7] M. Jahan, Q. Bao, J. X. Yang, K. P. Loh, *J. Am. Chem. Soc.* **2010**, 132, 14487.
- [8] N. A. Zubir, C. Yacou, J. Motuzas, X. W. Zhang, J. C. D. da Costa, *Sci. Rep.* **2014**, 4, 4594.
- [9] T. P. See, A. Pandikumar, L. H. Ngee, H. N. Ming, C. C. Hua, *Catal. Sci. Technol.* **2014**, 4, 4396.
- [10] S. Paulose, R. Raghavan, B. K. George, *RSC Adv.* **2016**, 6, 45977.
- [11] A. M. Pálvölgyi, J. Bitai, V. Zeindlhofer, C. Schröder, K. Bica, *ACS Sustainable Chem. Eng.* **2019**, 7, 3414.
- [12] S. Biswas, D. Sarkar, P. Roy, T. K. Mondal, *Polyhedron* **2017**, 131, 1.
- [13] L. Wang, T. Liu, *Chin. J. Catal.* **2018**, 39, 327.
- [14] S. Biswas, P. Roy, S. Jana, T. K. Mondal, *J. Organometal. Chem.* **2017**, 846, 201.
- [15] B. Stefane, F. Pozgan, *Catal. Rev. Sci. Eng.* **2014**, 56, 82.
- [16] M. Aydemir, N. Meric, C. Kayan, F. Ok, A. Baysal, *Inorg. Chim. Acta* **2013**, 398, 1.
- [17] G. Tang, M. Chen, J. Fang, Z. Xu, H. Gong, Q. Peng, Z. Hou, *Catal. Commun.* **2019**, 121, 43.
- [18] A. Lazar, S. Silpa, C. P. Vinod, A. P. Singh, *Mol. Catal.* **2017**, 440, 66.
- [19] T. M. Townsend, C. Kirby, A. Ruff, A. R. O'Connor, *J. Organometal. Chem.* **2017**, 843, 7.
- [20] A. Matsunami, Y. Kayaki, *Tetrahedron Lett.* **2018**, 59, 504.
- [21] T. Song, Y. Duan, Y. Yang, *Catal. Commun.* **2019**, 120, 80.
- [22] P. Roy, C. K. Manna, R. Naskar, T. K. Mondal, *Polyhedron* **2019**, 158, 208.
- [23] J. Li, J. Han, Z. Lin, L. Tang, Q. Huang, Q. Wang, J. Zhu, J. Deng, *Tetrahedron* **2019**, 75, 422.
- [24] M. K. Yılmaz, M. Keleş, *Transit. Met. Chem.* **2018**, 43, 285.
- [25] N. Zacharopoulos, E. Kolovou, A. Peppas, K. Koukoulakis, E. Bakeas, G. Schnakenburg, A. I. Philippopoulos, *Polyhedron* **2018**, 154, 27.
- [26] R. Hodgkinson, V. Jurčík, H. Nedden, A. Blackaby, M. Wills, *Tetrahedron Lett.* **2018**, 59, 930.
- [27] D. J. Braden, R. Cariou, J. W. Shabaker, R. A. Taylor, *Appl. Catal. A* **2019**, 570, 367.
- [28] F. Durap, M. Aydemir, A. Baysal, D. Elma, B. Ak, Y. Turgut, *Inorg. Chim. Acta* **2014**, 411, 77.
- [29] J. Volbeda, P. G. Jones, M. Tamm, *Inorg. Chim. Acta* **2014**, 422, 158.
- [30] J. Chen, T. Zhang, X. Liu, L. Shen, *Catal. Lett.* **2019**, 149, 601.
- [31] B. Qiu, W. Wang, X. Yang, *Catalysts* **2019**, 9, 101.
- [32] S. Sultana, G. Borah, P. K. Gogoi, *Catal. Lett.* **2019**, 149, 2142.
- [33] K. Z. Demmans, M. E. Olson, R. H. Morris, *Organometallics* **2018**, 37, 4608.
- [34] W. Wu, T. Seki, K. L. Walker, R. M. Waymouth, *Organometallics* **2018**, 37, 1428.
- [35] S. Sultana, G. Borah, P. K. Gogoi, *Appl. Organometal. Chem.* **2019**, 33, e4595.
- [36] S. Konwer, A. Begum, S. Bordoloi, R. Boruah, *J. Polym. Res.* **2017**, 24, 37.
- [37] K. Zhang, V. Dwivedi, C. Chi, J. Wu, *J. Hazard. Mater.* **2010**, 182, 162.
- [38] M. S. Sher Shah, A. R. Park, K. Zhang, J. H. Park, P. J. Yoo, *ACS Appl. Mater. Interfaces* **2012**, 4, 3893.
- [39] X. Yang, X. Zhang, Y. Ma, Y. Huang, Y. Wang, Y. Chen, *J. Mater. Chem.* **2009**, 19, 2710.
- [40] F. Ahangaran, A. Hassanzadeh, S. Nouri, *Int. Nano Lett.* **2013**, 3, 23.
- [41] W. Cheng, K. Tang, Y. Qi, J. Sheng, Z. Liu, *J. Mater. Chem.* **2010**, 20, 1799.
- [42] I. Saikia, M. Hazarika, C. Tamuly, *Mater. Res. Express* **2016**, 3, 105007.
- [43] S. Konwer, A. K. Guha, S. K. Dolui, *J. Mater. Sci.* **2013**, 48, 1729.
- [44] C. Ma, K. Yang, L. Wang, X. Wang, *J. Appl. Biomater. Funct. Mater.* **2017**, 15, 1.
- [45] P. M. Hallam, M. G. Mingot, D. K. Kampouris, C. E. Banks, *RSC Adv.* **2012**, 2, 6672.
- [46] X. Wang, Y. Liu, H. Arandiyan, H. Yang, L. Bai, J. Mujtaba, Q. Wang, S. Liu, H. Sun, *Appl. Surf. Sci.* **2016**, 389, 240.
- [47] M. N. Magubane, M. G. Alam, S. O. Ojwach, O. Q. Munro, *J. Mol. Struct.* **2017**, 1135, 197.
- [48] N. U. D. Reshi, D. Senthurpandi, A. G. Samuelson, *J. Organometal. Chem.* **2018**, 866, 189.
- [49] P. Bata, F. Notheisz, P. Kluson, A. Zsigmond, *Appl. Organometal. Chem.* **2015**, 29, 45.
- [50] M. D. Bala, M. I. Ikhile, *J. Mol. Catal. A* **2014**, 385, 98.
- [51] P. Bata, A. Zsigmond, M. Gyemant, A. Czegledi, P. Kluson, *Res. Chem. Intermed.* **2015**, 41, 9281.
- [52] F. Wang, Z. Zhang, *ACS Sustainable Chem. Eng.* **2017**, 5, 942.
- [53] M. N. Magubane, G. S. Nyamoto, S. O. Ojwach, O. Q. Munro, *RSC Adv.* **2016**, 6, 65205.
- [54] J. Li, J. Liu, H. Zhou, Y. Fu, *Chem. Sus. Chem.* **2016**, 9, 1339.
- [55] N. M. Patil, T. Sasaki, B. M. Bhanage, *ACS Sustainable Chem. Eng.* **2016**, 4, 429.
- [56] R. Hudson, V. Chazelle, M. Bateman, R. Roy, C. J. Li, A. Moores, *ACS Sustainable Chem. Eng.* **2015**, 3, 814.
- [57] B. S. Kumar, A. J. Amali, K. Pitchumani, *Mol. Catal.* **2018**, 448, 153.

SUPPORTING INFORMATION

Additional supporting information may be found online in the Supporting Information section at the end of this article.

How to cite this article: Sultana S, Bordoloi S, Konwer S, Borah G, Gogoi PK. Reduced graphene oxide/iron oxide hybrid composite material as an efficient magnetically separable heterogeneous catalyst for transfer hydrogenation of ketones. *Appl Organometal Chem.* 2020;34:e5582. <https://doi.org/10.1002/aoc.5582>

See discussions, stats, and author profiles for this publication at: <https://www.researchgate.net/publication/343649892>

Field experience of Fluoride Nilogon: a method of fluoride removal from groundwater

Article · January 2020

CITATIONS

0

READS

68

8 authors, including:



Raj kamal Mohan

Tezpur University

4 PUBLICATIONS 8 CITATIONS

[SEE PROFILE](#)



Sweety Gogoi

Tezpur University

8 PUBLICATIONS 170 CITATIONS

[SEE PROFILE](#)



Anup Jyoti Bora

Tezpur University

6 PUBLICATIONS 52 CITATIONS

[SEE PROFILE](#)



Shreemoyee Bordoloi

Tezpur University

11 PUBLICATIONS 181 CITATIONS

[SEE PROFILE](#)

Some of the authors of this publication are also working on these related projects:



Water treatment for removal of arsenic, fluoride and mercury from drinking water [View project](#)



(i) Arsenic, fluoride and mercury removal from drinking water; (ii) Chemistry of Mahi, the ink for Sancipat manuscript of early Assam. [View project](#)

Field experience of Fluoride Nilogon: a method of fluoride removal from groundwater

Rajkamal Mohan, Sweety Gogoi, Anup J. Bora, Gautam Baruah, Shremoyee Bordoloi, Asadulla A. Ali, Hridip R. Sarma and Robin K. Dutta*

Department of Chemical Sciences, Tezpur University, Napaam 784 028, India

Field trial of a patented fluoride removal method, based on precipitation–adsorption, has been carried out in some villages of Assam, North East India, with groundwater sources containing 1.8–20 mg/l initial [F⁻] at small community (220 l) and household (15 l) levels. Pre-acidified water containing 0.68 mM phosphoric acid was treated in a crushed limestone bed (1–20 mm) for 3 h and filtered through a sand–gravel filter to retain a desired 0.7 mg/l [F⁻] with pH of 7.44–7.9 and relevant water quality parameters meeting WHO guidelines. A slightly higher dose can totally remove fluoride. The fluoride removal has been found to be independent of initial [F⁻]. The units have been showing consistent results till now for over five and half years and 4625 batches of use without requiring any interventions like reactivation, replacement or replenishment of the limestone bed. With consistent removal of fluoride from any initial concentration to a desired concentration, a recurring cost of only Rs 0.005/l of water and an estimated life of the limestone bed of about 50 years or 39,000 batches, this safe, environment-friendly and simple method without requiring electricity, has been gaining popularity as Fluoride Nilogon.

Keywords: Fluoride removal, groundwater, hydroxyapatite, limestone defluoridation, phosphoric acid.

FLUORIDE, a naturally occurring mineral, is essential in small quantities for proper growth and maintenance of teeth and bones in humans. However, its excess consumption causes irreversible damage to teeth and bones, a phenomenon known as dental and skeletal fluorosis¹. Other effects such as osteoporosis, arthritis, brain damage, cancer and neurological disorders in human and certain health problems in animals are seen due to excess fluoride consumption^{1–3}. Fluoride contamination in groundwater occurs due to geological factors such as dissolution of rocks like fluorite, biotite, topaz, etc. and anthropogenic activities like industrial effluents⁴. Over 200 million people from India, China, Sri Lanka and the Rift Valley nations in Africa are affected by excess fluoride poison-

ing². In India, groundwater of many states are fluoride-affected⁵. In Assam, North East India, large areas of East Karbi Anglong and Hojai district and some parts in neighbouring areas of Guwahati city are affected by excess fluoride in groundwater^{6,7}. The World Health Organization (WHO) prescribes a guideline value of 1.5 mg/l for fluoride in drinking water². However, the Bureau of Indian Standards (BIS) has set a lower permissible limit of 1.0 mg/l for fluoride⁸.

Research is ongoing to develop a suitable method for removal of difficult-to-remove fluoride with high efficiency and low cost, while at the same time the method has to be safe, environment-friendly and easy to operate by a layman^{9–11}. Researchers have developed several defluoridation techniques to mitigate fluoride contamination, viz. coagulation–precipitation¹², reverse osmosis¹³, electro-coagulation¹⁴, nanofiltration¹⁵, ion exchange¹⁶, adsorption^{17,18}, etc. The Nalgonda technique, based on the coagulation–precipitation technique, was once widely used in India. Now it is losing popularity due to difficulty in pH adjustment, high residual sulphate and aluminium in treated water¹⁴.

Adsorption is one of the most common methods of fluoride removal due to its effectiveness, relatively low cost and easy operation. Several adsorbent materials have been reported for fluoride removal from water, e.g. limestone (calcite)^{19–21}, hydroxyapatite¹⁹, quartz¹⁹, bauxite²², gypsum²², brushite²³, laterite²⁴, pumice stone²⁵, rare earth oxides²⁶, graphene²⁷, chitosan²⁸, activated alumina²⁹, alum³⁰, and calcined phosphoric acid (PA)-treated lime³¹. Reardon and Wang³², reported a combined precipitation and adsorption method where CO₂ is passed through fluoride-contaminated water in a limestone bed column for generating Ca²⁺ ions for precipitation of CaF₂. However, handling of CO canisters is not easy for rural applications. Several interesting studies were conducted subsequently by adding other acids to the influent water, before treatment with crushed limestone, where fluoride was removed by both precipitation of fluorite and adsorption of fluoride on limestone surface^{21,33–37}. However, fluoride removal by these methods is associated with one or more shortcomings, such as high operational and maintenance costs, low capacity of adsorbent, frequent replacement of parts and involving energy-intensive steps³⁴.

*For correspondence. (e-mail: robind@tezu.ernet.in)

Recently, a highly efficient, low-cost, safe and environment-friendly method of fluoride removal, viz. phosphoric acid-crushed limestone treatment (PACLT), had been patented and reported by our research group^{38,39}. In this method, water is pre-mixed with 0.01 M PA and then treated in a crushed limestone fixed-bed reactor working in a plug-flow (batch) mode for 3 h. Precipitation of CaF₂, fluorapatite (FAP), and physisorption of fluoride by hydroxyapatite (HAP) formed *in situ* from the reaction between calcium and phosphate ions in the reactor were found to be the dominant mechanisms for fluoride removal in this method³⁸. Since a bench-scale pilot test of the method using synthetic fluoride-containing water had shown it to have high potential for practical applications³⁸, we had decided to conduct a field trial.

Here we present results of the field trial of the PACLT method at a small community scale and household level in some fluoride-affected villages of East Karbi Anglong district. The dose of PA was optimized using fluoride containing natural feed water collected from one of the field sources to remove excess fluoride and retaining about 0.6 mg/l fluoride in the treated water. The performance of the field units was pre-assessed with a small replica of the field unit set-up in the laboratory using feed water collected from the field source. The results of the field trial, its safety and suitability have been discussed.

The field trial has already completed over five and half years, but the units are still working well. The method has already started gaining popularity as Fluoride Nilogon (nilogon meaning removal in Assamese). Despite using for total of 4625 batches (once or twice a day) and even for water with initial fluoride ([F⁻]₀) as high as 20 mg/l, none of the limestone beds has been exhausted yet, making it impossible for us to carry out a study of regeneration of the limestone bed. The excellent experience of the field trial prompted us to publish the results without waiting for exhaustion of the limestone to facilitate use of this rural technology for the benefit of the needy at the earliest.

Materials and methods

Materials

Limestone used in the field trial was obtained as a gift from Bokajan Cement Factory, Cement Corporation of India, Bokajan, Karbi Anglong. The limestone sample with density 2.59 g/cm³ was high-purity calcite as evident from chemical composition and XRD analysis³⁶. The crude limestone was crushed and segregated to selected chip sizes before use. For dose-optimization experiments, the fluoride stock solution was prepared by dissolving NaF (AR-grade, Merck, Mumbai) in doubly distilled

water. Synthetic fluoride containing groundwater was prepared by spiking tap water with fluoride from the stock solution. The composition of the synthetic groundwater was: pH (7.47), Na⁺ (60.60 mg/l), K⁺ (1.07 mg/l), Ca²⁺ (2.50 mg/l), Mg²⁺ (2.40 mg/l), Hg²⁺ (<0.001 mg/l), F⁻ (0.20 mg/l), Cl⁻ (5.4 mg/l), SO₄²⁻ (6.3 mg/l), PO₄³⁻ (0.70 mg/l), hardness as CaCO (80 mg/l) and alkalinity as CaCO (86 mg/l). Analytical-grade PA (Merck, Mumbai) was used in laboratory experiments. Food-grade 85% PA (Lakshita Chemicals, Mumbai) was used in field trials.

Field units

One small community unit of 220 l capacity and five household units of 15 l capacity each were used for the field trial in four different villages of East Karbi Anglong district ([Supplementary Figures 1 and 2](#)). The fluoride concentration in water of the selected field sources was found to be in the range 20.0–2.8 mg/l. For the small community system, a 500 l plastic tank was used as the reactor chamber, whereas a 1000 l plastic tank was used as the four-layered sand-crushed limestone–sand–gravel filter-cum-pH corrector. The reactor chamber filled with crushed limestone of size 1–20 mm gave a void volume of 220 l. An additional 500 l plastic tank was used to collect the fluoride-contaminated water supplied by the local public health water supply scheme. For household systems, a 40 l bucket was used as the reactor chamber, containing limestone chips of the same size, giving a void volume of 15 l ([Supplementary Figure 2](#)). A four-layered filter-cum-pH corrector was made with another 40 l bucket ([Supplementary Figure 2](#)). A 15 l bucket was used for mixing PA to the fluoride contaminated water and for feeding the reactor. However, it was observed later that a simple sand–gravel filter also gave the same result as that of the four-layered filters, and therefore the four-layered filters were replaced by simple sand–gravel filters for the other units installed in the villages.

Dose optimization and pre-assessment of performance

A small replica of the field units was set up in the laboratory for optimization of dose of PA and pre-assessment of the performance of the field units using feed water collected from the field water source of the small community unit. This groundwater supplied by the Public Health Engineering Department, Government of Assam, had fluoride concentration ranging between 5.0 and 4.6 mg/l during the year. Three low-density polyethylene containers were used as mixer, reactor and four-layered filter-cum-pH corrector to make the replica unit ([Supplementary Figure 3](#)).

Procedure

Fluoride-contaminated field water, after mixing with appropriate amount of PA, was fed to the reactor and kept for a residence time of 3 h. After 3 h, the water was transferred to the filter. The first time-treated water occupied the void volume of the filter-cum-pH corrector and therefore, fluoride-free water could only be collected from the second treatment onwards, thus allowing enough residence time for the treated water to finally settle with a pH of 7.44–7.90.

Instrumental analysis

The concentrations of fluoride in water were determined using an Orion Multiparameter Kit (Orion 5 Star, pH-ISE-Cond-DO Benchtop) using a fluoride ion selective electrode. Total ionic strength adjustment buffer (TISAB-III) was used to control ionic strength and de-complex fluoride. The pH was determined using another Orion Multiparameter Kit with a pH electrode. The metal ions were determined using an atomic absorption spectrophotometer (AAS, Thermo iCE 3000 series, USA) fitted with a hydride vapour generator.

Results and discussion

Laboratory study

Optimization of PA dose: Defluoridation from groundwater with initial 4.8 ± 0.2 mg/l fluoride, collected from field source, was examined with 0.001 M $[PA]_0$ in the feed water to compare the results with those of the bench-scale pilot test reported earlier with synthetic fluoride containing water³⁸. Figure 1 shows the results of fluoride removal versus the number of batches of treatment (n). The fluoride removal was found to be somewhat poor initially, which started to improve after ten batches and showed further improvement after 16 batches. The observed initial poor defluoridation may be attributed to possible presence of CaO impurity in the limestone. The CaO impurity may neutralize a part of PA, decreasing the effective concentration of PA for fluoride removal. The alkalinity (as $CaCO_3$) in the field water was found to be 150 mg/l compared to 86 mg/l in the synthetic water used earlier. However, there was no noticeable change in defluoridation due to the higher alkalinity of field water compared to synthetic water. Similarly, there was no effect of presence of slightly higher concentrations of sulphate (60 mg/l) and chloride (20 mg/l) ions in field water compared those in the synthetic water (6.3 mg/l and 5.4 mg/l respectively). During the bench-scale pilot tests, we observed good fluoride removal right from the first batch with a higher $[PA]_0$ dosage of 0.01 M to the feed³⁸. Therefore, it was decided to pretreat the crushed lime-

stone bed with 0.01 M $[PA]_0$ before lowering the dose of feed PA to get a desirable effluent fluoride concentration of around 0.7 mg/l for healthy teeth and bones².

In order to determine the optimum $[PA]_0$ dose for field trial, fluoride was removed from the field water using the replica unit at different dose of $[PA]_0$. For this experiment, a limestone bed of 10–15 mm chip size was first pretreated with 0.01 M PA to neutralize any lime (CaO) present with limestone, followed by defluoridation with varying doses of $[PA]_0$ in the range 0.01–0.5 mM in the feed field water; Figure 2 presents the results. It was observed that in the presence of 0.01 M $[PA]_0$, fluoride was removed from 4.8 to 0.01 mg/l, which is much below the prescription of WHO for drinking water. On lowering $[PA]_0$ from 0.01 M to 0.7 mM, the effluent $[F^-]$ increased from 0.01 to 0.41 mg/l, still well below the prescription of WHO. On further reducing $[PA]_0$ to 0.6 mM, the effluent

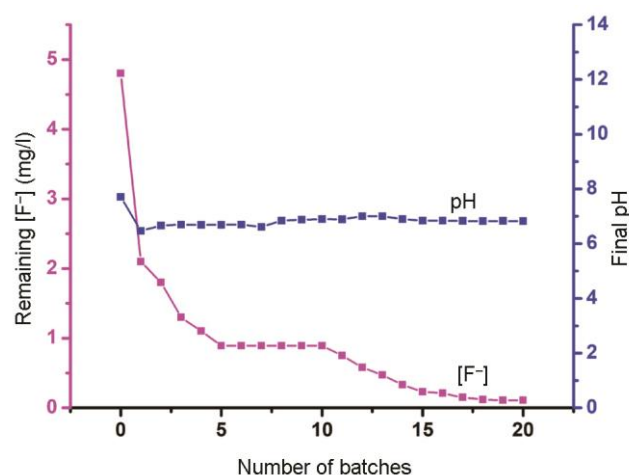


Figure 1. Plots of remaining $[F^-]$ with pH versus the number of batches used in PACLT for fluoride removal in the replica unit from field water with 0.001M $[PA]_0$. $[F^-]_0 = 4.8 \pm 0.2$ mg/l.

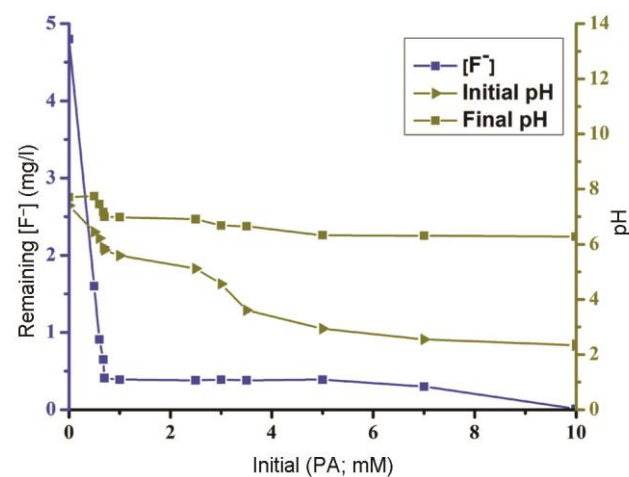


Figure 2. Plots of remaining $[F^-]$ and pH of water before (pH_0) and after (pH_f) treatment in the presence of varying $[PA]_0$ in the replica unit with field water having 4.8 ± 0.2 mg/l of $[F^-]_0$.

$[F^-]$ increased to 0.91 mg/l. Therefore, $[PA]_0$ of 0.68 mM, which gave an effluent $[F^-]$ of 0.65 mg/l, was chosen to be the optimum $[PA]_0$ for field trials.

The pH of field water, before and after treatment with $[PA]_0$ ranging from 0.01 M to 0.5 mM was measured (Figure 2). On decreasing $[PA]_0$ from 0.01 M to 0.68 mM, the initial pH of the feed water increased gradually from 2.34 to 5.89. The pH of the treated water increased after treatment in the crushed-limestone reactor, which increased further after passing through the four-layered sand-limestone-sand-gravel filter (Supplementary Figure 3). The effluent pH was below 6.5 with $[PA]_0$ between 0.01 M to 5.0 mM, which is lower than the minimum acceptable limit for drinking water, whereas it was above 6.5 with $[PA]_0$ below 3.5 mM. On the other hand, effluent $[F^-]$ of 0.91 mg/l and higher was detected with $[PA]_0$ of 0.6 mM and below (with an initial pH of 6.22 and above). However, both desirable effluent $[F^-]$ of 0.65 mg/l and acceptable pH of 7.37 for drinking purpose were achieved with $[PA]_0$ of 0.68 mM. Therefore, this optimum initial PA concentration was chosen for fixing the dose of $[PA]_0$ for the field trial as 0.463 ml of 8.5% PA per litre of water. However, for convenience of handling, rounded doses of 7 ml and 102 ml of 8.5% PA were used for 15 l household and 220 l small community units respectively.

Pre-assessment of performance: For a quicker assessment of the performance of field units, we examined the performance of the replica unit in the laboratory using fluoride-contaminated groundwater collected from the field source (Supplementary Figure 3). The pre-acidified influent water was poured into the crushed limestone reactor having 1.5 l void volume, allowed a residence time of 3 h and then filtered through a four-layered filter. Figure 3 shows the results. The effluent $[F^-]$ was within the acceptable range until breakthrough was observed after 250 batches. This means 83 l of defluoridated water was achieved per kilogram of limestone. The final pH of treated water was found to be in the range between 7.10 and 7.70 after passing through the four-layered filter.

Field trial

Performance of the small community field unit: For easy acceptability by the local users, the present fluoride removal method was named as Fluoride Nilogon. Figure 4 shows the results of fluoride removal and final pH of the water after removal of fluoride using the optimized dose of 0.68 mM $[PA]_0$ (102 ml of 8.5% PA in 220 l water) in the small community Fluoride Nilogon unit installed at Dengaon, Karbi Anglong district, on 15 March 2013. The effluent $[F^-]$ is consistent within 0.6–0.7 mg/l up to 579 batches in over 5½ years, showing no signs of depletion of the limestone till date. The small community

field unit has been showing remarkably better performance than the replica unit in the laboratory. It may be noted here that we used crushed limestone chips of size 10–15 mm in the replica unit test in the laboratory. Since it was impractical to choose such a narrow size range of chips for large quantities of limestone, chip sizes of 1–20 mm were used in the small community field unit. The better performance of the field units compared to the replica unit can be attributed to the presence of smaller chip size of limestone in the small community unit. Decrease in the particle size increases the surface area of limestone, thus increasing the removal of fluoride.

The pH of the influent field water was 5.89 with 0.68 mM $[PA]_0$. As the water enters the crushed limestone bed reactor, PA is neutralized by limestone³⁸. The pH of the effluent water from the four-layered filter of

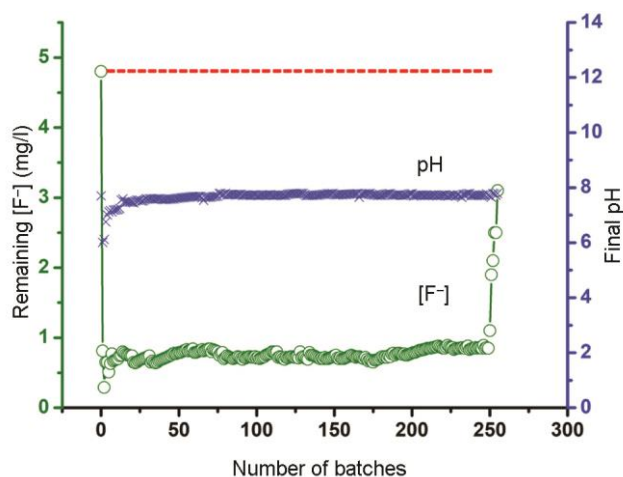


Figure 3. Plots of $[F^-]$ and pH of treated water versus number of batches for the replica unit $[F^-]_0 = 4.8 \pm 0.2$ mg/l (broken line), $[PA]_0 = 0.68$ mM and residence time = 3 h.

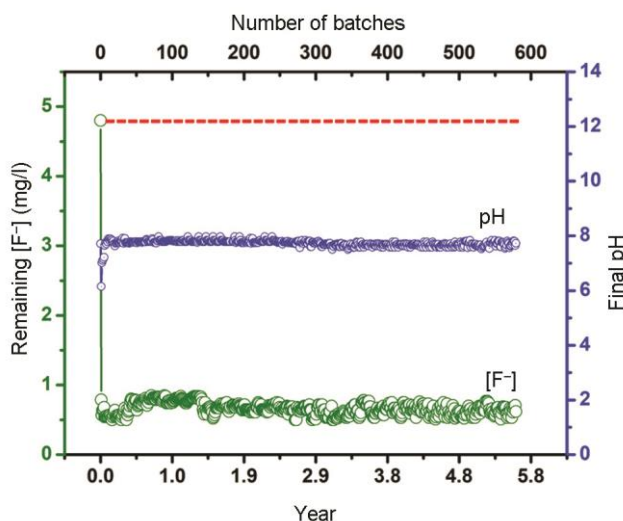


Figure 4. Plots of remaining $[F^-]$ and pH in treated water versus the number of batches and years of use for the small community field unit. $[F^-]_0 = 4.8 \pm 0.2$ mg/l (broken line), $[PA]_0 = 0.68$ mM and residence time = 3 h.

the small community field unit has been consistently found to be in the range 7.54–7.90, which is acceptable for drinking.

Performance of the household units: Figure 5 and [Supplementary Table 1](#) show the results of the remaining $[F^-]$ and final pH of the treated and filtered water for the household Fluoride Nilogon units with 15 l pore volume installed at the villages of Napakling (H1), Kehang Inlang (H2), Sarik Teron (H3) and Kat Tisso (H4). The results of another household unit installed in Napakling (H5) by a villager, trained by the present authors at Tezpur University, is also included in the figure. H1 was installed on 12 October 2014, while H2, H3 and H4 were installed on 6 December 2014 and H5 was installed on 15 October 2015. The $[F^-]_0$ in groundwater of the hand tubewell sources of H1, H2, H3, H4 and H5 was 5.0, 20, 2.8, 5.2 and 4.2 mg/l respectively. The procedure followed for operating the household units was the same as that for the small community unit. The dose of PA was 7 ml 8.5% PA in 15 l water and residence time of water in the reactor was 3 h.

It is interesting to note that the household Fluoride Nilogon units have been showing remaining $[F^-]$ in the range 0.50–0.80 mg/l consistently till date, for about four years and up to 4625 batches from the time of installation, thus meeting the WHO guideline value, without any sign of exhaustion of the limestone bed (Figure 5). The effluent pH was in the range 7.4–7.7, which is within the acceptable range pH for drinking water, i.e. 6.5–8.5. [Supplementary Table 1](#) also shows the average values of effluent $[F^-]$ and pH obtained from the community and five household systems. The average values were calculated considering all data collected till date. It was observed that in C1, H1, H2, H3, H4 and H5 units, where

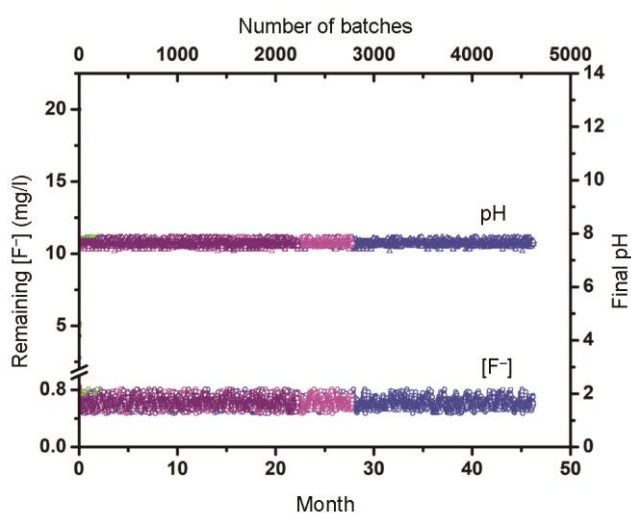
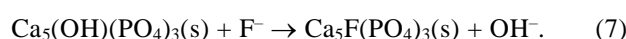
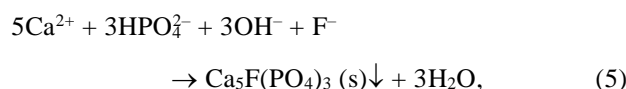
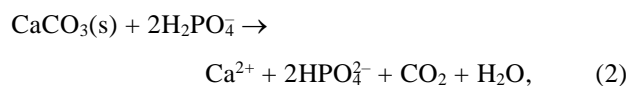


Figure 5. Results of $[F^-]$ before and after treatment along with final pH versus the number of batches for the household units: H1 (green), H2 (blue), H3 (magenta), H4 (red) and H5 (purple). $[PA]_0 = 0.68$ mM and residence time = 3 h.

$[F^-]_0$ was 4.8, 5.0, 20, 2.8, 5.2 and 4.2 mg/l respectively, the average effluent $[F^-]$ was 0.70, 0.62, 0.59, 0.55, 0.67 and 0.62 mg/l respectively, after treatment. More interestingly, the performance of the present method was found to be independent of initial $[F^-]_0$, at least up to 20 mg/l.

Mechanism of fluoride removal: The observed consistently good fluoride removal without needing any replenishment, regeneration or replacement of the crushed limestone bed for over 4625 batches of use and the method being independent of initial $[F^-]_0$ up to 20 mg/l may be attributed to the combined precipitation–adsorption mechanism of fluoride removal using PACLT method³⁸.

The following reactions have been proposed in the process of fluoride removal by limestone in the presence of PA³⁸.



Here, H_2PO_4^- ($\text{pK}_{a2} = 7.21$) overshadows HPO_4^{2-} ($\text{pK}_{a3} = 12.35$) in the pH range of treated water. The reactions of dissolution of CaCO_3 by the triprotic PA ($\text{pK}_{a1} = 2.12$), eq. (1), the precipitation of CaF_2 , viz. eq. (3) and the precipitation of FAP and HAP, viz. eq. (4–6) are completed rapidly. Due to this, the fluoride concentration in water comes down to about 2 mg/l within 3–4 min³⁸. Though FAP has a lower solubility product than that of HAP, high abundance of hydroxide ions in the system makes precipitation of HAP more favourable⁴⁰. The sorption or exchange of the remaining fluoride by HAP (eq. (7)) continues for a longer time as indicated by the continued increase in fluoride removal which lasts for about 3 h along with some adsorption of fluoride by the renewed limestone surface. Thus, it can be stated that defluoridation takes place predominantly through sorption of fluoride by *in situ*-formed HAP, in addition to precipitation of CaF_2 and FAP.

The continued consistent performance of the crushed limestone beds in the field units up to 4625 batches of use (Figure 5) is much better compared to the replica unit which showed breakthrough after 250 batches (Figure 3). This can be attributed to the difference in time interval between two consecutive batches in the field compared to that in the replica unit. While the replica unit was used for four batches a day with about 15 min interval between two batches, the field units were used at the most for two batches in a day and that too with at least 9 h interval between two batches. It is possible that the limestone surface gets enough time to dry and undergo some solid-state reactions increasing porosity or exposure at the surface, which favours dissolution of limestone and subsequent reactions in the next batch. This, however, remains to be verified experimentally. If it is true, along with the fact that the quantity of limestone dissolved by PA (7 ml 8.5% H_3PO_4) per batch of 15 l of water, in a household Fluoride Nilogon unit, is 1.53 g (Supporting Information), the life of the crushed limestone bed of a household Fluoride Nilogon unit may ideally extend to 39,210 batches or 53 plus years. With the field experience till now, this does not seem unlikely.

Plots of average effluent $[\text{F}^-]$ versus total alkalinity as CaCO_3 of the source water indicate a weak positive correlation between the effluent $[\text{F}^-]$ and total alkalinity of the source water with R^2 of 0.901 (Figure 6). However, there is significantly lesser correlation ($R^2 = 0.543$) between the effluent pH and total alkalinity as CaCO_3 , except at slightly higher pH in the case of the small community unit. It may be noted here that the effluent pH is expected to increase with longer residence time. The effluent water of the small community unit had longer residence time in the filter, which slightly increased the pH.

Potability of treated water: Table 1 presents the relevant water quality parameters before and after treatment

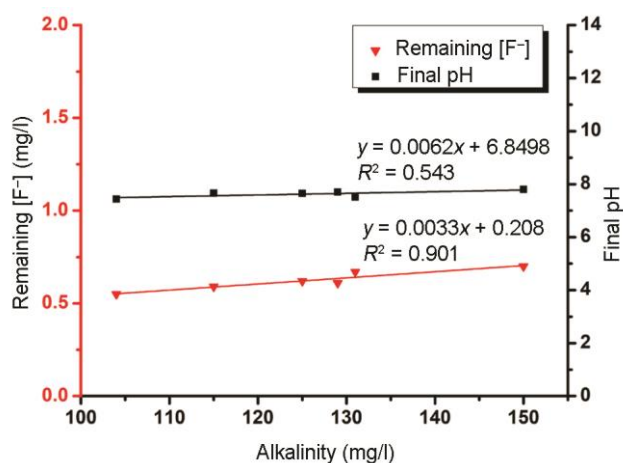


Figure 6. Plots of average value of remaining $[\text{F}^-]$ and final pH of treated water of six field units versus the total alkalinity as CaCO_3 of the influent water.

measured by standard methods⁴¹. All the parameters after treatment were within the respective WHO guideline values for drinking water². The concentration of most of the metal ions decreased after treatment, which may be attributed to low solubility of metal phosphates in water. The concentration of Ca^{2+} and PO_4^{3-} also remained within the WHO guideline values.

Suitability of the method

Capacity of limestone: Analysis of the composition of the precipitate collected from the bottom of the reactor chamber of the replica unit using a spatula, has shown the presence of HAP, FAP and CaF_2 , which is consistent with the results reported earlier³⁸. The performance of the field units indicates high capacity of limestone in Fluoride Nilogon. However, calculation of the actual capacity is not yet possible as the limestone bed of the community unit has been working consistently for over 579 batches (and 5½ years). Given the field experience, we can assume limestone to work consistently till the entire quantity is dissolved by PA. Considering the use of 7 ml of 8.5% PA twice a day for a household unit, the total number of batches that will be required to dissolve 60 kg (the quantity of limestone required to fill a 40 l drum) of limestone turns out to be 39,210. This means that the limestone bed may work up to a maximum of 53.7 years without needing replacement. This estimate is justified as the limestone beds of the household field units have been working consistently over 4625 batches or about four years. Taking the fluoride removed per batch of a household unit as 19.3 mg/l from the initial 20 mg/l, the estimated capacity of fluoride removal till total exhaustion of the limestone turns out to be 252.2 mg/g. This is incomparable to the capacity of limestone alone (0.39 mg/g)⁴², activated alumina (1.08 mg/g)⁴³, activated carbon (1.10 mg/g)⁴⁴, bone char (1.4 mg/g)⁴⁵ and HAP nanoparticles (5.5 mg/g)⁴⁶.

Cost estimation: For estimation of the recurring cost incurred in Fluoride Nilogon, one needs to take only the cost of PA into account. The cost of limestone can be included in capital cost as it has almost unlimited lifetime, as mentioned in the previous section. There is no maintenance cost of the units. Thus, considering the market retail price of 85% PA as Rs 100, the recurring cost of the treatment turns out to be Rs 0.00467/l (USD 0.000063) of treated water, which is much lower than that of RO (\approx Rs 0.54 considering Rs 6000 for annual maintenance and 30 l water consumption per day) and any adsorption-based fluoride filters. The capital cost includes only the cost of two plastic containers of desired size, two taps, crushed limestone, sand and gravel. The capital cost turns out to be Rs 600 (USD 8.51) and Rs 4500 (USD 61.12) for the household and small community Fluoride Nilogon units respectively ([Supporting Information](#)).

Table 1. Relevant water quality parameters before and after treatment by PACLT

Parameter (mg/l except for pH)	WHO guidelines value	Before treatment	After treatment
pH	6.50–8.50 ^a	7.40	7.3–7.5
Dissolved solids	600	175	240
Suspended solids	NS ^b	12	8
Total alkalinity as CaCO ₃	200	150	154
Total hardness as CaCO ₃	200	154	160
Phosphate	NS	0.135	0.109
Sulphate	500	60	62
Chloride	250	20	7
Nitrate	50	0.45	0.27
Cadmium	0.003	<0.001	<0.001
Calcium	50	10.78	12.13
Chromium	0.05	ND ^c	ND
Cobalt	NS	ND	ND
Copper	2.0	<1.00	<1.00
Lead	0.01	<0.001	<0.001
Magnesium	NS	2.81	3.40
Manganese	0.40	<0.001	<0.001
Zinc	3.0	2.5	0.07
Sodium	200	94.69	85.96
Potassium	NS	4.22	3.12
Iron	0.30	0.013	<0.001

[PA]₀ = 0.68 mM; [F⁻]₀ = 4.8 ± 0.2 mg/l; Source of water sample: piped water supply by PHED.

^aAcceptable range for drinking; ^bNS, Not specified and ^cND, Not detectable.

Sludge disposal: A toxicity characteristic leaching procedure test prescribed by the United States Environmental Protection Agency (US EPA) was performed on the precipitate produced in the reactor, which showed only 0.35 mg/l fluoride in the leachate. Thus, leaching from the sludge of Fluoride Nilogon is 429 times lower than the maximum permissible limit of 150 mg/l allowed for land-fill dumping by US EPA^{47,48}. The very low leaching from the sludge may be attributed to the strong binding of F⁻ in FAP. The solid sludge can be easily disposed of in landfills or buried in other safe places like construction sites. However, the question of sludge disposal may not arise now, as the limestone bed is still in a good condition even after 4625 batches of use, and ideally the life of the limestone bed may extend over 53 years.

User satisfaction and present status: Limestone, a low-cost sedimentary rock, is readily available in most of the fluoride-affected areas of the world, including India⁴⁹. In Assam, limestone mines are present in the vicinity of its severely fluoride-affected areas of West Karbi Anglong and Hojai districts. PA is approved by the US EPA for application in water purification⁴⁷. PA is also easily acceptable to people as it is an edible acid used in popular beverages and for preserving packaged food. The treated water does not leave any objectionable odour or colour. Moreover, PA being a weak acid is easy to handle. However, in the present field study, PA has been dispensed to the rural users after ten times dilution from the original strength of 85% (W/V) for further safety.

That the users are satisfied with the Fluoride Nilogon is indicated by continuation of the field trial units by

them for over five and half years continuously. There is an increasing desire of the affected people to acquire a household unit of their own. Government restrictions on procurement of limestone are however a great deterrent faced by the villagers. Despite that, there are six small community and 35 household Fluoride Nilogon units at present in West Karbi Anglong district, most of which have been installed by trained local people. With involvement of various individuals and government and non-governmental organizations, e.g. Karbi Anglong Autonomous Council, National Programme for Prevention and Control of Fluorosis, and Art of Living, Fluoride Nilogon is set for implementation in a big way soon in Karbi Anglong.

Conclusion

The present field study proves that Fluoride Nilogon, is a good rural technology for fluoride removal. The method involves pre-mixing of fluoride-contaminated water with a dose of 0.463 ml of 8.5% PA/l of water to give a concentration of 0.68 mM of PA in water, subsequent treatment of the water in a fixed-bed crushed limestone reactor of chip size 1–20 mm for 3 h, and then sand-gravel filtration. The crushed limestone bed needs to be pretreated with 0.01 M PA. The method removes excess fluoride efficiently from as high as 20 mg/l to a desired level of 0.7 mg/l. The removal is independent of the initial [F⁻] and a higher dose of PA can totally remove fluoride. The pH of the treated water remains within 7.4–7.9, which is in the middle of the acceptable range of

6.5–8.5 for drinking. All other relevant water quality parameters for the treated water remain within the guideline values of WHO.

The field units have been working consistently over 4625 batches or 5½ years without needing any interventions like regeneration, replenishment or replacement of the limestone. The estimated life of the crushed limestone bed of a household Fluoride Nilogon unit used twice a day with 20 mg/l feed water is 39,210 batches or over 50 years. The recurring cost of the treatment which includes only the cost of PA is Rs 0.00467 (USD 0.000063)/l of treated water. This is much lower than any other fluoride removal methods. Requiring only two containers, two taps, limestone, sand and gravel, the capital cost of 15 l household and 220 l small community Fluoride Nilogon units is only Rs 600 (USD 8.51) and Rs 4500 (USD 61.12) respectively. Finally, it can be concluded from the present field experience that, high efficiency, high capacity of limestone, extremely low cost, safe, environment-friendliness, non-requirement of electricity, non-requirement of regeneration, replenishment or replacement of any part for years (possibly decades), simple enough to be operated by a layman and user satisfaction prove Fluoride Nilogon as a good rural technology to address the worldwide problem of excess fluoride in drinking water.

- Susheela, A. K., A treatise on fluorosis. Fluorosis Research and Rural Development Foundation, New Delhi, 2001.
- WHO, *Guidelines for Drinking-Water Quality*, Geneva, World Health Organization, 2011, 4th edn, pp. 370–371.
- Swarup, D. and Dwivedi, S. K., Environmental pollution and effects of lead and fluoride on animal health, Indian Council of Agricultural Research, New Delhi, 2002.
- Edmunds, M. and Smedley, P., Fluoride in natural waters. In *Essentials of Medical Geology, Impacts of Natural Environment on Public Health*, Elsevier Academic Press, London, UK, 2005.
- Ali, S., Thakur, S. K., Sarkar, A. and Shekhar, S., Worldwide contamination of water by fluoride. *Environ. Chem. Lett.*, 2016, **14**, 291–315.
- Dutta, R. K., Saikia, G., Das, B., Bezbaruah, C., Das, H. B. and Dube, S. N., Fluoride contamination in groundwater of central Assam, India. *Asian J. Water Environ. Pollut.*, 2006, **2**, 93–100.
- Das, B., Talukdar, J., Sarma, S., Gohain, B., Dutta, R. K., Das, H. B. and Das, S. C., Fluoride and other inorganic constituents in groundwater of Guwahati, Assam, India. *Curr. Sci.*, 2003, **85**, 657–661.
- BIS, Indian Standard Specification for Drinking Water, IS 10500, Bureau of Indian Standards, New Delhi, 1991, pp. 2–4.
- Mohapatra, M., Anand, S., Mishra, B. K., Giles, D. E. and Singh, P., Review of fluoride removal from drinking water. *J. Environ. Manage.*, 2009, **91**, 67–77.
- Maheshwari, R. C., Fluoride in drinking water and its removal. *J. Hazard. Mater.*, 2006, **137**, 456–463.
- Bhatnagar, A., Kumar, E. and Sillanpaa, M., Fluoride removal from water by adsorption – a review. *Chem. Eng. J.*, 2011, **171**, 811–840.
- Nawlakhe, W. G., Kulkarni, D. N., Pathak, B. N. and Bulusu, K. R., Defluoridation using the Nalgonda technique in Tanzania. *Indian J. Environ. Health*, 1975, **17**, 26–65.
- Ndiayea, P. I., Moulin, P., Dominguez, L., Millet, J. C. and Charbit, F., Removal of fluoride from electronic industrial effluent by RO membrane separation. *Desalination*, 2005, **173**, 25–32.
- Vasudevan, S., Lakshmi, J. and Sozhan, G., Studies on a Mg–Al–Zn alloy as an anode for the removal of fluoride from drinking water in an electrocoagulation process. *Clean-Soil Air Water*, 2009, **37**, 372–378.
- Lhassani, A., Rumeau, M., Benjelloun, D. and Pontie, M., Selective demineralization of water by nanofiltration application to the defluorination of brackish water. *Water Res.*, 2001, **35**, 3260–3264.
- Viswanathan, N. and Meenakshi, S., Selective fluoride adsorption by a hydrotalcite/chitosan composite. *Appl. Clay Sci.*, 2010, **48**, 607–611.
- Meenakshi, S. and Viswanathan, N., Identification of selective ion-exchange resin for fluoride sorption. *J. Colloid Interface Sci.*, 2007, **308**, 438–450.
- Wang, J., Kang, D., Yu, X., Ge, M. and Chen, Y., Synthesis and characterization of Mg–Fe–La trimetal composite as an adsorbent for fluoride removal. *Chem. Eng. J.*, 2015, **264**, 506–513.
- Fan, X., Parker, D. J. and Smith, M. D., Adsorption kinetics of fluoride on low cost materials. *Water Res.*, 2003, **37**, 4929–4937.
- Turner, B. D., Binning, P. and Stipp, S. L. S., Fluoride removal by calcite: evidence for fluorite precipitation and surface adsorption. *Environ. Sci. Technol.*, 2005, **39**, 9561–9568.
- Murutu, C., Onyango, M. S., Ochieng, A. and Otieno, F. A. O., Fluoride removal performance of phosphoric acid treated lime: breakthrough analysis and point-of-use system performance. *Water SA*, 2012, **38**, 279–285.
- Thole, B., Mtalo, F. and Masamba, W., Groundwater defluoridation with raw bauxite, gypsum, magnesite, and their composites. *Clean-Soil Air Water*, 2012, **40**, 1222–1228.
- Mourabet, M., El Boujaady, H., El Rhilassi, A., Ramdane, H., Bennani-Ziatni, M., El Hamri, R. and Taitai, A., Defluoridation of water using brushite: equilibrium, kinetic and thermodynamic studies. *Desalination*, 2011, **278**, 1–9.
- Maiti, A., Basu, J. K. and De, S., Chemical treated laterite as promising fluoride adsorbent for aqueous system and kinetic modeling. *Desalination*, 2011, **265**, 28–36.
- Asgari, G., Roshani, B. and Ghanizadeh, G., The investigation of kinetic and isotherm of fluoride adsorption onto functionalize pumice stone. *J. Hazard. Mater.*, 2012, **217**, 123–132.
- Raichur, A. M. and Basu, M. J., Adsorption of fluoride onto mixed rare earth oxides. *Sep. Purif. Technol.*, 2001, **24**, 121–127.
- Li, Y. H. et al., Adsorption of fluoride from aqueous solution by graphene. *J. Colloid Interf. Sci.*, 2011, **363**, 348–354.
- Huang, R. H., Yang, B. C., Liu, Q. and Ding, K. L., Removal of fluoride ions from aqueous solutions using protonated cross-linked chitosan particles. *J. Fluorine Chem.*, 2012, **141**, 29–34.
- Lounici, H., Addour, L., Belhocine, D., Grib, H., Nicolas, S., Bariou, B. and Mameri, N., Study of a new technique for fluoride removal from water. *Desalination*, 1997, **114**, 241–251.
- Nigussie, W., Zewge, F. and Chandravanshi, B. S., Removal of excess fluoride from water using waste residue from alum manufacturing process. *J. Hazard. Mater.*, 2007, **147**, 954–963.
- Murutu, C. S., Onyango, M. S., Ochieng, A. and Otieno, F. A., Investigation on limestone derived apatite as a potential low cost adsorbent for drinking water defluoridation; http://www.Ewisa.Co.Za/literature/files/148_101%20murutu.Pdf (accessed on 10 October 2018).
- Reardon, E. J. and Wang, Y., A limestone reactor for fluoride removal from wastewaters. *Environ. Sci. Technol.*, 2000, **34**, 3247–3253.
- Gogoi, S. and Dutta, R. K., Mechanism of fluoride removal by phosphoric acid-enhanced limestone: equilibrium and kinetics of fluoride sorption. *Desalin. Water Treat.*, 2016, **57**, 6838–6851.

34. Nath, S. K. and Dutta, R. K., Enhancement of limestone defluoridation of water by acetic and citric acids in fixed bed reactor. *Clean-Soil Air Water*, 2010, **38**, 614–622.
35. Nath, S. K. and Dutta, R. K., Fluoride removal from water using crushed limestone. *Indian J. Chem. Technol.*, 2010, **17**, 120–125.
36. Nath, S. K. and Dutta, R. K., Acid-enhanced limestone defluoridation in column reactor using oxalic acid. *Process Saf. Environ. Prot.*, 2012, **90**, 65–75.
37. Nasr, A. B., Walha, K., Puel, F., Mangin, D., Amar, R. B. and Charcosset, C., Precipitation and adsorption during fluoride removal from water by calcite in the presence of acetic acid. *Desalin. Water Treat. Prot.*, 2014, **52**, 2231–2240.
38. Gogoi, S., Nath, S. K., Bordoloi, S. and Dutta, R. K., Fluoride removal from groundwater by limestone treatment in presence of phosphoric acid. *J. Environ. Manage.*, 2015, **152**, 132–139.
39. Dutta, R. K. and Nath, S. K., A highly efficient defluoridation method by *in situ* generation of an efficient precipitant and strong adsorbents of fluoride in crushed limestone fixed-bed column and plug flow reactors. Indian Patent No. 2892204, 2017.
40. Narasaraju, T. S. B. and Rai, U. S., Some thermodynamic aspects of dissolution of solid solutions of hydroxylapatites of phosphorus and arsenic. *Can. J. Chem.*, 1979, **57**, 2662–2664.
41. APHA, *Standard Methods for the Examination of Water and Wastewater*, American Public Health Association, New York, USA, 17th edn, 1998.
42. Biswas, K., Gupta, K. and Ghosh, U. C., Adsorption of fluoride by hydrous iron(III)–tin(IV) bimetal mixed oxide from the aqueous solutions. *Chem. Eng. J.*, 2009, **149**, 196–206.
43. Maliyekkal, S. M., Sharma, A. K. and Philip, L., Manganese oxide-coated alumina: a promising sorbent for defluoridation of water. *Water Res.*, 2006, **40**, 3497–3506.
44. Ramos, R. L., Ovalle-Turrubiarres, J. and Sanchez-Castillo, M. A., Adsorption of fluoride from aqueous solution on aluminum-impregnated carbon. *Carbon*, 1999, **37**, 609–617.
45. Dahi, E. and Nielsen, J. M., In Proceedings of the 2nd International Workshop on Fluorosis Prevention and Defluoridation of Water, Ethiopia, 19–25 November 1997.
46. Poinern, G. E. J., Ghosh, M. K., Ng, Y. J., Issa, T. B., Anand, S. and Singh, P., Defluoridation behavior of nanostructured hydroxyapatite synthesized through an ultrasonic and microwave combined technique. *J. Hazard. Mater.*, 2011, **185**, 29–37.
47. <http://www.Epa.Gov/osw/hazard/wastetypes/wasteid/inorchem/docs/phosphor.pdf>
48. US EPA, Method 1311: Toxicity characteristic leaching procedure, US Environmental Protection Agency, Washington, DC, 1992.
49. Nath, S. K. and Dutta, R. K., Significance of calcium containing materials for defluoridation of water: a review. *Desalin. Water Treat.*, 2015, **53**, 2070–2085.

ACKNOWLEDGEMENTS. We thank Bokajan Cement Factory of Cement Corporation of India, Bokajan, Assam, for gifts of several tonnes of limestone and the Department of Science and Technology (Water Technology Initiative), New Delhi for financial support (DST/TM/WTI/2K16/95 dated 15/6/2017). Deneb Instruments, Kolkata gifted us a Fluoride ISE. S. G. and S. B. thank CSIR, New Delhi for SRF fellowships. R. M. and A. J. B. thank Tezpur University for institutional fellowships. We are grateful to the users for their interest and cooperation. R. K. D. thanks his friends who extended a helping hand, including financial support, in the field trial.

Received 5 October 2018; revised accepted 17 September 2019

doi: 10.18520/cs/v118/i2/255-263



Synthesis of biochemically reduced graphene-oxide/Fe⁰ containing polyaniline ternary hybrid composite through interfacial polymerization for supercapacitors

BISWAJIT PEGU¹, SHREEMOYEE BORDOLOI^{1,2}, RATAN BORUAH³ and SURAJIT KONWER^{1,*} 

¹Department of Chemistry, Dibrugarh University, Dibrugarh 786001, India

²Department of Chemistry, MDKG College, Dibrugarh 786004, India

³Department of Physics, Tezpur University, Tezpur 784028, India

*Author for correspondence (surajitkonwer@dibru.ac.in)

MS received 3 January 2021; accepted 16 June 2021

Abstract. A novel electrode material for supercapacitor has been developed based on biochemically reduced graphene oxide/zerovalent iron (rGO/Fe⁰) and polyaniline (PANI) ternary hybrid composite synthesized by interfacial polymerization. The composites were characterized by Fourier transform infrared spectroscopy (FTIR), scanning electron microscopy (SEM), ultraviolet–visible absorption (UV–Vis), X-ray diffraction (XRD), X-ray photoelectron spectrum (XPS) and electrical conductivity measurements. The composites exhibited noticeable improvement in electrical conductivity and excellent electrochemical reversibility when compared to bare polymer. The electrochemical properties of the composite electrode are investigated by galvanostatic charge–discharge, electrochemical impedance spectroscopy (EIS) studies. The enhanced specific capacitance with higher conductivities is observed in PANI/rGO/Fe⁰ (342 F g⁻¹) when compared with PANI (182 F g⁻¹) and PANI/rGO composites (294 F g⁻¹) with a constant current density of 1.0 A g⁻¹. The cyclic stability of the composite, following 500 cycles of operations, was at 68.6 (PANI), 80.6 (PANI/rGO) and 95.4% (PANI/rGO/Fe⁰) of their initial capacitance. The higher conductivity, higher specific capacitance and cyclic self-stability of PANI/rGO/Fe⁰ ternary composite can provide new prospects in the field energy storage application.

Keywords. Polyaniline; biochemical reduction; graphene oxide; capacitance; ternary composite.

1. Introduction

In recent years, the rising of environmental crisis due to carbon dioxide emission and depletion of fossil fuels; leads to the development of efficient, low-cost, environment friendly and sustainable energy storage devices, such as supercapacitors, fuel cells, high-energy batteries, etc., which has become one of the greatest challenges for the researchers [1–3]. Electrochemical supercapacitors are considered as one of the next generation energy-storage devices owing to its high-power density, fast charging–discharging, excellent cycling performance and long lifetime [4–6].

Reduced graphene oxide (rGO) bearing various oxygen functional groups on their basal planes and edges, has received a rapidly growing research interest [7–16]. Though, electrical conductivity of rGO individually is very poor, the fabrication of rGO in electrically active material is limited by the presence of highly electrical resistant groups like carboxyl, hydroxyl, or epoxy in rGO sheets. Many researchers have tried to combine the GO with various

metal nanoparticle-based binary composites or their ternary composites with conducting polymers for improving their electrical and electrochemical properties [17–33].

Various attempts have been made to develop efficient electronically conducting polymer (viz. polyaniline, polypyrrole, polythiophene, etc.)-based electrode materials in supercapacitors. In the family of various conducting polymers, polyaniline is one of the most promising conducting polymers for supercapacitors due to its high conductivity, multi-redox behaviour, low-cost and high flexibility, tremendous environmental and chemical stabilities [34–36].

There is another major challenge in the research and development for using zero valent iron (Fe⁰) for the preparation of suitable composites due to rapid aggregation [37] and short lifespan in water because the Fe⁰ nanoparticles are oxidized easily to form external oxide layers [38]. To overcome these issues, the modification/stabilization of Fe⁰ in composite materials followed by enhanced mobility and stabilized reactivity is considered essential. Recently, porous carbon material, such as rGO with conducting polymers have attracted much attention as supporters,

owing to their high surface area and specific channel structure that could prevent oxidation and aggregation [39].

Herein, we report a new green route of preparation and surface modification of conducting polyaniline (PANI)-based biochemically reduced rGO/Fe⁰ ternary hybrid composite in which rGO and Fe⁰ nanoparticles are fabricated on the surface of polymerization. To the best of our knowledge, no previous work has been reported for preparing PANI/rGO/Fe⁰ ternary composites by this route. The rGO/Fe⁰-incorporated PANI composites are achieving good improvement in thermal, electrical, optical and electrochemical properties. The introduction of less amount of rGO/Fe⁰ into PANI is found to greatly enhance the properties of pristine polymer.

2. Experimental

2.1 Chemicals

Aniline was obtained from Aldrich Co. and used without further purification. The natural graphite flake of size (crystalline, 300 mesh, Alfa Aesar) from Shankar Graphites & Chemicals, New Delhi, India. Hydrochloric acid (HCl), sulphuric acid (H₂SO₄), nitric acid (HNO₃), sodium nitrate (NaNO₃), potassium permanganate (KMnO₄), hydrogen peroxide (H₂O₂), ferric chloride (FeCl₃) and potassium persulphate (K₂S₂O₈) were of analytical reagent grade chemicals (Merck) and used as received. Acetonitrile was obtained from Merck and purified by standard methods. For all the purposes, double-distilled water was used.

2.2 Preparation of tea leaf extract, GO and rGO

The fresh tea leaves used in this work were collected from local tea garden in Assam, a north eastern state of India. Two grams of crushed dried tea leaves were boiled with 100 ml of distilled water at 80°C for 1 h in 500 ml flask under reflux condition. The prepared solution was filtered to obtain tea leaves extract (figure 1a).

Graphene oxide (GO) was prepared from natural graphite powder using Hummers' method published elsewhere [15]. For purification, the final yellow brown coloured solution (figure 1b) was left for 24 h to settle down and then, water was drawn out and the precipitate was washed by rinsing and centrifuged with 0.1 N HCl, followed by distilled water for several times. Finally, the precipitate was dried at 50°C under vacuum and the GO was obtained as a grey powder.

The GO solution (0.5 mg ml⁻¹) was mixed with tea leaf extract solution in a ratio of 1:1 (volume ratio) in 500 ml flask and the mixture was then homogeneously heated to 90°C using water bath under reflux condition for 1 h. After about 15 min of heating, the colour of the solution gradually changes from brown to black which indicates the beginning of reduction of GO. When the solution becomes dark black



Figure 1. (a) Tea leaf solution, (b) GO solution and (c) rGO solution.

(figure 1c), it indicates the complete reduction of GO and the formation of rGO.

2.3 Preparation of PANI

Eight hundred milligrams of aniline and 20 ml of chloroform were mixed in a 50 ml beaker (solution A) and in another beaker, 2 g of initiator (FeCl₃) was dissolved in 10 ml of water and sonicated for 15 min (solution B). Solution B was added dropwise into solution A and a dark green coloured composite film developed gradually at the interface of these immiscible phases. The reaction was allowed to proceed for 24 h for completion. As the reaction progressed, the reaction mixture gradually turned black. The resulting mixture was then filtered, washed with water and ethanol several times and dried.

2.4 Preparation of PANI/rGO composite

Six grams of GO and initiator (0.5 g of FeCl₃) were dispersed in 20 ml of H₂O by sonication for 30 min. In another beaker, 0.8 ml aniline was dissolved in 20 ml chloroform and then, to this organic mixture, aqueous dispersion was added dropwise. A dark green coloured composite film developed gradually at the interface and after 30 min, 15 ml of tea leaf extract was added under N₂ atmosphere. As the reaction progressed, the mixture became black and the reaction was allowed to proceed for 24 h for the completion of reduction of GO. Finally, the resulting mixture was filtered and washed with ethanol and water several times and the black solid was collected. The product was dried in vacuum to get PANI/rGO.

2.5 Preparation of PANI/rGO/Fe⁰ ternary hybrid composite

In this process, first, required amounts (6 g) of GO and FeCl₃ were dispersed in 20 ml of H₂O by sonication for 30 min. In another reaction vessel, aniline monomer (0.8 ml) is dissolved in 20 ml chloroform which formed the organic phase. Then, to this organic mixture, aqueous dispersion was added dropwise. A dark green coloured composite film developed gradually at the interface of these immiscible phases. After 30 min, 15 ml of tea leaf extract was added to the above solution under N₂ atmosphere which led to the formation of rGO and reduced form of iron (Fe⁰) on the matrix of polymer. As the reaction progressed, the mixture became black and the reaction was allowed to proceed for 24 h for the completion of reduction of GO and the remaining FeCl₃. Finally, the resulting mixture was filtered and washed with ethanol and water for several times and the black solid was collected. The product was dried in vacuum to get PANI/rGO/Fe⁰ composite.

2.6 Preparation of supercapacitor electrodes

About 5 mg of the prepared composite was mixed with Nafion solution coated by stainless-steel net with 1 cm² area and then, dried at 100 °C for 10 h and was used as a working electrode. Supercapacitor setup was designed by using a separator immersed in 1 M H₂SO₄ electrolyte solution placing between tightly pressed two electrodes and stainless-steel wires were used as current collectors.

2.7 Characterization

Fourier transform infrared (FTIR) spectra were analysed by Impact 410, Nicolet, USA, in a frequency range of 4000–500 cm⁻¹. X-ray diffraction (XRD) analysis was performed using Rigaku X-ray diffractometer at the scan rate of 0.05 θ s⁻¹. Raman analysis was carried out by Nanofinder 30 confocal Raman employing He–Ne laser beam (λ = 532 nm). Scanning electron microscope (SEM) analysis was taken by JSM-6390LV, JEOL, Japan. The ultraviolet–visible (UV–Vis) absorption spectroscopy of the samples in 1-methyl-2-pyrrolidone solvent was recorded using Shimadzu UV-2550 UV–Vis spectrophotometer. X-ray photoelectron spectrum (XPS) was performed at ACMS, IIT Kanpur, on an XPS-AES module, model: PHI 5000Versa Pro II, FEI Inc. The electrical conductivity of the samples was measured with a Four-probe method (300 K ≤ T ≤ 413 K) using the following equations:

$$\text{Resistivity } (\rho, \text{ ohm-cm}) = (V/I) 2\pi d, \quad (1)$$

$$\text{Conductivity } (\sigma, \text{ S cm}^{-1}) = 1/\rho, \quad (2)$$

where *V* is the applied voltage, *I* the measured current and *d* the distance between the probes.

Current–voltage (*I–V*) characteristics of the prepared samples were recorded by Keithley 2400 source meter at the room temperature in the frequency range of 10²–10⁶ Hz and at the scan rate of 0.1 V s⁻¹. The electrochemical behaviour of the prepared samples was studied using Sycopel AEW2-10 cyclic voltammeter.

2.7a Electrochemical analysis: Cyclic voltammetry (CV) of the sample was studied using Sycopel AEW2-10 cyclic voltammeter at scan rates between 10 and 100 mV s⁻¹ and it was performed in a three-electrode cell where the composite, platinum and saturated calomel electrode (SCE) electrodes were used as a working, counter and reference electrodes, respectively. The galvanostatic charge–discharge test was performed in a two-electrode system by Autolab PGSTAT302N with the current density range between 1 and 6 A g⁻¹. Specific capacitance (*C_S*) was measured from the charge–discharge method by the following equation [29]:

$$C_S = (I \times S_t) / (m \times S_V), \quad (3)$$

where *I*, *S_t*, *S_V* and *m* are the discharge current, discharge time, voltage drop and the weight of active material (5 mg) per electrode, respectively. Electrochemical impedance spectroscopy (EIS) was performed using Gamry EIS300 analyzer with the frequency range of 10⁻¹–10⁵ Hz (AC voltage, 5 mV).

3. Results and discussion

3.1 FTIR analysis

FTIR spectra of GO, rGO, PANI and PANI/rGO/Fe⁰ composites are revealed in figure 2. In GO, the characteristic O–H peak at 3430 cm⁻¹, strong C=O peak in carboxylic acid and carbonyl moieties at 1720 and 1630 cm⁻¹, respectively, are shown. C–OH peak at 1395 cm⁻¹ and the appearance of the peak at around 1070 cm⁻¹, confirm the presence of epoxy group in GO. In the FTIR spectrum of rGO, the peaks at 1630 and 3426 cm⁻¹ represent carbonyl moieties and O–H stretching vibration, respectively. Disappearance of the peak for carbonyl group at 1720 cm⁻¹ indicates that GO is reduced to rGO.

PANI shows peaks at 3450 and 1420 cm⁻¹ due to the N–H and C–N stretching vibrations of aniline. The peak at 2930 cm⁻¹ corresponds to aromatic sp² CH stretching. The C=C stretching deformation of the quinoid ring in the emeraldine salt and benzenoid rings in leucoemeraldine are depicted at 1728 and 1630 cm⁻¹, respectively. FTIR spectrum of the composite shows peaks associated with both PANI and rGO. The presence of PANI characteristic vibrations, suggesting PANI can be successfully deposited on the rGO/Fe⁰ surface. The shifting of the peaks towards lower wavelength with low peak intensity for the composite compared to pure PANI signifies successful inclusion of rGO/Fe⁰ in PANI matrix.

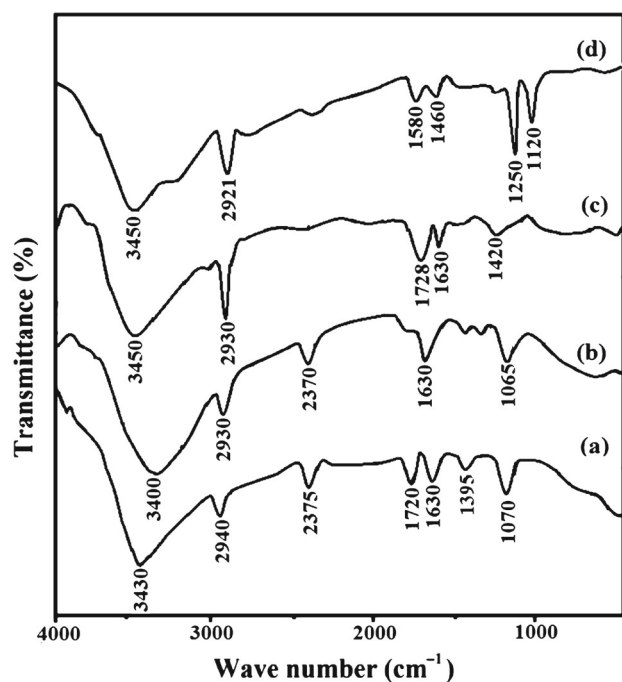


Figure 2. FTIR of (a) GO, (b) rGO, (c) PANI and (d) PANI/rGO/Fe⁰.

3.2 X-ray diffraction

Figure 3 shows XRD pattern of PANI, GO and PANI/rGO/Fe⁰ composites. A characteristic broad peak of amorphous PANI was observed at about $2\theta = 25.8^\circ$. The XRD pattern of GO, a broad reflection with peak at $2\theta = 13.1^\circ$ corresponding to the (0 0 1) diffraction peak, which indicates a typical loose layer-like structure. The 2θ value corresponds to an interlayer spacing (I_c) of about 0.63 nm, which might depend on the method of preparation and on the number of layers of water in the gallery space of the material. This indicates the formation of layer-like GO sheets.

For the PANI/rGO/Fe⁰ composite, the sharp peaks are observed where the characteristic peaks of PANI at 26.9° and the diffraction peaks at $2\theta = 55.2^\circ$ match the (111) and (222) planes of rhombohedral system with rhomb-centred lattice (ref. no. PCPDFWIN 75-2078 and calculated from ISCD using POWD-12++ (1997)). The crystalline peaks observed in the composite are due to the dominant crystalline nature of rGO and Fe⁰ particles. This indicates the successful incorporation of rGO, iron over polymer matrix.

3.3 Raman analysis

Figure 4 shows the Raman spectra of PANI/rGO/Fe⁰ composite and rGO sheets. In rGO, the corresponding peaks for D and G bands appear at 1328 and 1590 cm⁻¹, respectively. The peak intensity ratio between D and G bands (ID:IG) is found to be 1.19 for rGO which indicates that the defect structures are present and it was retained due to the removal

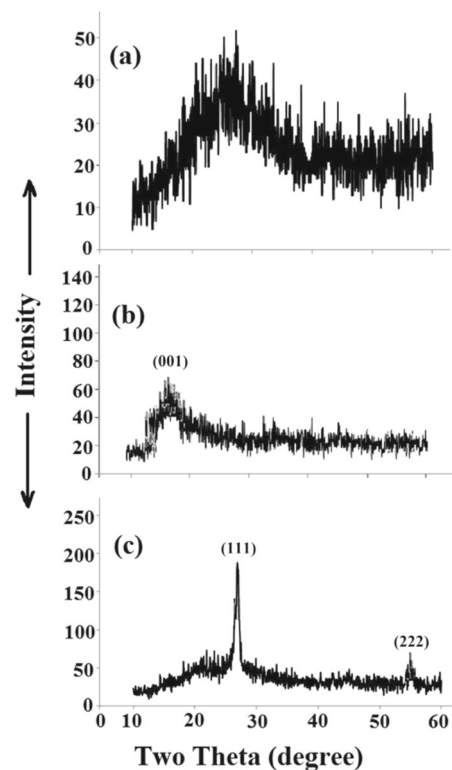


Figure 3. XRD analysis of (a) PANI, (b) GO and (c) PANI/rGO/Fe⁰ composites.

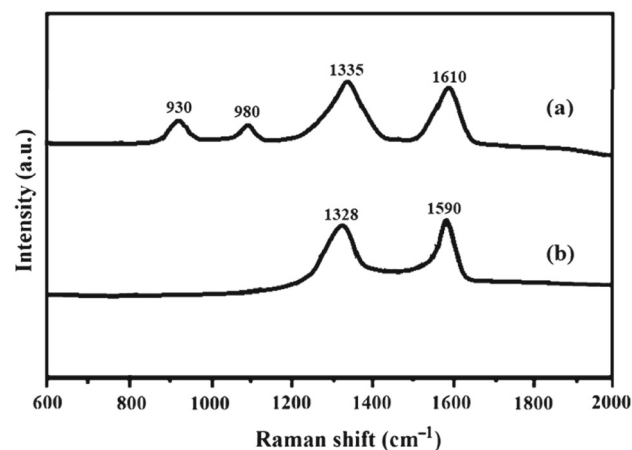


Figure 4. Raman spectra of (a) PANI/rGO/Fe⁰ composite and (b) rGO.

of functional groups during reduction. The characteristic peaks for PANI at 980 cm⁻¹ for polaron and 930 cm⁻¹ for bipolaron structure of PANI confirm that PANI is present in the composite. Moreover, shifting of the D and G bands to 1335 and 1610 cm⁻¹ in the composite indicates the π - π interaction between the two components. The intensity ratio, ID:IG of the composites was calculated to be 1.14, which indicates the presence of localized sp³ defects in the sp² carbon network structure. The results are well-consistent with FTIR results.

3.4 SEM study

The surface morphology of PANI, rGO and PANI/rGO/Fe⁰ composites were investigated by scanning electron micrographs of their powdered sample (figure 5). Pure PANI displays a randomly aggregated different crystal-like structures (figure 5a) and the flaky, layer-like structure of rGO is distinctly observed in SEM micrograph (figure 5b). In PANI/rGO/Fe⁰ composite, the morphological change clearly observed confirms the formation ordered PANI chain on the surface of the rGO/Fe⁰ sheets.

3.5 XPS analysis

XPS spectrum of the composite (figure 6) shows the binding energy peaks of Fe_{2p} centered at 711, 722 and 725 eV corresponding to 2p_{3/2} and 2p_{1/2}, of oxidized iron, i.e., (Fe(III)). Since in aqueous solution, Fe⁰ reacts with water and dissolved oxygen, there is a possibility of production of iron oxide (viz., ferrous hydroxide, ferric hydroxide, oxyhydroxides, lepidocrocite, maghemite and magnetite) depending on the redox as well as pH of the aqueous solution [40].

3.6 UV-Vis analysis

Figure 7 represents the UV-Vis absorption spectra of the PANI, PANI/GO and PANI/rGO/Fe⁰ composites recorded in NMP. The PANI/rGO/Fe⁰ composite shows an intense absorption peak at 315–320 nm and a broad peak at around 510–528 nm. The first absorption bands are related to the molecular conjugation (π - π^* transition), while the second absorption peak assigned to the polaron state of PANI in the synthesized PANI/rGO/Fe⁰ composites. However, all the PANI bands in PANI/rGO/Fe⁰ composites and the red shift due to the interaction of rGO and Fe⁰ particles into PANI matrix have been observed.

Absorption spectra of the polymers also enable to provide important information regarding its optical band gap. Attempts have been made to determine the optical band gap using the following equation.

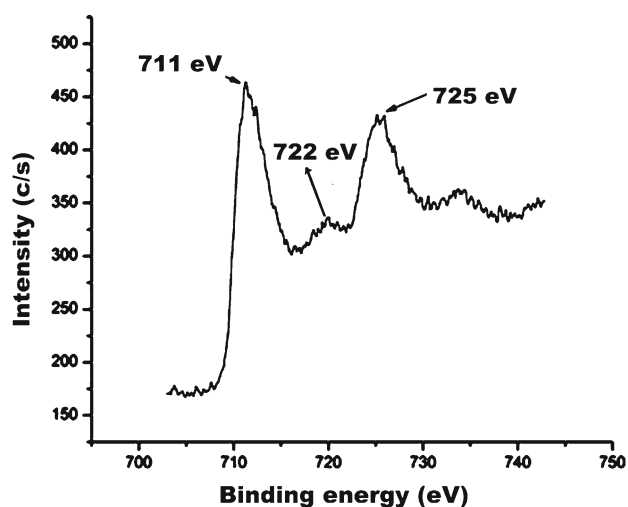


Figure 6. XPS spectra of PANI/GO/Fe⁰.

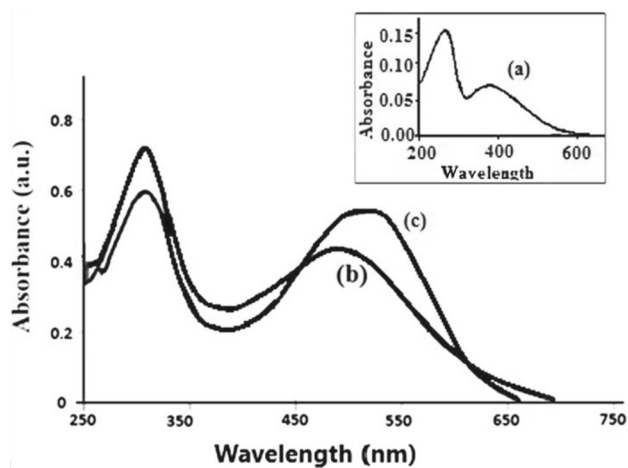


Figure 7. UV-Vis spectra of (a) PANI, (b) PANI/rGO and (c) PANI/rGO/Fe⁰.

$$E_g^{\text{opt}} \text{ (eV)} = 1240/\lambda_{\text{edge}} \text{ (nm)}, \quad (4)$$

where E_g^{opt} is the optical band gap of polymers and λ_{edge} is the absorption edge. The optical band gap of PANI, PANI/

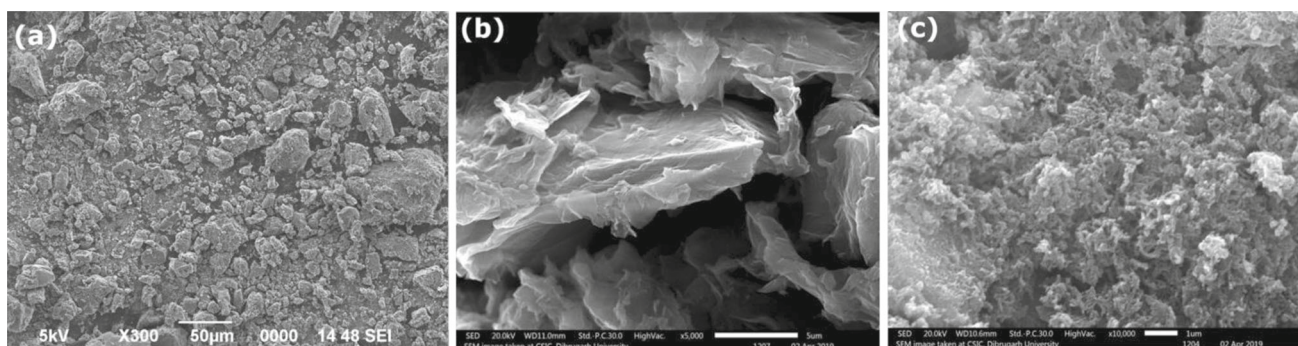


Figure 5. SEM images of (a) PANI, (b) rGO and (c) PANI/rGO/Fe⁰.

rGO and PANI/rGO/Fe⁰ are found to be 3.31, 2.43 and 2.35 eV, respectively.

3.7 Electrical conductivity

The conductivity of pristine PANI, PANI/rGO and PANI/rGO/Fe⁰ composites was varied widely in the range of 0.031–62 S m⁻¹ (table 1) with increased temperature. The conductivity decreases with increase in temperature up to 323 K, may be due to the removal of solvent and increases from 323 to 413 K, shows semiconducting behaviour of the polymer composites.

3.8 Electrochemical properties

3.8a CV study: CV test was conducted in a three-electrode system in 1 M H₂SO₄ electrolyte within a voltage range from -0.4 to 0.8 V (scan rate, 50 mV s⁻¹). Figure 8 illustrates the CV of PANI, rGO and PANI/rGO/Fe⁰ composite electrodes where rGO shows ideal electric double-layer (EDL) like capacitive behaviour with rectangular CV curve with very small area of the CV curve which may be due to the compact structure of rGO. In PANI, the CV curve exhibits reduction and oxidation peaks at around -0.33 and +0.45 V, respectively, indicating the pseudocapacitive nature of the polymer. In the ternary composite, a larger area with almost rectangular shaped cyclic voltammogram which indicates the ideal EDL capacitive nature as well as better charge transport behaviour than that of the pristine PANI and rGO.

Figure 9 shows the effect of scan rate (10–100 mV s⁻¹) on the electrochemical behaviour of PANI/rGO/Fe⁰ composite. As the scan rates increased from 10 to 100 mV s⁻¹, the slight negative and positive shifts of reduction and oxidation peaks, respectively, were observed which could be mainly due to the resistance of the electrode [41]. The clear redox peaks with every scan rate indicated its excellent rate capability as well as electrochemical behaviour in a wide range of scan rates.

Table 1. Conductivity of PANI and composites at various temperatures.

Temperature (K)	Conductivity (S m ⁻¹)		
	PANI	PANI/rGO	PANI/rGO/Fe ⁰
300	0.031	5.30	23.04
323	0.037	3.01	16.08
343	0.039	5.13	24.50
363	0.045	9.60	33.60
373	0.046	11.70	37.30
393	0.053	21.30	52.80
413	0.054	26.23	62.00

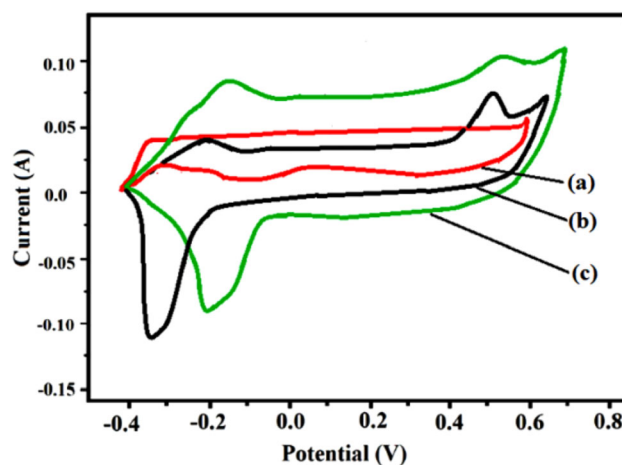


Figure 8. Cyclic voltammogram of (a) rGO, (b) PANI and (c) PANI/rGO/Fe⁰ in 1 M H₂SO₄ electrolyte at a scan rate of 50 mV s⁻¹.

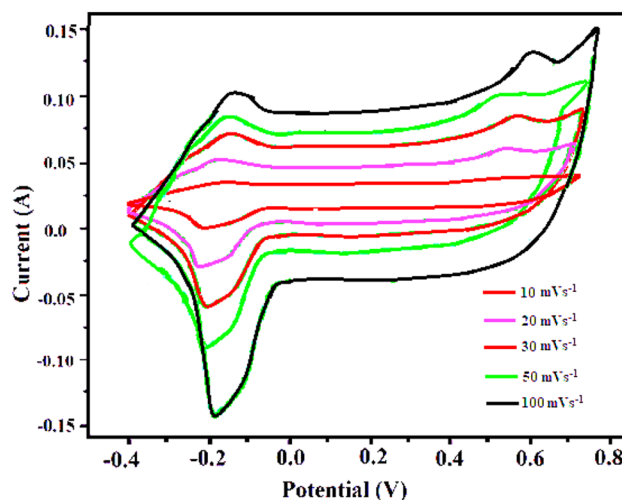


Figure 9. CV curves of PANI/rGO/Fe⁰ at various scan rates of 10, 20, 30, 50 and 100 mV s⁻¹.

3.8b EIS study: EIS study of electrodes in the form of Nyquist plots were obtained and fitted in the range of 20 kHz–100 mHz in 1.0 M H₂SO₄ (figure 10). The EIS diagrams showed nearly straight line at low frequency with a small, distorted semicircle at high frequencies. The diameter of the semicircle reveals the charge transfer resistance in PANI, and the nearly vertical line demonstrates the pseudocapacitive nature of PANI/rGO/Fe⁰ composites [42]. The lack of a separate semicircle in the diagrams represents a small charge transfer resistance at the electrode/electrolyte interface of the composite. In the Nyquist diagrams, the linear part of it, is closer to a vertical line along the imaginary axis and followed the order: PANI/rGO/Fe⁰ > PANI/rGO > PANI. This suggests that the ternary composite electrode is more capacitive than the PANI/rGO and PANI electrodes which is consistent with the CV results.

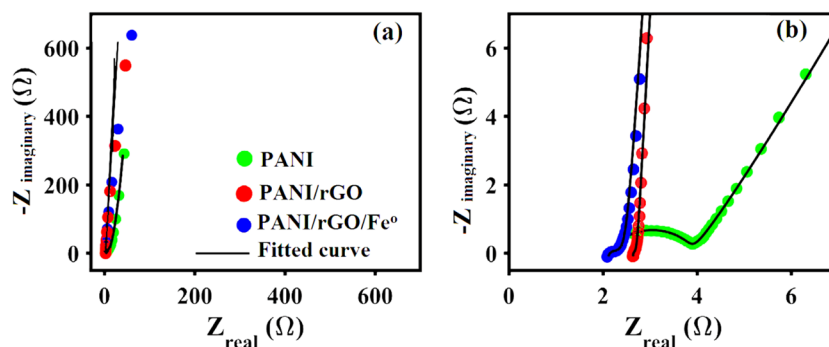


Figure 10. Nyquist plots of PANI, PANI/rGO and PANI/rGO/Fe⁰ composites.

3.8c Galvanostatic charge–discharge study: Figure 11 shows the galvanostatic charge/discharge curves of PANI, PANI/rGO and PANI/rGO/Fe⁰ at a constant current density of 1 A g⁻¹. The specific capacitance values of polymers and polymer nanocomposites electrodes from galvanostatic charge–discharge curves were calculated. The specific capacitance in PANI, PANI/rGO and PANI/rGO/Fe⁰ electrodes was observed as 182, 294 and 347 F g⁻¹, respectively. The ternary composites exhibit a nearly triangular shape in the charge–discharge curve and a longer discharge time compared to pure PANI and PANI/rGO composites at the same current density, implying the combined EDL and the pseudocapacitances of PANI and PANI/rGO, respectively.

The higher specific capacitance values of composite when compared to polymer and PANI/rGO under the same current density may be due to the oxidation–reduction reaction of polymer by highly conductive rGO/Fe⁰ sheets and also due to the π - π interaction between the rGO/Fe⁰ layer and polymer which may contribute to extend the conjugation length of the composite which allows the

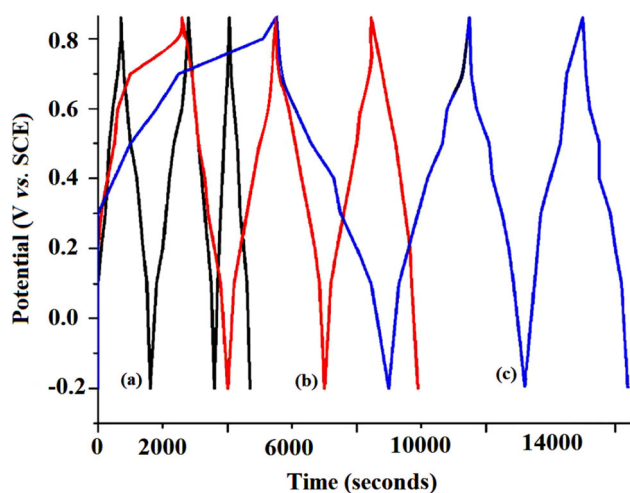


Figure 11. Galvanostatic charge/discharge curves of (a) PANI, (b) PANI/rGO and (c) PANI/rGO/Fe⁰ composites (current density 1 A g⁻¹).

counter ions to readily penetrate into the polymer matrix and access their internal surface.

The effect of current density on capacitance values of the prepared composite was also examined (figure 12). On increasing current density from 1 to 6 A g⁻¹, the capacitance behaviour of the ternary composite decreased from 347 to 289 F g⁻¹ (83.2% retention), whereas the PANI and PANI/rGO binary composites showed 64.6% (182 to 118 F g⁻¹) and 86.7% (294 to 255 F g⁻¹) capacitance retention, respectively. The enhanced capacitance of the ternary composite may be due to the large surface area of the rGO and Fe⁰ with high conductivity which may increase the charge-transport behaviour and favours ionic movements during discharging [34].

The cycling stability during long-term charging/discharging cycle with a scan rate of 50 mV s⁻¹ was studied (figure 13). Here, only 4.6% loss in the capacitance (from 347 to 331 F g⁻¹) during 500 charge/discharge cycles at 1 A g⁻¹ current density was found to be in PANI/rGO/Fe⁰ ternary composite, whereas PANI/rGO loses 19.4% of its capacitance (from 294 to 237 F g⁻¹) and the pure PANI loses 31.4% in the capacitance (from 182 to 155 F g⁻¹) at the same conditions. The rGO and Fe⁰ may restrict the shrinking and swelling of polymer during charge/discharge

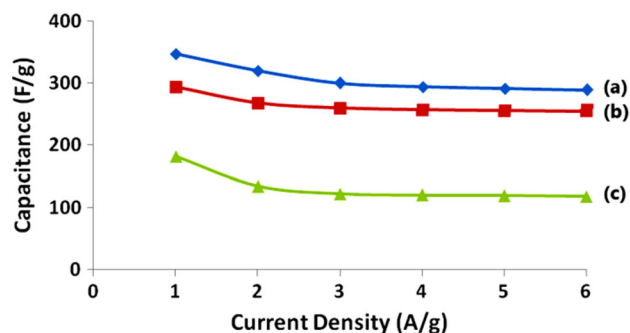


Figure 12. Specific capacitances of (a) PANI/rGO/Fe⁰, (b) PANI/rGO and (c) PANI at different discharging current densities.

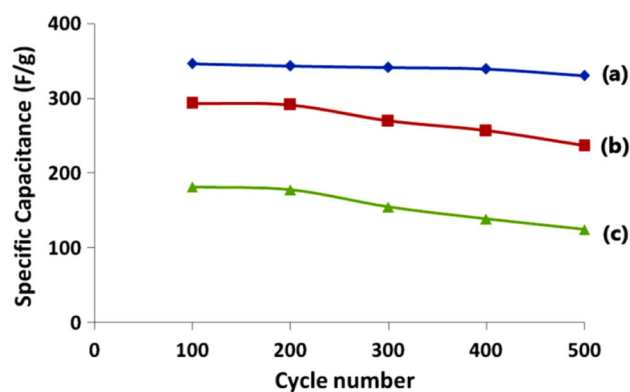


Figure 13. Cycling stability of (a) PANI/rGO/Fe⁰, (b) PANI/rGO and (c) PANI up to 500 charge/discharge cycles (current density, 1 A g⁻¹).

cycling which result in the better electrochemical stability of the composite than that of the pristine polymer.

4. Conclusion

The PANI/rGO/Fe⁰ composites have been successfully synthesized via interfacial polymerization through reductive deposition of rGO and Fe⁰ onto the PANI and were found to be promising candidates for capacitor electrode. The FTIR and XRD reveal the interaction between rGO, Fe⁰ and PANI. Charge–discharge measurements, EIS and CV were performed to characterize these materials as supercapacitor electrodes and the resulting data shows pronounced electrochemical activity, i.e., high conductivities, good reversibility and low current densities compared to pure PANI and binary PANI/rGO composites. This may be due to the large surface area of rGO sheets and Fe⁰ nanoparticle that exists within the polymer matrix. High specific capacitances are achieved for PANI/rGO/Fe⁰ composite (342 F g⁻¹) when compared with PANI (182 F g⁻¹) and PANI/rGO composites (294 F g⁻¹) at a constant current density of 1.0 A g⁻¹. Furthermore, the ternary composite showed better electrochemical stability after 500 charging/discharging cycles (95.4% capacitance retained) than that of the binary PANI/rGO composite (80.6% capacitance retained) and pure PANI (68.6% capacitance retained).

Considering their improved conductivity, capacitance behaviour and cyclic self-stability, the PANI/rGO/Fe⁰ ternary composite can provide new prospects in the field energy storage application and supercapacitor application.

Acknowledgements

SB and SK both acknowledge Science and Engineering Research Board (SERB), India, for providing research

Grant (Nos. SR/WOS-A/CS-161/2016, SERB/F/6115/2013-14) and (No. SB/FT/CS-025/2013), respectively.

References

- [1] Wang H, Hao Q, Yang X, Lu L and Wang X 2010 *ACS Appl. Mater. Interfaces* **2** 821
- [2] Pandolfo A G and Hollenkamp A F 2006 *J. Power Sources* **157** 11
- [3] Heydari H and Gholivand M B 2016 *J. Mater. Sci.: Mater. Electron.* **28** 3607
- [4] Kaya A, Alialy S, Demirezen S, Balbas M, Kin S Y and Aytumur A 2016 *Ceram. Int.* **42** 3322
- [5] Parlaktu F, Altundal S, Tatarog A, Parlak M and Agasiev A 2008 *Microelectron. Eng.* **85** 81
- [6] Yu Z, Tetard L, Zhai L and Thomas J 2015 *Energy Environ. Sci.* **8** 702
- [7] Yu D and Liming D L 2010 *J. Phys. Chem. Lett.* **1** 467
- [8] Zhou X, Huang X, Qi X, Wu S, Xue C, Boey F Y *et al* 2009 *J. Phys. Chem. C* **113** 10842
- [9] Liu K, Chen L, Chen Y, Wu J, Zhang W, Chen F *et al* 2011 *J. Mater. Chem.* **21** 8612
- [10] Li X, Zhang H, Wanga G and Jiang Z 2020 *J. Mater. Chem.* **10** 10598
- [11] Gu Z, Zhang L and Li C 2009 *J. Macromol. Sci. Part B: Phys.* **48** 1093
- [12] Gu Z, Li C, Wang G, Zhang L, Li X, Wang W *et al* 2010 *J. Polym. Sci. Part B: Polym. Phys.* **48** 1329
- [13] Bora C, Sarkar C, Mohan K J and Dolui S K 2015 *Electrochim. Acta* **157** 225
- [14] Pethe S M and Kondawar S B 2014 *Adv. Mater. Lett.* **5** 728
- [15] Gui D, Liu C, Chen F and Liu J 2014 *Appl. Surf. Sci.* **307** 172
- [16] Ren L M, Dong J, Chi Z and Huang H 2018 *J. Environ. Sci.* **73** 96
- [17] Hwang J H, Pathak P, Wang X, Rodriguez K L, Park J J, Chob H J *et al* 2019 *Sens. Actuators B Chem.* **294** 89
- [18] Yanilmaz M, Dirican M, Asiric A M and Zhang X 2019 *J. Energy Storage* **24** 100766
- [19] Yesuraj J, Padmaraj O and Suthanthiraraj S A 2020 *J. Inorg. Organomet. Polym. Mater.* **30** 310
- [20] Suneetha R B, Selvi P and Vedhi C 2019 *Vacuum* **164** 396
- [21] Zhou J, Zhang C, Niu T, Huang R, Li S, Zhang J Z *et al* 2018 *ACS Appl. Energy Mater.* **1** 4599
- [22] Bora C and Dolui S K 2012 *Polymer* **53** 923
- [23] Bora C and Dolui S K 2014 *J. Phys. Chem. C* **118** 29688
- [24] Schedin F, Geim A K, Morozov S V, Hill E W, Blake P, Katsnelson M I *et al* 2007 *Nat. Mater.* **6** 652
- [25] Wu J, Pisula W and Mullen K 2007 *Chem. Rev.* **107** 718
- [26] Bunch J S, van der Zande A M, Verbridge S S, Frank I W, Tanenbaum D M, Parpia J M *et al* 2007 *Science* **315** 490
- [27] Liu N, Luo F, Wu H, Liu Y, Zhang C and Chen J 2008 *Adv. Func. Mater.* **18** 1518
- [28] Konwer S, Begum A, Bordoloi S and Borua R 2017 *J. Polym. Res.* **24** 371
- [29] Konwer S, Boruah R and Dolui S K 2011 *J. Electron. Mater.* **40** 2248
- [30] Liu P G, Gong K C, Xiao P and Xiao M 2000 *J. Mater. Chem.* **10** 933

- [31] Konwer S 2016 *J. Mater. Sci.: Mater. Electron.* **27** 4139
- [32] Rose A, Prasad K G, Sakthivel T, Gunasekaran V, Maiyalagan T and Vijayakumar T 2018 *Appl. Surf. Sci.* **449** 551
- [33] Sultana S, Bordoloi S, Konwer S, Borah G and Gogoi P K 2020 *Appl. Organomet. Chem.* **34** e5582
- [34] Chetia M, Konwar M, Pegu B, Konwer S and Sarma D 2021 *J. Mol. Struct.* **1233** 130019
- [35] Xu Y, Schwab M G, Strudwick A J, Hennig I, Feng X, Wu Z *et al* 2013 *Adv. Energy Mater.* **3** 1035
- [36] Zhang T, Yue H, Gao X, Yao F, Chen H, Lu X *et al* 2020 *Dalton Trans.* **49** 3304
- [37] Ahmad A, Qureshi A S, Li L, Bao J, Xia X, Xu Y *et al* 2016 *Colloids Surf. B: Biointerfaces* **143** 490
- [38] Hlekelele L, Nomadolo N E, Setshedi K Z, Mofokeng L E, Chetty A and Chauke V P 2019 *RSC Adv.* **9** 14531
- [39] Liu A, Li C, Bai H and Shi G 2010 *J. Phys. Chem. C* **114** 22783
- [40] Wang S, Gao B, Li Y, Elise A C and He F 2017 *J. Hazard. Mater.* **322** 172
- [41] Heydari H and Gholivand M B 2017 *J. Mater. Sci.: Mater. Electron.* **28** 3607
- [42] Arjomandi J, Lee J Y, Ahmadi F, Parvin M H and Moghanni-Bavil-Olyaei H 2017 *Electrochim. Acta* **252** 212



Removal of As(III) and As(V) from water using reduced GO-Fe⁰ filled PANI composite

Shreemoyee Bordoloi, Rupkamal Chetia, Geetika Borah & Surajit Konwer

To cite this article: Shreemoyee Bordoloi, Rupkamal Chetia, Geetika Borah & Surajit Konwer (2021): Removal of As(III) and As(V) from water using reduced GO-Fe⁰ filled PANI composite, Journal of Applied Water Engineering and Research, DOI: [10.1080/23249676.2021.1948361](https://doi.org/10.1080/23249676.2021.1948361)

To link to this article: <https://doi.org/10.1080/23249676.2021.1948361>



Published online: 23 Jul 2021.



Submit your article to this journal [↗](#)



Article views: 3



View related articles [↗](#)



View Crossmark data [↗](#)

Removal of As(III) and As(V) from water using reduced GO-Fe⁰ filled PANI composite

Shreemoyee Bordoloi^{a,b}, Rupkamal Chetia^a, Geetika Borah^a and Surajit Konwer^{a*}

^aDepartment of Chemistry, Dibrugarh University, Dibrugarh, India; ^bDepartment of Chemistry, MDKG College, Dibrugarh, India

(Received 7 December 2020; accepted 21 June 2021)

A novel ternary adsorbent was prepared by reductive deposition of zerovalent iron on reduced graphene oxide through in-situ polymerization of aniline. SEM/EDS study showed an irregular, porous, and heterogeneous surface morphology with iron available for As binding. Batch adsorption experiments were conducted to determine the optimum conditions for As adsorption with optimum adsorbent dose, initial concentration of As, pH etc. Under optimized conditions, the maximum removal percentage of As was 99.6% for As(III) and 89% for As(V). The adsorption of arsenic on the composite was fitted well to the pseudo-second-order kinetic model and obeyed both Langmuir [$R^2 = 0.955$ for As(III) and 0.992 for As(V)] and Freundlich [$R^2 = 0.975$ for As(III) and 0.993 for As(V)] models. In aqueous solutions, the common co-ions phosphate hindered As removal more than the any other ions. The absorptive ability of adsorbent was compared with those of different adsorbents and found to be considerably efficient.

Keywords: Arsenic removal; graphene oxide; polyaniline; adsorbent; water treatment; Zero-valent iron

1. Introduction

Contamination of water from carcinogenic metalloid arsenic is creating a menace worldwide as a long time exposure to arsenic through drinking water can cause severe health problems (Thomas et al. 2007; Chakraborti et al. 2010). Chronic exposure to arsenic-contaminated drinking water is the major cause of arsenic poisoning in developing countries, such as, India (Chakraborti et al. 2002), Bangladesh (Roberts et al. 2011), China (Xie et al. 2009), Vietnam (Kim et al. 2009), where millions of people are using arsenic-contaminated groundwater with concentration above WHO guideline of $10 \mu\text{g/L}$ for arsenic (WHO, Environmental Health Criteria 224 2001; Berg et al. 2006). Arsenic is released into water sources by natural processes, such as dissolution and weathering of arsenic minerals or by some anthropogenic activities such as mining, use of arsenical pesticides, herbicides, fertilizers in agriculture, industrial effluents, improper disposal of chemical waste etc. Arsenate, As(V) (H_3AsO_4 , H_2AsO_4^- , HAsO_4^{2-}) along with arsenite, As(III) (H_3AsO_3 , H_2AsO_3^- , HAsO_3^{2-}), is the primary inorganic form in groundwater (Nickson et al. 2000). Greater attention is required for the removal of As(III) from groundwater due to its higher toxicity and mobility than As(V).

During the past few decades, diverse conventional and modern approaches for removing arsenic and other contaminants have been explored and various techniques, such as adsorption, coagulation/filtration, ion-exchange,

reverse osmosis, photo-oxidation, nanofiltration, chemical precipitation and membrane technologies, have been proposed (USEPA 2000; Yoon et al. 2009; Maiti et al. 2013; Neumann et al. 2013; Bordoloi et al. 2013a, 2013b; Lingamdinne et al. 2018; Koduru et al. 2019; Sahu et al. 2019; Karri et al. 2020; Khan et al. 2021). However, there are various limitations for most of these techniques viz., high installation cost, required large tanks to obtain the effective ion etc. (Qiao et al. 2012). Among all these known methods, adsorption technique has been regarded as simple and effective due to its wide applicability, environment-friendliness and cost advantages. Various materials have been investigated for the removal of arsenic, which includes mixed aluminium/iron hydroxides, nanostructured iron/chromium oxides, iron-oxide-coated sand, ferrihydrite, granular iron, micro- and nanoparticles of various iron oxides etc. (Jain et al. 1999). Specifically tailored materials employed to enhance the arsenic removal efficiency, such as reduced graphene oxide, super magnetic iron oxide nanoparticles, graphene oxide/ferric hydroxide composites, graphene-based polymer composites, super magnetic high surface area Fe_3O_4 nanoparticles etc. (Chandra et al. 2010; Zhang et al. 2010a; Sreerasad et al. 2011; Tang et al. 2011). From most of the recent work, it has been found that sorbents, based on iron oxide, are heavily explored due to its high abundance, environmental-friendliness and cost advantages (Mohan and Pittman 2007; Lingamdinne et al. 2019a). As arsenic

*Corresponding author. Email: surajitkonwer@dibru.ac.in; geetikachem@yahoo.co.in

removal depends on the oxidation state of arsenic species in water and adsorption capacity of the adsorbent towards arsenic, it is very important to modify the size, structure and physicochemical textures of the sorbent to increase the removal efficiency.

Nanoscale zerovalent (NZVI) iron, an environmentally benign material, has showed great potential to remove arsenic from contaminated water due to its high surface reactivity and large active surface area (Wang et al. 2014). However, the use of NZVI in the remediation of contaminated water is limited due to its lack of stability, rapid aggregation and difficulty while separating from the treated solution. Hence, to overcome these problems, immobilization of NZVI onto supporting material, such as porous activated carbon, resin, clay, zeolite, etc., is reported (Jang et al. 2008; Shao et al. 2008). Immobilization of NZVI not only increases the stability of NZVI but also retains the properties of both support materials and NZVI. But, most of them were found to be effective only for moderate removal of arsenic. It is, therefore, necessary to explore new efficient support matrices for NZVI to obtain high removal capacity for arsenic (Wang et al. 2017).

Recently, reduced graphene oxide (rGO) has been positively tested as support matrix due to its exceptional electron transport, mechanical properties and high surface area (Konwer et al. 2013, 2017; Konwer 2016; Sultana et al. 2020). Moreover, the preparation of GO involves low cost as it can be readily made from low-cost natural graphite in a large scale. Various literatures showed that ferric hydroxide, iron oxide-loaded rGO, rGO-loaded Fe^0 showed the efficiency of arsenic adsorption (Zhang et al. 2010b; Lingamdinne et al. 2019b; Dehghani et al. 2020; Foti et al. 2020; Julian et al. 2020; Lingamdinne et al. 2020; Pradhan et al. 2020; Baskan and Hadimlioglu 2021; Raj et al. 2021).

Polyaniline (PANI) has stimulated research interest as it can be easily synthesized in bulk quantities and has a large surface area to volume ratio, with good redox properties, high conductivity and excellent environmental stability among the conducting polymers. This makes it improved for adsorption in separation and purification systems (Bhaumik et al. 2014). Moreover, to improve the physico-chemical properties of conducting polymer, metal nanoparticles were incorporated as secondary components (Li et al. 2013). The combination of metal particles and a conducting polymer strengthens the polymer and introduces electronic properties, based on the morphological modification or electronic interaction between the two components (Ren et al. 2010; Bhaumik et al. 2015; Vasaki et al. 2021).

In this study a novel adsorbent rGO- Fe^0 -PANI (reduced graphene oxide-zero valent iron-polyaniline) nanocomposite for arsenic removal was synthesized by a two-step method – chemical reduction of graphene oxide and ferric chloride to yield rGO/ Fe^0 binary composite, followed by in-situ polymerization of aniline on rGO/ Fe^0 surface.

In this study, the prepared composite was tested for its capacity to remove arsenate and arsenite from the aqueous solution along with batch experiment study to determine the optimum initial concentration of As (III) and As (V), adsorbent dose, and the effect of pH on the solution to achieve the best performance. To the best of authors' knowledge, no research results have been reported about arsenic adsorption by this effective ternary composite using reduced graphene oxide, zero valent iron and polyaniline.

2. Experimental

2.1. Materials

Sodium arsenate dibasic heptahydrate ($\text{Na}_2\text{HAsO}_4 \cdot 7\text{H}_2\text{O}$) and Sodium arsenite (NaAsO_2) are from Loba Chemi. Aniline was obtained from Aldrich Co. and used without further purification. The natural graphite flakes of size (crystalline, 300 mesh, Alfa Aesar) from Shanker Graphites and Chemical, New Delhi, India, sodium borohydride (NaBH_4), ferric chloride hexahydrate ($\text{FeCl}_3 \cdot 6\text{H}_2\text{O}$), hydrochloric acid (HCl), sulphuric acid (H_2SO_4), nitric acid (HNO_3), sodium nitrate (NaNO_3), potassium permanganate (KMnO_4), hydrogen peroxide (H_2O_2), and potassium persulphate ($\text{K}_2\text{S}_2\text{O}_8$) were of analytical reagent grade chemicals (Merck) and used as received. Acetonitrile was obtained from Merck and purified by standard methods. For all purposes double distilled water was used. An As(III) and As(V) stock solution (1000 mg/L) were prepared by dissolving NaAsO_2 and $\text{Na}_2\text{HAsO}_4 \cdot 7\text{H}_2\text{O}$ in distilled water.

2.2. Instrumentation

Arsenic [As (III) and As (V)] solution concentrations were determined by a PerkinElmer Atomic Absorption Spectrometer, model PinAAcle 900 H equipped with hydride generating system FIAS 100. pH value was measured using a Thermo Scientific Orion Star A111 pH Benchtop Metre. Scanning Electron Microscope (SEM) coupled with EDX (Jeol, Japan, JSM-6390LV) was used to study the surface morphology of adsorbents. FTIR (Impact 410, Nicolet, USA) spectra were used to characterize the adsorbents. TEM measurements were conducted by PHILIPS CM 200 microscope at 200 kV. Bruker AXS, Germany, D8 FOCUS using a scanning rate of $0.050^\circ/\text{s}$ in the range of $2\theta = (10 - 70)^\circ$ was used to study the X-ray diffraction. BET measurement was recorded using Quantachrome NOVAE 2200 apparatus using N_2 adsorption (77.35 K).

2.3. Preparation of PANI/rGO/ Fe^0 ternary nanocomposite

At first GO was synthesized from graphite powder using Hammer's method (Hummert and Offeman 1958) and it was exfoliated in water to produce a suspension of GO sheets. The mixed water solution of FeCl_3 was added

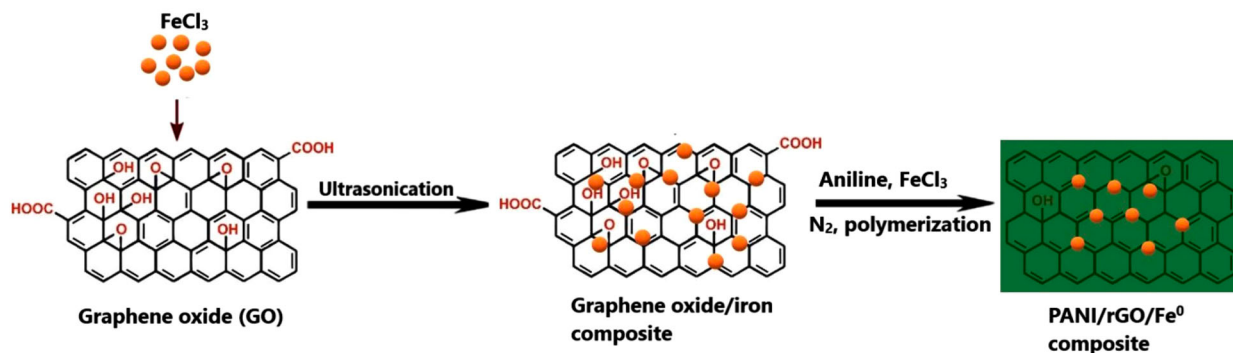
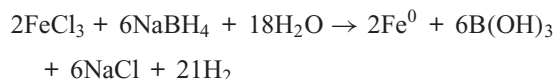


Figure 1. Schematic presentation of the preparation of PANI/rGO/Fe⁰.

slowly to the GO solution and ultrasonicated for 5 min. Then aniline was syringed at a time to the mixture and stirred vigorously under N₂ atmosphere for 2 h followed by the addition of NaBH₄ solution. The reduced products (PANI/rGO/Fe⁰) were collected by vacuum filtration and washed several times with water and ethanol. The final black powders were vacuum-dried at 60°C and stored in a N₂ purged desiccator (Figure 1).

In the preparation of PANI/rGO/Fe⁰, the liquid phase reduction of FeCl₃ and GO takes place using NaBH₄. The probable reaction mechanism is shown as follows:



3. Results and discussion

3.1. FTIR analysis

The FTIR spectrum of pure polymer and composite is shown in Figure 2. The absorption peak at 3430 cm⁻¹ is attributable to the N–H stretching vibrations of the leucoemeraldine component of the polymer sample. The weak peak at 2924 cm⁻¹ corresponds to aromatic sp² CH stretching. The C = C stretching deformation of the quinoid ring in the emeraldine salt and benzenoid rings in leucoemeraldine is depicted at 1631 and 1461 cm⁻¹, respectively. The peaks at 1283 and 1152 cm⁻¹ correspond to C–N stretching of the secondary aromatic amine and C = N stretching, respectively. The spectrum of the PANI/GO/Fe⁰ composite, the absorption peaks, is similar to PANI except the characteristic peak of C = O group at 1728 cm⁻¹ that was observed from composite. The absorption peaks at ~1640 and 1450 cm⁻¹ represent the quinoid and benzenoid structures, respectively of the PANI in unexposed composite (Trchová and Stejskal 2011; Ibrahim 2017). The presence of PANI characteristic vibrations suggests PANI can be successfully deposited on the GO/Fe⁰ surface.

3.2. X-ray diffraction analysis (XRD)

Figure 3 shows the XRD pattern of PANI, GO, and PANI/rGO/Fe⁰ composite. A characteristic broad peak

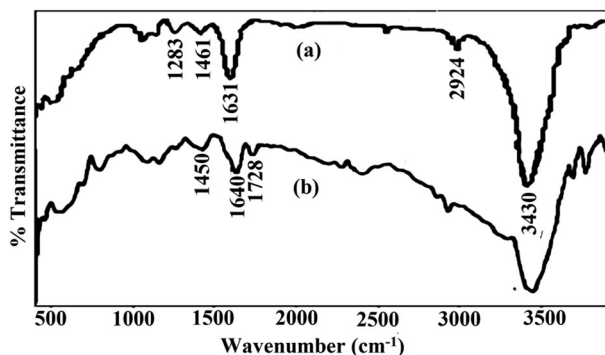


Figure 2. FTIR of (a) pristine PANI and (b) PANI/rGO/Fe⁰.

of amorphous PANI was observed at about $2\theta = 25.8^\circ$. The XRD pattern of rGO, a broad reflection with peak at $2\theta = 13.1^\circ$ corresponding to the (0 0 1) diffraction peak, indicates a typical loose layer-like structure. The corresponding peaks for the PANI/rGO/Fe⁰ composite at 26.9 and 55.2° match the (111) and (222) planes of rhombohedral system with rhomb-centred lattice [ref No. – PCPDFWIN 75-2078 and calculated from ICSD using POWD-12 + + (1997)]. The crystalline peaks are observed in the composite due to the dominant crystalline nature of GO and Fe⁰ particles.

3.3. SEM-EDS study

The surface morphology of pure graphite and rGO has been studied by scanning electron micrographs of their powdered sample (Figure 4). Due to rigorous oxidation of graphite planes, the opening of planar carbon networks wedged at the edge surface of crystallite, by surface group layer-like structures of rGO, is distinctly observed in the SEM micrograph. This is due to the opening of planar carbon networks wedged at the edge surface of crystallite by surface groups as a consequence of oxidation. Also rGO inherits the layer-by-layer and network structure but in a denser stacking compared with the randomly aggregate structure with a rough surface for the pure graphite.

SEM image (Figure 5) reveals that the adsorbent surface morphology is irregular, porous, and heterogeneous in

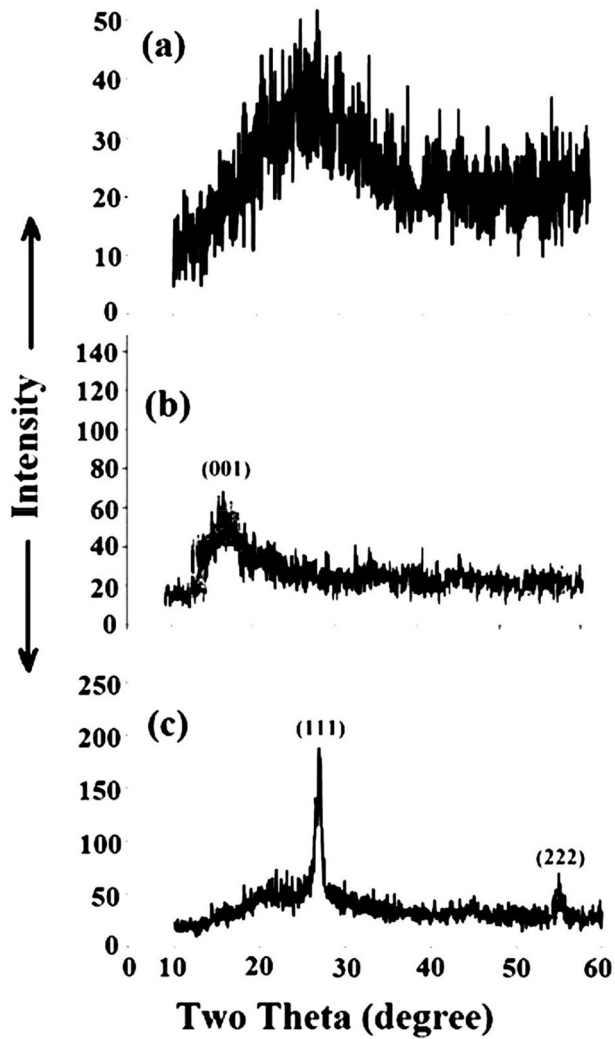


Figure 3. XRD analysis of (a) PANI, (b) rGO and (c) PANI/rGO/Fe⁰ composite.

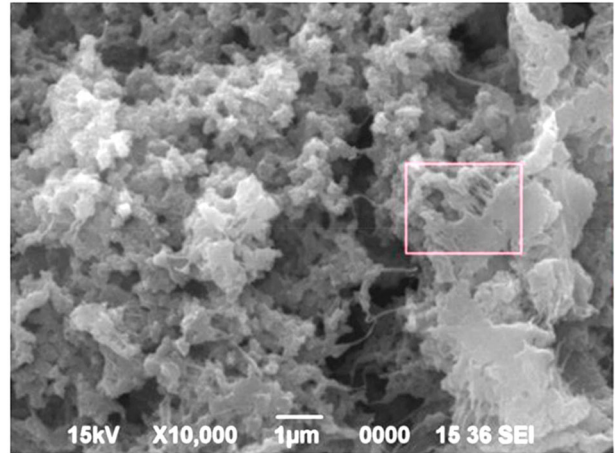


Figure 5. SEM of PANI/GO/Fe⁰ composite.

nature. In addition, pores and large cavities of the adsorbent may show their greater adsorption ability due to their extended surface area.

The elemental composition of the adsorbent's surface determined by EDS (Figure 6) shows the presence of Fe (with 3.06 estimated wt. %) in the composite.

3.4. TEM analysis

Typical morphology of rGO is shown in the TEM image of Figure 7. A layered structure of individual rGO sheets with a lateral dimension of few micrometres is observed in Supplementary Figure S5(a,b). On the other hand, some fibre-like structures of PANI, which are decorated at the surface of the rGO/Fe⁰ sheets, are observed in the TEM images of the composite [Supplementary Figure S5(c,d)]. It confirms the formation ordered PANI chain on the surface of the rGO/Fe⁰ sheets. In addition, it is observed that the PANI/rGO/Fe⁰ sheets are folded with dark edges which indicate the flexible character of the composite.

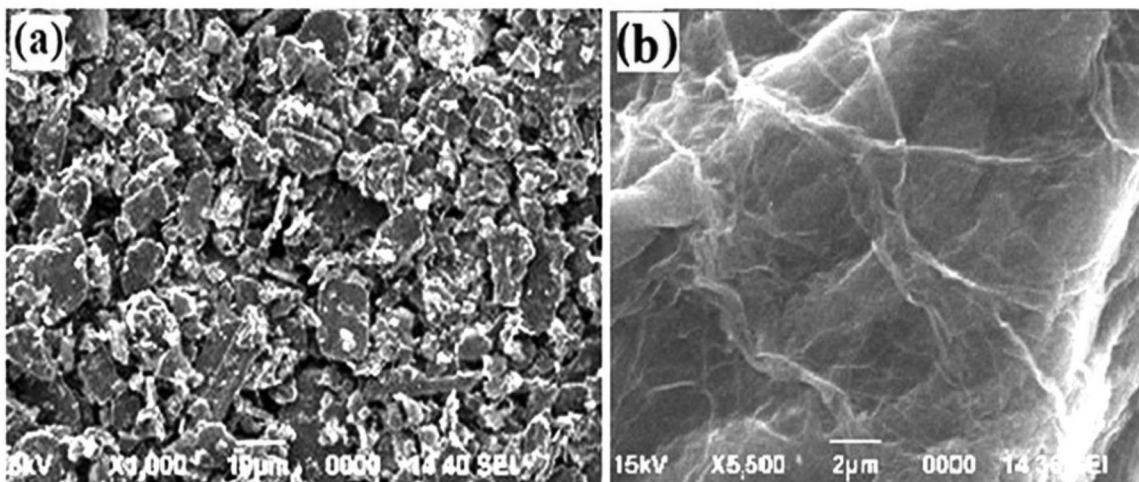


Figure 4. SEM images of (a) graphite and (b) rGO.

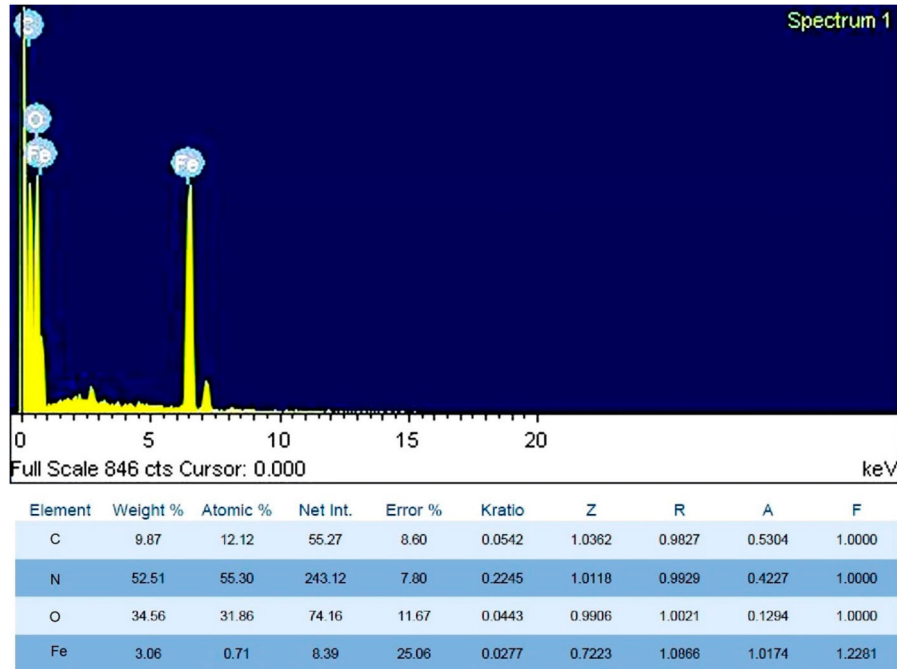


Figure 6. SEM of PANI/GO/Fe⁰ composite.

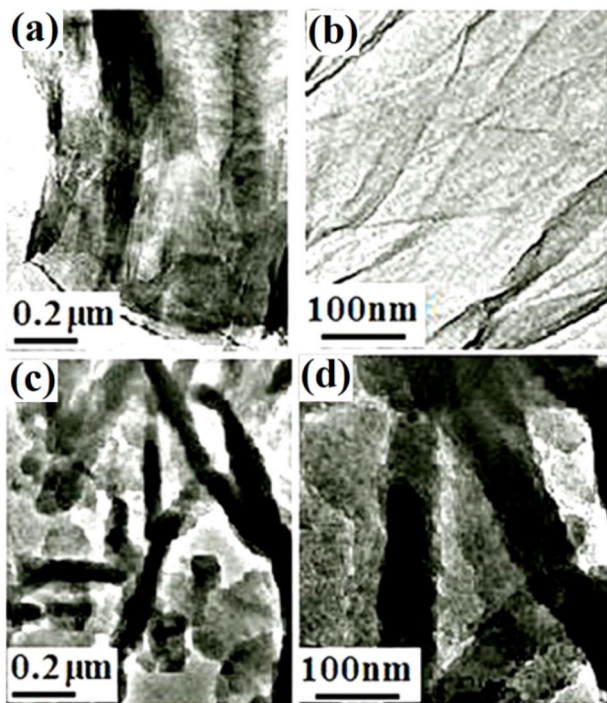


Figure 7. TEM images (a) GO at lower magnification; (b) GO at higher magnification, (c) PANI/rGO/Fe⁰ at lower magnification and (d) PANI/rGO/Fe⁰ at higher magnification.

3.5. Brunauer–Emmett–teller (BET) study

The BET results show that the specific surface area of PANI/GO/Fe⁰ is 14.01 m²g⁻¹ and the pore size is about 3.33 nm which is much higher than the surface area of

bare polymer (5.07 m²g⁻¹) but much lower than graphene (377.55 m²g⁻¹) which may be because the PANI wrapped on GO/Fe⁰ had caused the decrease of the specific surface area. The broad distributions of pore size for PANI and PANI/GO/Fe⁰ agree with the irregular morphology of PANI.

3.6. Effect of adsorbent dose on the removal of arsenic

To study the adsorptive performance of the new adsorbent, the amount of adsorbent dose was varied in between 0.1 and 1.0 g/L, with a fixed initial As(V) and As(III) concentration of 1 mg/L. Batch experiments were performed in 250 mL Erlenmeyer flasks, in which 0.01–0.1 g of composites were added into 100 mL of As(V) or As(III) solution. The above solutions were then shaken on a temperature-controlled water bath shaker at 200 rpm at 25°C and a contact time of 12 h. The removal % of As (adsorption efficiency) was determined using the following equation -

$$\% \text{removal} = (C_0 - C_e) / C_0 \times 100 \quad (1)$$

C_0 and C_e are the initial and equilibrium concentrations of As, in mg/L, respectively.

The sorption rate of both the arsenic species onto PANI/rGO/Fe⁰ was increased in adsorbent dose from 0.1 to 1 g/L (Figure 8), i.e. with the increase in adsorbent dose, active sites of the adsorbent increase which enhances As adsorption. The maximum adsorption capacities for As(V) and As(III) are up to 99.6% and 89%, respectively.

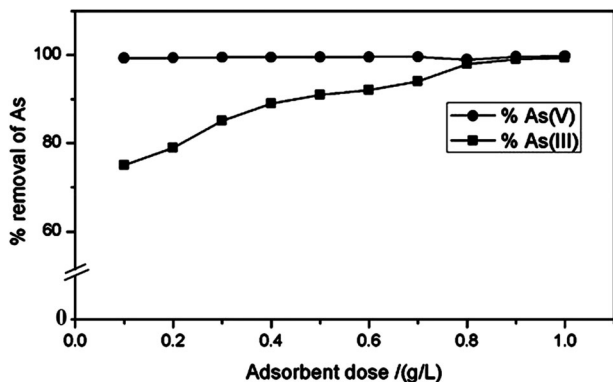


Figure 8. Plot of % of As(V) and As(III) vs. adsorbent dose in g/L.

3.7. Effect of the initial concentration of As

A batch experiment was carried out using a fixed dose of 0.5 g/L of adsorbent at different initial As(V) and As(III) concentrations of 0.5, 1.0, 3.0, 5.0, 7.0, 10.0, 15.0, 20.0 and 30.0 mg/L to observe the effect of initial As concentration (Figure 9) and with the increase in initial concentration, the removal of As gradually decreased.

Arsenic adsorption was reported to be more dependent on its oxidation states than the pH within a pH range of 5.5–7.5 (Smedley and Kinniburgh 2002). As(III) is relatively mobile than As(V) and Arsenic exists in near neutral reductive groundwater conditions mainly in the + III oxidation state as trihydrogen arsenite (H_3AsO_3) which is much less adsorbed than the + V species which exists predominantly as anionic dihydrogen arsenate (H_2AsO_5^-) ion (Wickramasinghe et al. 2004).

3.8. Effect of pH on adsorption of As

The effect of pH on As(V) and As(III) adsorption by PANI/rGO/ Fe^0 was examined by varying the solution pH from 3.0 to 10.0 (Figure 10). The pH of the solutions was adjusted using 0.1 M HCl or 0.1 M NaOH and the initial concentration of As(V) and As(III) was fixed at 1.0 mg/L.

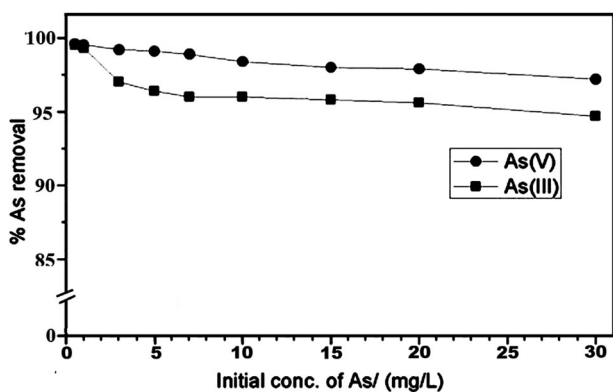


Figure 9. Plot of % removal of As(V) and As(III) against the initial As concentration in mg/L.

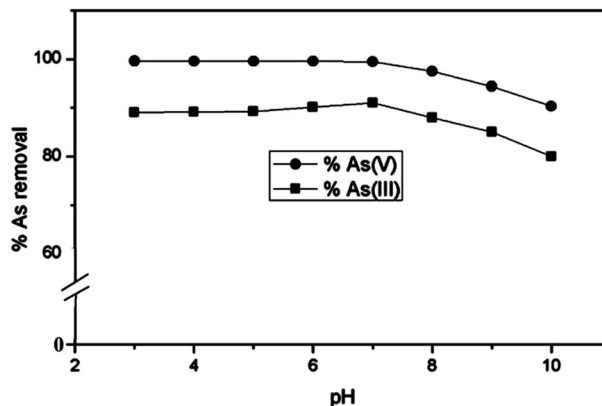


Figure 10. Effect of the initial solution pH on the removal of As(V) and As(III) using PANI/rGO/ Fe^0 (Initial [As(V)] and [As(III)] = 1 mg/L, adsorbent dose = 0.5 g/L).

The extent of As(V) removal was 99.6–90.3% in the pH range 3–10 and at neutral pH it was 99.48%, whereas for As(III) adsorption range was 91%–80% with maximum adsorption (91%) at neutral pH. It can be seen from the figure that PA/GO/ Fe^0 composite is effective for the removal of As(V) and As(III) in acidic and neutral range of pH. This can be explained as the ionization of both adsorbate and adsorbent in aqueous solution. In the acidic range of pH, H_2AsO_4^- and HAsO_4^{2-} are the predominant species of As(V), while below pH 9.2 H_3AsO_3 is the main species of As(III). Thus adsorption of anionic As(V) and As(III) was enhanced by columbic interaction, whereas at pH > 8, the negatively charged adsorbent species shows less affinity towards As(V) and As(III).

3.9. Kinetics of As adsorption onto PANI/GO/ Fe^0

The influence of adsorbent (PANI/GO/ Fe^0) dosage (0.1, 0.3, 0.5 g/L) at neutral pH on the rate of adsorption, using 1 mg/L of the initial concentration of As(V) and As(III) was investigated in the batch mode. From Figure 11, it can be seen that the sorption rate of both As species was increased with the increase in adsorbent dose due to the increase in active sites. The amount of As adsorbed was calculated by using the following equation:

$$q_t = (C_0 - C_t)V/m \quad (2)$$

where C_0 and C_t are the initial As concentration (mg/L) and As concentration (mg/L) at time 't', respectively; V is the volume of the solution (L); and m is the mass of the adsorbent taken (g).

The pseudo-first-order kinetics is described by the following equation:

$$\ln(q_e - q_t) = \ln q_e - k_1 t \quad (3)$$

where q_e and q_t are the As adsorption capacities of sorbent in (mg/g) at equilibrium and at time t, respectively, and k_1 is the pseudo-first-order rate constant in min^{-1} .

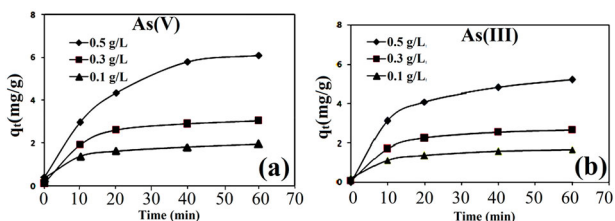


Figure 11. Effect of PANI/rGO/Fe⁰ dosage on the removal capacity with respect to time for (a) As(V) and (b) As(III).

The pseudo-second-order rate equation is expressed by the following equation:

$$t/q_t = (1/k_2)(1/q_e^2) + (t/q_e) \quad (4)$$

where q_e and q_t are the As adsorption capacities of sorbent at equilibrium and at time t , respectively, and k_2 is the pseudo-second-order rate constant in (g/mg/min).

Description of the kinetic data with appropriate kinetic model was expressed by correlation coefficient (R^2) and a relatively high R^2 value indicated that the model successfully described the kinetics of arsenic sorption by the composite. The parameters of pseudo-first-order and pseudo-second-order kinetic models are listed in Table 1 for As(V) and Table 2 for As(III), respectively. It was observed that the values of R^2 for pseudo-second order model are higher than those for the pseudo-first-order model. Finally, pseudo-second-order model has the best fit for adsorption kinetics of As. The plots of pseudo-first-order kinetic and pseudo-second-order kinetic models for both As species are presented in Figure 12(a–d) and the values of rate constants and q_e were calculated from the slope and the intercept of the plot of t/q_t vs. t , respectively.

3.10. Effect of coexisting anions

The effects of the competing anions, viz., sulphate, phosphate and silicate were studied in the concentration ranges 0–10 mM on the adsorption of 1 mg/L of As(V) and As(III) by 0.5 g/L PANI/GO/Fe⁰ and the results are presented in Table 3. The presence of the anions has been found to inhibit the arsenic removal, indicating that these ions compete for the surface adsorption sites of the adsorbent. With the increase in the concentrations of each of the competing ions, As removal percentage gradually decreases. Sulphate anion did not have significant effects on the As(V) and As(III) removal efficiencies, whereas silicate at higher concentration (10 mM) reduced the As(V) uptake from 99.5% to 93.2% and As(III) uptake from 91.3% to 84.2%. However, in the presence of phosphate at 10 mM, As(V) removal percentage decreases from 99.5% to 72.2% and As(III) decreases from 91.3% to 68.2%. The inhibitory effects of the competing ions on the arsenic removal increase in the order: sulphate < silicate < phosphate. These results are useful for in-situ remediation of As-contaminated groundwater due to the coexistence of competing anions in groundwater.

3.11. The Chemistry of As removal (XPS analysis)

To understand the chemistry involved behind arsenic removal, XPS analysis (Figure 13) of PANI/rGO/Fe⁰ was obtained before and after 24 h treatment with 100 mg/L As(III) and As(V) (as model arsenic species). In Figure 13(b,c), the third core level peak of arsenic is shown which confirms the presence of As species on the surface of the samples. The band energy value at 45.67 eV corresponds to the binding energy of As the third core level for As(V) species suggesting no reduction of As(V) species by the ternary composite. Since in aqueous solution, Fe⁰ reacts

Table 1. Kinetic parameters for As(V) adsorption by the PANI/rGO/Fe⁰.

Concentration arsenic (g/L)	Pseudo-first-order			Pseudo-second-order		
	K_1 (min ⁻¹)	q_e (mg/g)	R^2	K_2 (1/min)	q_e (mg/g)	R^2
0.1	0.156	10.365	0.984	0.118	8.321	0.992
0.3	0.147	7.321	0.984	0.103	5.735	0.990
0.5	0.112	3.216	0.980	0.098	4.147	0.965

Table 2. Kinetic parameters for As(III) adsorption by the PANI/rGO/Fe⁰.

Concentration arsenic (g/L)	Pseudo-first-order			Pseudo-second-order		
	K_1 (min ⁻¹)	q_e (mg/g)	R^2	K_2 (1/min)	q_e (mg/g)	R^2
0.1	0.097	7.899	0.916	0.021	12.672	0.986
0.3	0.168	6.215	0.942	0.036	9.924	0.990
0.5	0.521	3.042	0.969	0.541	4.119	0.990

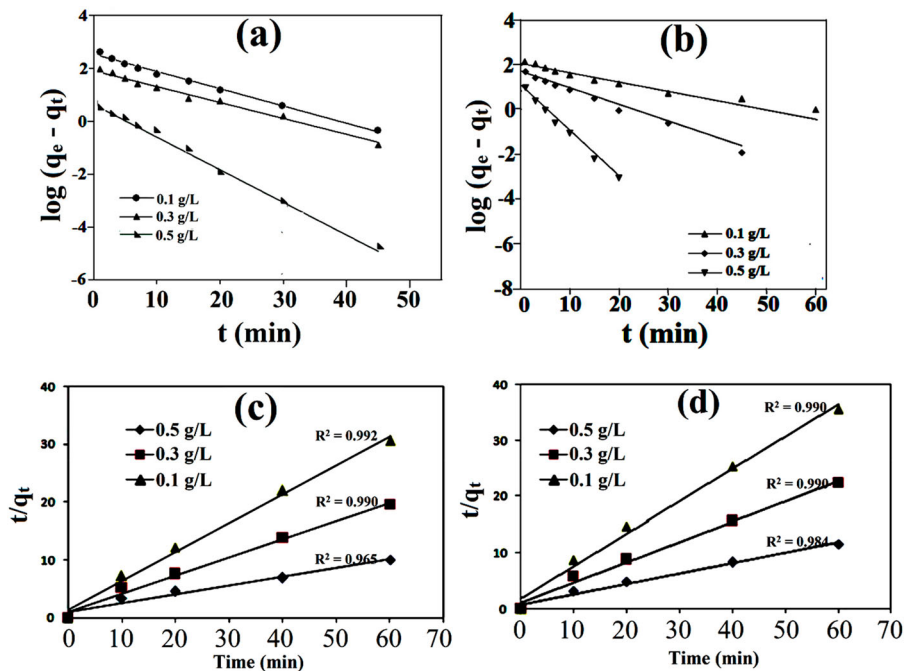


Figure 12. Fitting of kinetics data with pseudo-first-order model (a) As(V) and (b) As(III) and pseudo-second-order model for (c) As(V) and (d) As(III) removal using PANI/rGO/Fe⁰.

Table 3. As(V) and As(III) removal efficiencies of PANI/GO/Fe⁰ in the presence of coexisting anions.

As species	Concentration of anions (mM)	Removal of As in the presence of anion (%)		
		Sulphate	Silicate	Phosphate
As(III)	0	91.3	91.3	91.3
	0.1	91.1	90.9	87.5
	1	90.6	89.2	79.3
	10	87.4	84.2	68.2
As(V)	0	99.5	99.5	99.5
	0.1	99.4	99.2	94.4
	1	99.1	98.9	89.4
	10	94.5	93.2	72.2

with water and dissolved oxygen, there are possibilities of production of iron oxide (viz., ferrous hydroxide, ferric hydroxide, oxyhydroxides, lepidocrocite, maghemite and magnetite) depending on the redox and pH of the aqueous solution (Lingamdinne et al. 2019a). The core level peaks of Fe_{2p} centred at 711, 722 and 725 eV (Figure 13(a)) correspond to the binding energies of 2p_{3/2} and 2p_{1/2} of oxidized iron i.e. [Fe(III)]. So, the adsorption of arsenic onto these composite occurs via substitution of surface bonded OH⁻ ligand by arsenate and forms monodentate-adsorbed arsenate which later transformed into bidentate complex by substituting another OH⁻ ligand.

3.12. Adsorption isotherms

Aqueous solutions of different initial As concentrations (from 3 to 7 mg/L) at neutral pH and room temperature

(25°C) were used for the adsorption study (Figures 14 and 15). The data of arsenic adsorption were fitted with Freundlich and Langmuir isotherm models. The Langmuir isotherm model is expressed as

$$q_e = \frac{abc_e}{1 + bc_e} \quad (5)$$

The Freundlich isotherm is represented by the following equation:

$$q_e = K_f C_e^{1/n} \quad (6)$$

where q_e is the amount of arsenic adsorbed per unit weight of adsorbent (mg/g), C_e is the equilibrium concentration of arsenic (mg/L), b is the constant related to the free energy of adsorption (L/mg), and a is the maximum adsorption capacity (mg/g), K_f and $1/n$ are Freundlich constants related to the adsorption capacity (mg/g) and intensity of adsorption, respectively.

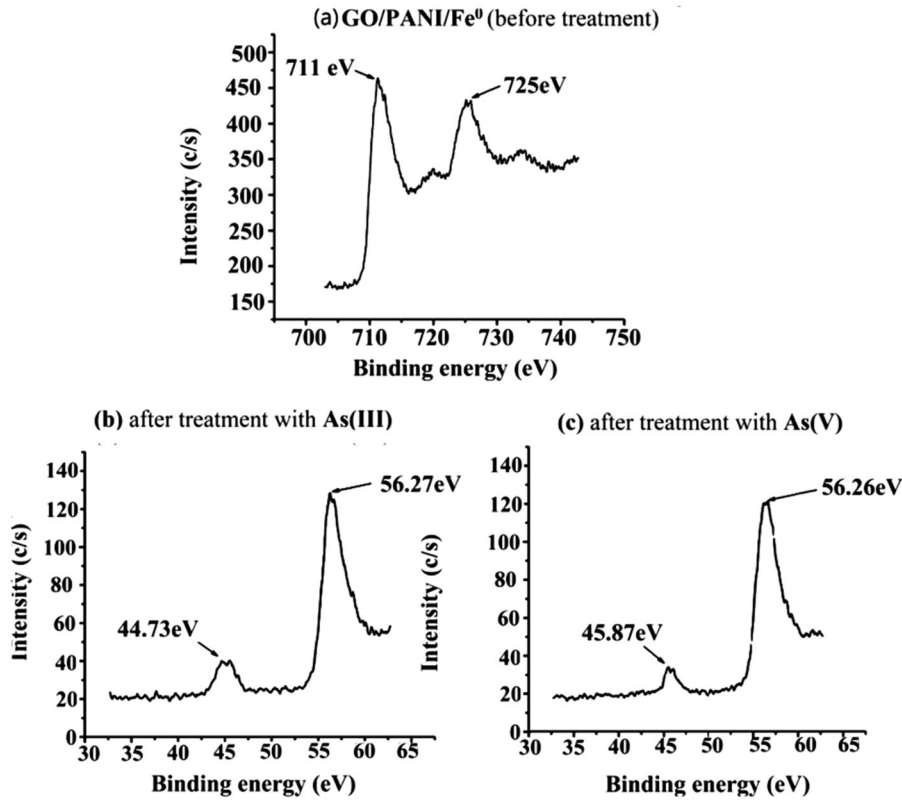


Figure 13. (a) XPS spectra of the PANI/GO/Fe⁰ before treatment with As. (b) As the third core-level spectrum after treatment with As(III). (c) As the third core-level spectrum after treatment with As(V).

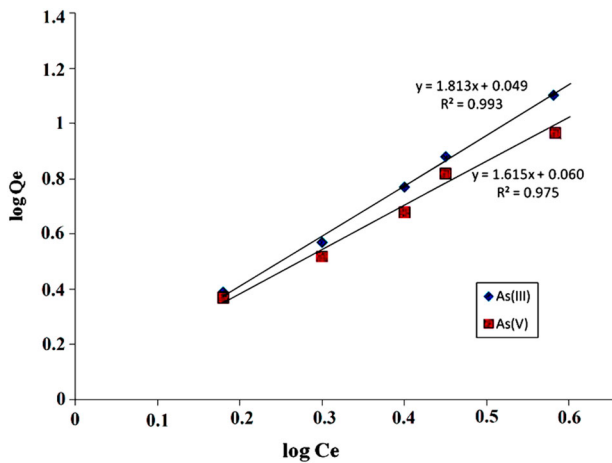


Figure 14. Langmuir isotherm for As(III) and As(V) ion at 30°C.

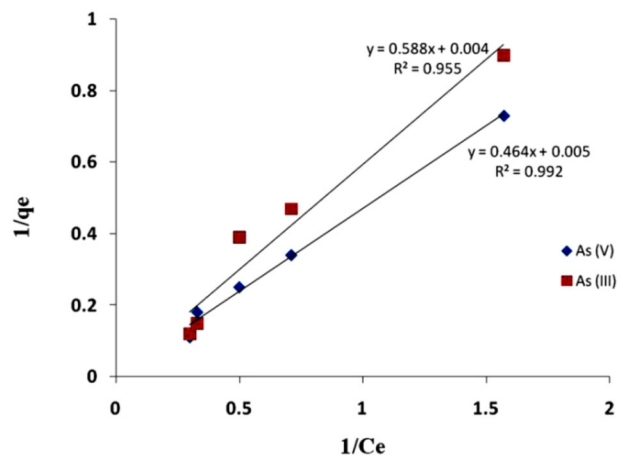


Figure 15. Freundlich isotherm for As(III) and As(V) ion at 30°C.

To study Langmuir and Freundlich isotherms, graph between 1/q_e and 1/C_e and log q_e vs log C_e was plotted, respectively and the adsorption data fitted well with both isotherms. The maximum adsorption amounts of As(V) and As(III) over PANI/rGO/Fe⁰ calculated by Langmuir model for As(III) and As(V) are 250 and 200 mg/g, respectively at neutral pH. The adsorption constants evaluated from the isotherms are listed in Table 4. Value of n is more than 0.5 which shows better adsorption behaviour

than normal adsorption and K_f was 1.119 for As(III) and 1.148 for As(V).

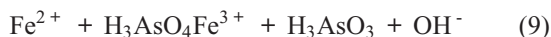
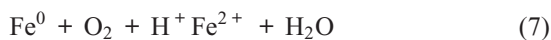
3.13. Comparison of maximum As adsorption capacities using different adsorbents

The maximum adsorption capacity calculated by Langmuir equation for the removal of As by various adsorbents is reported in the literature and summarized in Table 5. It is

Table 4. Langmuir and Freundlich Adsorption Isotherm Parameters for As(III) and As(V) on PANI/rGO/Fe⁰ composite.

Isotherm type	Isotherm constants	As(III)	As(V)
Langmuir	A	250.0	200.0
	B	0.147	0.051
	R ²	0.955	0.992
Freundlich	K _f	1.119	1.148
	N	0.55	0.61
	R ²	0.975	0.993

found that the adsorption capacity of the PANI/rGO/Fe⁰ is significantly higher than that of other adsorbents which may be due to the small size of Fe⁰ nanoparticles immobilized on the high surface area reduced graphene oxide and polymer matrix. The Fe⁰ nanoparticles were entrapped into PANI and rGO surfaces, which enhanced the stability of Fe⁰ particles and the oxygen-containing functional group provided more active sites to interact with arsenic species. The rGO not only contributes to the adsorption of arsenic, but also acts as a support for both iron nanoparticles and PANI. Fe⁰ spontaneously reacts with water and dissolved oxygen to produce Fe²⁺ and Fe³⁺, which further produces a series of different iron oxides. The probable structure of Fe⁰ and iron oxide present in the composite is expected as the core-shell structure where Fe⁰ forms core and its oxide forms shell. As(V) can be reduced to As(III) because of the role played by the reactive Fe(II) and PANI (since PANI also has redox behaviour).



4. Conclusion

Adsorption capacity and the efficiency of prepared rGO/Fe⁰ filled PANI ternary composite were studied for the removal of arsenic from aquatic solutions. The present study showed that the efficiency of the removal process depends on various factors, such as the initial concentration

of adsorbent, arsenic concentrations, coexisting anions and pH of the solution. The adsorption rate of As (both arsenate and arsenite) increases with the increase in adsorbent dose from 0.1 to 0.5 g/L and maximum adsorption capacities were up to 99.6% for As(III) and 89% for As(V). The maximum arsenic removal (99.48% for arsenate and 91% for arsenite) was obtained at the pH of 7 and both acidic and neutral range of pH (~3–10); it is effective for the removal of As(V) and As(III). Characteristics of the adsorbent viz., high surface area, the presence of suitable functional groups on the surface, and irregular heterogeneous surface morphology enhanced its adsorption potential significantly. The adsorption of arsenic on the adsorbent was fitted well to the pseudo-second-order kinetic model and obeyed both Langmuir and Freundlich models; this indicates surface heterogeneity and monolayer adsorption of the adsorbents. The presence of common co-ions (viz., sulphate, phosphate and silicate) inhibited the arsenic removal with the order: sulphate < silicate < phosphate. Because of the above-mentioned benefits of the PANI/rGO/Fe⁰ composite, such as high absorption capacity, effective removal efficiency, easy synthesis and availability, the use of this adsorbent can be considered for the removal of arsenic from the aqueous solution.

Disclosure statement

No potential conflict of interest was reported by the author(s).

Funding

The author S. Bordoloi thanks DST-SERB, India for the financial support of the research work under Women Scientist Scheme-A (WOS-A) provided by Science and Engineering Research Board (SERB), India [Grant Number SR/WOS-A/CS-161/2016]. The author S. Konwer thanks the DST-SERB, India, for their financial support in the research work under ‘‘Fast Track Scheme for Young Scientists provided by Department of Science and Technology (DST), India’’ [Grant Number SERB/F/6115/2013-14]. Science and Engineering Research Board (SERB), India.

Notes on contributors

Dr. Shreemoyee Bordoloi did her MSc from Department of Chemistry, Dibrugarh University and PhD from Department of

Table 5. Comparison of maximum As adsorption capacities using different adsorbents.

Adsorbent	Max. As(III) adsorption (mg/g)	Max. As(V) adsorption (mg/g)	Ref.
NZVI	3.5	—	
NZVI/AC	18.2	12.0	Zhu et al. (2009)
NZVI-RGO	35.8, 45.57	29.0, 45.12	Wang et al. (2014); Liu et al. (2019)
Fe ₃ O ₄ nanoparticle	16.5, —	46.0, 58.38	Feng et al. (2012); Liu et al. (2018)
Fe–Cu binary oxide	122.3	82.7	Zhang et al. (2013)
Fe ₃ O ₄ –RGO nanoparticles	—, 104	58.48, 68	Hoan et al. (2016); Kanga et al. (2017)
Fe ₃ O ₄ –RGO–MnO ₂ nanoparticles	14.04	12.22	Luo et al. (2012)
PANI/iron	232.5, 28.27	227.2, 83.08	Li et al. (2013); Dutta et al. (2020)
PANI/rGO/Fe ⁰	250.0	200.0	Present study

Chemical Sciences, Tezpur University, Assam, India. Her areas of research interest are Water Purification, Material Chemistry. Presently she is working as an Assistant Professor in Department of Chemistry, MDKG College, Assam, India.

Mr. Rupkamal Chetia did his MSc from Dibrugarh University, and presently pursuing PhD from Department of Chemistry, Dibrugarh University, Assam India.

Dr. (Ms) Geetika Borah did her MSc and PhD from Department of Chemistry, Dibrugarh University, India. Her areas of research interest are Co-ordination Chemistry, Catalysis, Nanochemistry. Presently she is working as a Professor in Department of Chemistry, Dibrugarh University, Assam, India.

Dr. Surajit Konwer did his MSc from Gauhati University and PhD from Department of Chemical Sciences, Tezpur University, Assam, India. His research areas of interest are Multifaceted Polymeric Nanocomposites, Graphene Science, Nanochemistry and Water Treatment. Presently he is working as an Assistant Professor in Department of Chemistry, Dibrugarh University, Assam, India.

References

- Baskan BM, Hadimlioglu S. 2021. Graphene oxide-iron modified clinoptilolite based composites for adsorption of arsenate and optimization using response surface methodology. *J Environ Sci Health, Part A*. 56: 537–548.
- Berg M, Luzi S, Kim PT, Hung TP, Walter VG, Stüben D. 2006. Arsenic removal from groundwater by household sand filters: comparative field study, model calculations, and health benefits. *Environ Sci Technol*. 40:5567–5573.
- Bhaumik M, Choi HJ, McCrindle RI, Maity A. 2014. Composite nanofibers prepared from metallic iron nanoparticles and polyaniline: high performance for water treatment applications. *J Colloid Interface Sci*. 425:75–82.
- Bhaumik M, Noubactep C, Gupta VK, McCrindle RI, Maity A. 2015. Polyaniline/Fe⁰ composite nanofibers: an excellent adsorbent for the removal of arsenic from aqueous solutions. *Chem Eng J*. 271:135–146.
- Bordoloi S, Nath M, Dutta RK. 2013a. pH-conditioning for simultaneous removal of arsenic and iron ions from groundwater. *Proc Saf Environ Prot*. 91:405–414.
- Bordoloi S, Nath SK, Gogoi S, Dutta RK. 2013b. Arsenic and iron removal from groundwater by oxidation-coagulation at optimized pH: laboratory and field studies. *J Hazard Mater*. 260:618–626.
- Chakraborti D, Rahman MM, Das B, Murrill M, Dey S, Chandra Mukherjee S, Dhar RK, Biswas BK, Chowdhury UK, Roy S, et al. 2010. Quamruzzaman Q. status of groundwater arsenic contamination in Bangladesh: a 14-year study report. *Water Res*. 44:5789–5802.
- Chakraborti D, Rahman MM, Paul K, Chowdhury UK, Sengupta MK, Lodh D, Chanda CR, Saha KC, Mukherjee SC. 2002. Arsenic calamity in the Indian subcontinent: what lessons have been learned? *Talanta*. 58:3–22.
- Chandra V, Park J, Chun Y, Lee JW, Hwang IC, Kim KS. 2010. Water-dispersible magnetite-reduced graphene oxide composites for arsenic removal. *ACS Nano*. 4:3979–3986.
- Dehghani MH, Karri RR, Alimohammadi M, Nazmara S, Zarei A, Saeedi Z. 2020. Insights into endocrine-disrupting bisphenol-A adsorption from pharmaceutical effluent by chitosan immobilized nanoscale zero-valent iron nanoparticles. *J Mol Liq*. 311:113317.
- Dutta S, Manna K, Srivastava SK, Gupta AK, Yadav MK. 2020. Hollow polyaniline microsphere/Fe₃O₄ nanocomposite as an effective adsorbent for removal of arsenic from water. *Sci Rep*. 10:4982.
- Feng L, Cao M, Ma X, Zhu Y, Hu C. 2012. Superparamagnetic high-surface-area Fe₃O₄ nanoparticles as adsorbents for arsenic removal. *J Hazard Mater*. 439–446:217–218.
- Foti C, Mineo GP, Nicosia A, Scala A, Neri G, Piperno A. 2020. Recent advances of graphene-based strategies for arsenic remediation. *Front Chem*. 8:608236.
- Hoan NTV, Thu NTA, Duc HV, Cuong ND, Khieu DQ, Vo V. 2016. Fe₃O₄/reduced graphene oxide nanocomposite: synthesis and Its application for toxic metal Ion removal. *J Chem*. 2016:1–10.
- Hummers WS, Offeman RE. 1958. Preparation of graphitic oxide. *J Am Chem Soc*. 80:1339–1339.
- Ibrahim KA. 2017. Synthesis and characterization of polyaniline and poly(aniline-co-o-nitroaniline) using vibrational spectroscopy. *Arab J Chem*. 10:S2668–S2674.
- Jain A, Raven KP, Loeppert RH. 1999. Arsenite and arsenate adsorption on ferrihydrite: surface charge reduction and net OH⁻ release stoichiometry. *Environ Sci Technol*. 33:1177–1184.
- Jang M, Chen WF, Cannon FS. 2008. Preloading hydrous ferric oxide into granular activated carbon for arsenic removal. *Environ Sci Technol*. 42:3369–3374.
- Julian AB, Fathi SA, Sherif M, El-Shall MS. 2020. Laser synthesis of magnetite-partially reduced graphene oxide nanocomposites for arsenate removal from water. *J Mater Sci*. 55:5351–5363.
- Kanga BK, Lim BS, Yoon Y, Kwag SH, Park WK, Song YH, Yang WSe, Ahn Y-T, Kang J-W, Yoon DH. 2017. Efficient removal of arsenic by strategically designed and layer-by-layer assembled PS@rGO@GO@Fe₃O₄ composites. *J Env Manag*. 201:286–293.
- Karri RR, Sahub JN, Meikap BC. 2020. Improving efficacy of Cr (VI) adsorption process on sustainable adsorbent derived from waste biomass (sugarcane bagasse) with help of ant colony optimization. *Ind Crops Prod*. 143:111927.
- Khan FSA, Mubarak NM, Tan YH, Khalid M, Karri RR, Walvekar R. 2021. A comprehensive review on magnetic carbon nanotubes and carbon nanotube-based buckypaper-heavy metal and dyes removal. *J Hazard Mater*. 125375.
- Kim M, Um HJ, Bang S, Lee SH, Oh SJ, Han JH, Kim KW, Min J, Kim YH. 2009. Arsenic removal from Vietnamese groundwater using the arsenic-binding DNA aptamer. *Environ Sci Technol*. 43:9335–9340.
- Koduru JR, Karri RR, Mubarak NM. 2019. Smart materials, magnetic graphene oxide-based nanocomposites for sustainable water purification. *Sustain Polym Compos Nanocomposites*. 1:759–778.
- Konwer S. 2016. Graphene oxide-polyaniline nanocomposites for high performance supercapacitor and their optical, electrical and electrochemical properties. *J Mater Sci Mater Electron*. 27:4139–4146.
- Konwer S, Begum A, Bordoloi S, Borua R. 2017. Expanded graphene-oxide encapsulated polyaniline composites as sensing material for volatile organic compounds. *J Polym Res*. 24:37–41.
- Konwer S, Guha AK, Dolui SK. 2013. Graphene oxide filled polyaniline composites as methanol sensing materials. *J Mater Sci*. 48:1729–1739.
- Li R, Liu L, Yang F. 2013. Preparation of polyaniline/reduced graphene oxide nanocomposites and its application in adsorption of aqueous Hg(II). *Chem Eng J*. 229:460–468.

- Lingamdinne LP, Choi JS, Choi YL, Chang YY, Yang JK, Karri RR. 2020. Process modeling and optimization of an iron oxide immobilized graphene oxide gadolinium nanocomposite for arsenic adsorption. *J Mol Liq.* 299:112261.
- Lingamdinne LP, Koduru JR, Chang YY, Karri RR. 2018. Process optimization and adsorption modeling of Pb (II) on nickel ferrite-reduced graphene oxide nano-composite. *J Mol Liq.* 250:202–211.
- Lingamdinne LP, Koduru JR, Karri RR. 2019a. A comprehensive review of applications of magnetic graphene oxide based nanocomposites for sustainable water purification. *J Environ Manag.* 231:622–634.
- Lingamdinne LP, Koduru JR, Karri RR. 2019b. Green synthesis of iron oxide nanoparticles for lead removal from aqueous solutions. *Key Eng Mater.* 805:122–127.
- Liu J, Kong L, Huang X, Liu M, Li L. 2018. Removal of arsenic(v) from aqueous solutions using sulfur-doped Fe₃O₄ nanoparticles. *RSC Adv.* 8:40804–40812.
- Liu P, Liang Q, Luo H, Fang W, Geng J. 2019. Synthesis of nano-scale zero-valent iron-reduced graphene oxide-silica nano-composites for the efficient removal of arsenic from aqueous solutions. *Environ Sci Pollut Res Int.* 26:33507–33516.
- Luo X, Wang C, Luo S, Dong R. 2012. Adsorption of As (III) and As (V) from water using magnetite Fe₃O₄-reduced graphite oxide–MnO₂ nanocomposites. *Chem Eng J.* 187:45–52.
- Maiti A, Thakur BK, Basu JK, De S. 2013. Comparison of treated laterite as arsenic adsorbent from different locations and performance of best filter under field conditions. *J Hazard Mater.* 262:1176–1186.
- Mohan D, Pittman JCU. 2007. Arsenic removal from water/waste water using adsorbents – a critical review. *J Hazard Mater.* 142:1–53.
- Neumann A, Kaegi R, Voegelin A, Hussam A, Munir AK, Hug SJ. 2013. Arsenic removal with composite iron matrix filters in Bangladesh: a field and laboratory study. *Environ Sci Technol.* 47:4544–4554.
- Nickson RT, McArthur JM, Ravenscroft P, Ahmed KM. 2000. Mechanism of arsenic release to groundwater, Bangladesh and West Bengal. *Appl Geochem.* 15:403–413.
- Pradhan SS, Konwar K, Ghosh TN, Mondal B, Sarkar SK, Deb P. 2020. Multifunctional iron oxide embedded reduced graphene oxide as a versatile adsorbent candidate for effectual arsenic and dye removal. *Coll Inter Sci Comm.* 39:100319.
- Qiao J, Jiang Z, Sun B, Sun Y. 2012. Arsenate and arsenite removal by FeCl₃: effects of pH, As/Fe ratio, initial As concentration and co-existing solutes. *Sep Purif Tech.* 92:106–114.
- Raj SK, Sharma J, Kulshrestha V. 2021. Facile synthesis of reusable graphene oxide composite magnetic beads for removal of arsenic (III). *SPE Polymers.* 2:74–85.
- Ren G, Qui H, Wu Q, Li H, Fan H, Fang C. 2010. Thermal stability of composites containing HCl-doped polyaniline and Fe nanoparticles. *Mater Chem Phys.* 120:127–133.
- Roberts LC, Stephan JH, Andreas V, Jessica D, Ruben K, Bernhard W, Ganesh CS, Badruzzaman ABM, Ali MA. 2011. Arsenic dynamics in porewater of an intermittently irrigated paddy field in Bangladesh. *Environ Sci Technol.* 45:971–976.
- Sahu JN, Zayed H, Karri RR, Shams S, Qi X. 2019. Applications of nano-biotechnology for sustainable water purification. *Indus Appl Nanomat.* 1:313–340.
- Shao W, Li X, Cao Q, Luo F, Li J, Du Y. 2008. Adsorption of arsenate and arsenite anions from aqueous medium by using metal(III)-loaded amberlite resins. *Hydrometallurgy.* 91:138–143.
- Smedley PL, Kinniburgh DG. 2002. A review of the source, behaviour and distribution of arsenic in natural waters. *Appl Geochem.* 17:517–568.
- Sreeprasad TS, Maliyekkal SM, Lisha KP, Pradeep T. 2011. Reduced graphene oxide–metal/metal oxide composites: facile synthesis and application in water purification. *J Hazard Mater.* 186:921–931.
- Sultana S, Bordoloi S, Konwer S, Borah G, Gogoi PK. 2020. Reduced graphene oxide/iron oxide hybrid composite material as an efficient magnetically separable heterogeneous catalyst for transfer hydrogenation of ketones. *Appl Organ Chem.* 34(5):e5582.
- Tang W, Li Q, Gao S, Shang JK. 2011. Arsenic (III, V) removal from aqueous solution by ultrafine a-Fe₂O₃ nanoparticles synthesized from solvent thermal method. *J Hazard Mater.* 192:131–138.
- Thomas S, Choong Y, Chuah TG, Robiah Y. 2007. Gregory FL azni I, arsenic toxicity, health hazards and removal techniques from water: an overview. *Desalination.* 217:139–166.
- Trchová M, Stejskal J. 2011. Polyaniline: The infrared spectroscopy of conducting polymer nanotubes (IUPAC technical report)*. *Pure Appl Chem.* 83:1803–1817.
- USEPA. 2000. Office of water: technologies and costs for removal of arsenic from drinking water. EPA.815-R-00-028.
- Vasaki M, Karri RR, Ravindran G, Paramasivan B. 2021. Predictive capability evaluation and optimization of sustainable biodiesel production from oleaginous biomass grown on pulp and paper industrial wastewater. *Renew Energy.* 168:204–215.
- Wang S, Gao B, Li Y, Elise AC, He F. 2017. Adsorptive removal of arsenate from aqueous solutions by biochar supported zero-valent iron nanocomposite: batch and continuous flow tests. *J Hazard Mater.* 322:172–181.
- Wang C, Lu H, Zhang Z, Wu Y, Zhang J, Chen S. 2014. Removal of As(III) and As(V) from aqueous solutions using nanoscale zero valent iron-reduced graphene oxide modified composites. *J Hazard Mater.* 268:124–131.
- WHO, Environmental Health Criteria 224. 2001. *Arsenic and arsenic compounds.* Geneva: WHO.
- Wickramasinghe SR, Han B, Zimbron J, Shen Z, Karim MN. 2004. Arsenic removal by coagulation and filtration: comparison of groundwaters from the United States and Bangladesh. *Desalination.* 169:231–244.
- Xie X, Ellis A, Wang Y, Xie Z, Duan M, Su C. 2009. Geochemistry of redox-sensitive elements and sulfur isotopes in the high arsenic groundwater system of Datong Basin, China. *Sci Total Environ.* 407:3823–3835.
- Yoon J, Amy G, Chung J, Sohn J, Yoon Y. 2009. Removal of toxic ions (chromate, arsenate, and perchlorate) using reverse osmosis, nanofiltration, and ultrafiltration membranes. *Chemosphere.* 77:228–235.
- Zhang K, Dwivedi V, Chi C, Wu J. 2010a. Graphene oxide/ferric hydroxide composites for efficient arsenate removal from drinking water. *J Hazard Mater.* 182:162–168.
- Zhang S, Li XY, Chen JP. 2010b. Preparation and evaluation of a magnetite-doped activated carbon fiber for enhanced arsenic removal. *Carbon.* 48:60–67.
- Zhang G, Ren Z, Zhang X. 2013. Nanostructured iron(III)-copper(II) binary oxide: A novel adsorbent for enhanced arsenic removal from aqueous solutions. *J Chem Water Res.* 47:4022–4031.
- Zhu H, Jia Y, Wu X, Wang H. 2009. Removal of arsenic from water by supported nano zero valent iron on activated carbon. *J Hazard Mater.* 172:1591–1596.



Comparative study of miracle leaf extracts reduced graphene oxide (m-rGO) and chemically synthesized graphene oxide (GO) as methanol gas sensor

Biswajit Pegu¹, Shreemoyee Bordoloi^{1,2,*}, Ratan Boruah³, and Surajit Konwer^{1,*}

¹Department of Chemistry, Dibrugarh University, Dibrugarh 786004, Assam, India

²Department of Chemistry, MDKG College, Dibrugarh 786004, India

³SAIC, Tezpur University, Tezpur 784028, Assam, India

Received: 29 June 2022

Accepted: 20 October 2022

© The Author(s), under exclusive licence to Springer Science+Business Media, LLC, part of Springer Nature 2022

ABSTRACT

A novel, green, bio-inspired synthesis of miracle leaf extracts reduced graphene oxide (m-rGO) nanosheets was explored. Here, graphene oxide (GO) was prepared using modified Hummers method from graphite powder and then reduced by miracle leaf extracts to produce m-rGO. The prepared m-rGO and chemically prepared GO was characterized by scanning electron microscopy (SEM), powder x-ray diffraction (XRD) analysis, transmission electron microscopy (TEM), Fourier transform infrared (FTIR) spectroscopy, Raman Spectroscopy and UV-Visible Spectroscopy. The XRD, FTIR, and Raman confirm the oxidation and reduction process. SEM and TEM images showed wrinkled sheet structure for green-synthesized reduced graphene oxides. The synthesized m-rGO products were investigated as a methanol gas sensor at ambient temperature using laboratory-made sensor setup. The sensing characteristics were monitored by measuring the change in electrical resistivity on exposure to methanol vapor at different concentrations. It is observed that the electrical response and % sensitivity of m-rGO toward methanol vapor is found to be a highly sensitive (254.7) than that of GO (27.7). The basic mechanism of the interaction between methanol and GO is believed to be hydrogen bonding and π - π interaction. To the best of our knowledge, no study has been conducted on miracle leaf extracts reduced graphene oxide (m-rGO) using this environment friendly green method for application of methanol gas sensor.

Address correspondence to E-mail: shreemoyeebordoloi@dibru.ac.in; surajitkonwer@dibru.ac.in

1 Introduction

Graphene, one-atom-thick a very attractive two-dimensional sheet of sp^2 hybridized hexagonal carbon nanomaterial has attracted incredible attention due to its excellent mechanical flexibility, superior electrical conductivity, high thermal and chemical stability has attracted scientific researchers from all across the world [1–10]. For these reasons, a reliable method for producing large-area single-crystalline graphene at reasonable price is an essential requirement. There are many techniques [11–14] have been introduced to synthesize graphene based on its application, cost effectiveness and eco-friendliness.

The most extensively used approach for synthesizing Graphene Oxide (GO) was Hummers method [15]. Although this method has some drawbacks viz., the liberation of hazardous gases (NO_2 and N_2O_4) during oxidation, difficulties of removal of Na^+ and NO_3^- ions from the residual water GO is highly oxidized form of graphite which retains the similar structure (multilayer) of its precursor although with a higher interlayer spacing due to the presence of oxygen functionalities [16]. According to widely accepted Lerf–Klinowski model, the basal-plane of the graphite oxide is highly populated with hydroxyls and epoxide while the edge-plane mainly consists of carboxyl and carbonyl groups [17]. The removal of these oxygen moieties is a significant topic that determines the properties of the ultimate product and to which extent rGO will resemble pristine graphene [18, 19]. Therefore, finding a suitable reducing agent for this task is very important.

There are many reducing agents have been introduced to remove the oxygenated functional groups from graphene oxides [20–22] and the reducing agents are categorized into two groups, (i) reducing agents under well-supported mechanism and (ii) reducing agents under proposed mechanism. The reducing agents under well-supported mechanism are traditionally applied in synthetic chemistry and have shown specific mode of reaction toward oxygenated functional groups. They are generally highly toxic and expensive, such as hydrazine and its derivatives [23], sodium borohydride [24], lithium aluminum hydride [25, 26] etc. The reducing agents ‘proposed’ mechanisms include reducing agents that have not been previously applied in synthetic chemistry as reducing agents and also do not have any definite modes of reaction toward specific

oxygen moieties. In addition, most of these have non-specific antioxidant or oxygen scavenging properties, e.g., plant extract [27], amino acid [28], microorganism [29] etc.

Dealing with toxic chemicals enhances the individual health risks as well as the surroundings. Several plants extracts have been investigated by several researchers for reduction of GO due to non-toxic, environment friendly, easily availability, safe to handle and relatively more stable in nature [27, 30–37]. Hence, we used a green method using natural reducing agents where GO was reduced using bioreductant Miracle leaf (*Bryophyllum pinnatum*) extract. The scientific name of Miracle plant is *Kalanchoe pinnata*. *Kalanchoe pinnata* is a medicinal plant largely used folk medicine for treatment of kidney stones, gastric ulcer, pulmonary infection and rheumatoid. It is found in Asia, Australia, New Zealand, West Indies, Marconesia, Polynesia and Hawaii. Phytochemicals contains in Miracle plant are alkaloid, flavonoids, phenolic compound, tannins, macro element: magnesium, calcium, potassium, phosphorous, sodium, and microelement: zinc, vitamins, ascorbic acid, riboflavin, thiamine, niacin [38]. In the most of research article reported that the antioxidant and reducing activity of plants are due to redox behavior of phenolic compounds and also these phenolic compounds are acts as hydrogen donors, reducing agents and singlet oxygen quencher. The phenolic compounds contains in *Kalanchoe pinnata* are flavonoid and phenolic acid, e.g., caffeic, ferulic and protocatechuic acid [39].

The detection of polluted gases, especially toxic gases are important to get clean the environment. Out of various pollutant gases the methanol vapor is one of the most extensively studied gases and also popular gases in industry and day to day life, so it is important to detect and control leaks in mobile practical devices as well as distribution lines of industry.

In the present work, the aqueous extract of Miracle leaf has been used for reduction of GO and studied the sensing behavior of reduced GO for methanol vapors in different analyte concentrations. The sensitivity has been studied with respect to the change in resistivity on exposure to methanol vapors. To the best of our knowledge, no article has been published to address the reduction of GO using Miracle leaf and studied as methanol sensor element. The cost-effective and green proposed method has the potential for

mass production of m-rGO with low-cost and no environmental pollution may open up a new route to develop an efficient gas sensor device.

2 Experimental

2.1 Materials and chemicals

Graphite powder was purchased from Chemical biochemical, Potassium permanganate (KMnO_4) was obtained SDFCL (SD Fine chem. Ltd., India) and Sodium Nitrate (NaNO_3) was received from Thermo Fischer Scientific India Pvt. Ltd., sulphuric acid (H_2SO_4), hydrochloric acid (HCl) and hydrogen peroxide (H_2O_2) were purchased from RANKEM, India. All reagents were used as received without further purification. Miracle leaves were collected from Dibrugarh University's campus, Dibrugarh, India.

2.2 Preparation of graphene oxide (GO)

GO was prepared via modified Hummers method by oxidizing the graphite powder as previously reported by us [40, 41]. In this process, graphite (2.5 gms) and NaNO_3 (1.25 gms) were mixed with 60 ml of conc. H_2SO_4 and stirred for 30 min at 0–5 °C. KMnO_4 (7.5 g) was slowly added maintaining the temperature ~ 0–5 °C for 90 min and then the mixture was stirred at room temperature (RT) for 24 h. Finally, 115 ml of water was added in the resulting mixture and temperature increase to 98 °C. After 30 min, 30% H_2O_2 (15 ml) was slowly added and then the color of the solution turns from brown to yellow. For purification, the mixture was washed by rinsing and centrifugation with 5% HCl and then de ionized water for several times then filtered and dry under vacuum to get final gray colored powder GO.

2.3 Collection of the leaves

Bryophyllum pinnatum, commonly known as *Dupor-Tenga* or *miracle plant*. The leaves of miracle plant were identified by a research scholar in the Department of Chemistry of Dibrugarh University, Dibrugarh, Assam, India. Nonetheless, the leaves were collected from the garden and premises of the Dibrugarh University and were therefore transported to the laboratory immediately for processing. The leaves were not exposed to direct sunlight so that the

active compounds are not lost The leaves were washed using tap water followed by deionized water for several times to remove dust and then dried in the vacuum oven at 40 °C for 3 days.

2.4 Preparation of extracts

The dried leaves were ground into a crude powder using manual grinder. The hot water (aqueous) extract was prepared by putting 10 g of fine powder with 100 ml distilled water into a 250 ml flask. This was heated to boil for one hour using a hot plate and stirred regularly for 3–5 min. After cooling, the resulting solution was filtered using Whatmann No 1 filter paper and takes the filtrate (Fig. 1).

2.5 Reduction of GO using miracle leaf extract

50 mg of GO was mixed with 30 ml of miracle extract and sonicated for 15 min. The resulting dispersed solution was refluxed at 90 °C under N_2 atmosphere followed by 2 h stirring. As the reaction progressed, color of the solution changed from brown to black (Fig. 2). Finally, the resulting solution was filtered and washed several times with water and ethanol to get Miracle extracts reduced graphene oxide (m-rGO).

The flow chart (Fig. 3) of total experimental procedure to prepare GO and reduced graphene oxide using miracle leaf abstract as-

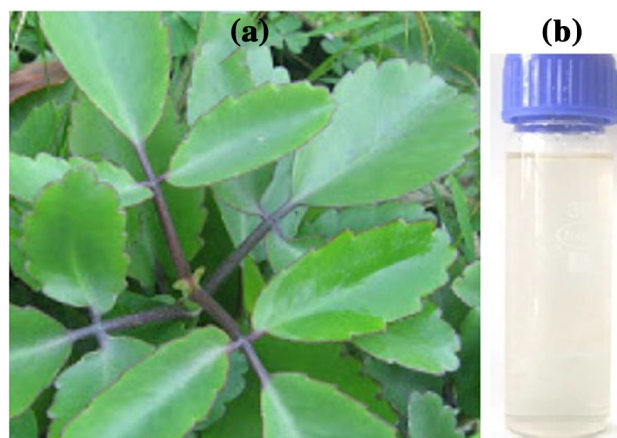


Fig. 1 a Photograph of Miracle plant and b Miracle leaf extract

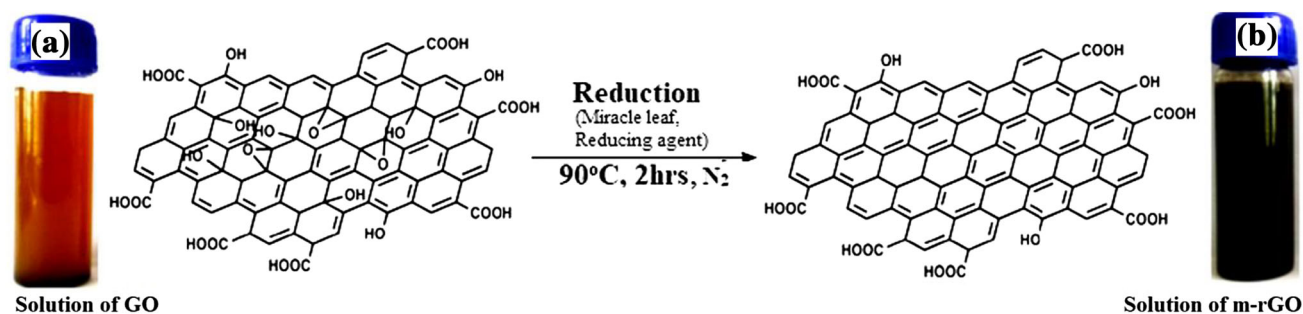
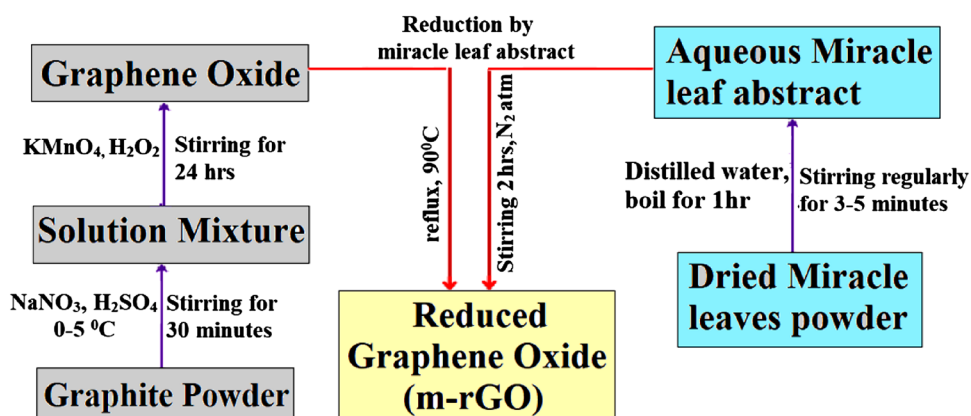


Fig. 2 Reduction of graphene oxide, (a) Solution of Graphene oxide, (b) Miracle extracts reduced graphene oxide (m-rGO)

Fig. 3 Flow-chart of preparation procedure of GO and m-rGO



2.6 Characterization

Fourier transform infrared spectroscopy (FTIR) was used to record FTIR spectra by Impact 410, Nicolet, USA, using KBr pellets. The x-ray diffraction (XRD) study was performed at RT on Rigaku x-ray diffractometer with Cu K α radiation ($\lambda = 0.15418$ nm). The surface morphology of GO and m-rGO was studied by SEM image with model JSM-6390LV, JEOL, Japan. The nanostructure of m-rGO was investigated with the help of Transition electron microscopy (TEM, JEOL JEM-2200 FS). The thermal decomposition curve was obtained from thermo gravimetric analysis. The ultraviolet-visible (UV-Vis) absorption spectroscopy of the samples in 1-Methyl-2-pyrrolidone solvent was recorded using Shimadzu UV-2550 UV-Vis spectrophotometer. Using a compression-molding machine with hydraulic pressure; pellets of composite samples were made. High pressure was applied (1.5–2 ton) to the sample to get hard round-shaped pellet (1.5 cm diameter, 2 mm breadth), which was used to measure the electrical conductivity. I-V calculations were recorded by Keithley 2400 source meter at the RT in the frequency range

102–106 Hz and at the scan rate 0.1 V/s within a voltage range of -10 V to $+10$ V.

2.7 Sensor testing measurements

The sensor set up for study the methanol gas sensing behavior of GO and m-rGO is shown in Fig. 4. Here the sensor material was heated at 80 °C for 24 h to remove excess solvent present in the material and

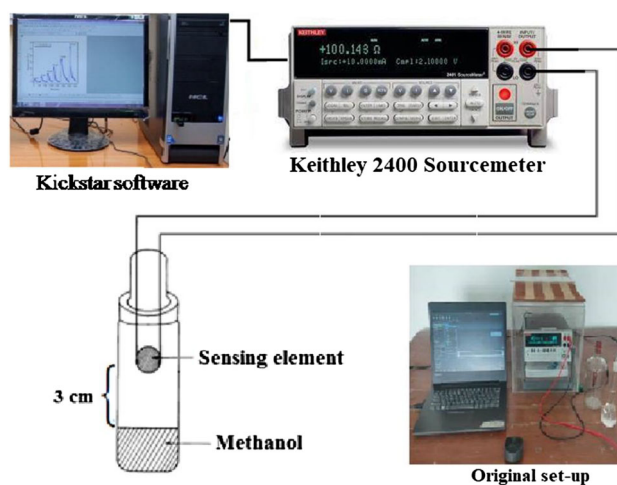


Fig. 4 Methanol vapors sensor set – up

then it was placed into the closed chamber. The contact between the sensor (as pellets) and the two probes was made with the help of silver paste and ~ 3 cm distance was fixed with the sensing material and methanol. The electrical response (i.e., resistance) was studied at RT via Keithley 2400 source meter using Kickstar software with scan rate 0.1 V/s. Hexane was used as diluents to obtain different concentration of the methanol vapors.

3 Results and discussion

In the FTIR spectra of GO (Fig. 5a), the peaks at 1037 cm^{-1} , 1221 cm^{-1} , 1396 cm^{-1} , 1623 cm^{-1} , 1718 cm^{-1} and a broad band at around 3421 cm^{-1} corresponded to C–O stretching vibrations, –C–O–C stretching, C–OH stretching, C=C stretching mode of the sp^2 carbon skeletal network, C=O stretching and O–H stretching vibration, respectively [42, 43]. The two small peaks near $\sim 2912\text{ cm}^{-1}$ and $\sim 2806\text{ cm}^{-1}$ are corresponding to the H-bonded OH groups of dimeric COOH groups and intramolecular bonded O–H stretching of alcohols, respectively [44]. These indicated the presence of oxygen-containing moieties such as carbonyl, carboxylic, epoxy and hydroxyl in GO. The reduction of graphene oxide clearly established by the disappearance of the some bands from the respective spectra and the decrease in the intensity of the broad band at 3421 cm^{-1} for the hydroxyl group (Fig. 5b) [45].

The characteristic XRD diffraction peak of GO at around $2\theta = 10.45^\circ$ highlighted the introduction of

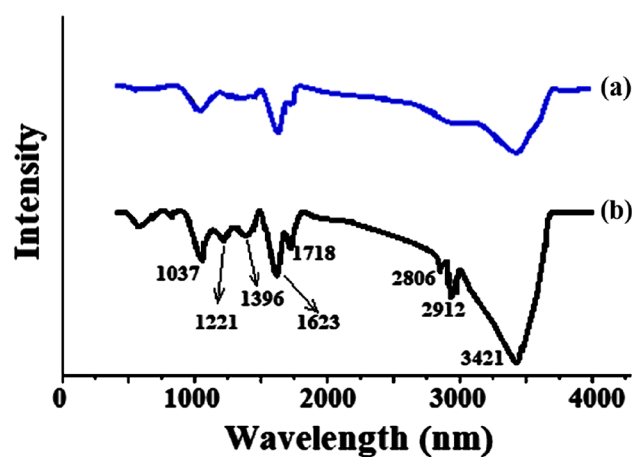


Fig. 5 FTIR spectra of GO and m-rGO

oxygenated functional groups with an interlayer spacing 'd' of 8.46 \AA (Fig. 6a) and the peak at around 42.41 correspond to the reflection from (100) plane with the interlayer distance 2.13 \AA as reported elsewhere [46]. The small peak at 10.55 in M-rGO reveals the presence of a small amount of residual oxygen functionalities during reduction, which is also supported by the literature. This removal of oxygen-containing functional groups is in agreement with the FTIR results as discussed in the above section. During reduction, the interlayer distance decreases due to the removal of oxygenated functional groups, and a characteristic broad peak reappearance at $2\theta = 29.53$ (Fig. 6b) reveals the restoration of an ordered crystal structure. This indicates the successful formation of m-rGO nanosheets with several layers of thickness after treating GO with the phytochemicals.

SEM image of m-rGO (Fig. 7a) shows the well-exfoliated flake-like sheets which also support by TEM image (Fig. 7b). TEM image suggest that the m-rGO layers are very transparent, silky and the ordered graphitic lattices are clearly visible. The selected area electron diffraction (SAED) pattern of m-rGO (Fig. 6c) confirms the crystalline structure which also corroborated with the XRD analysis.

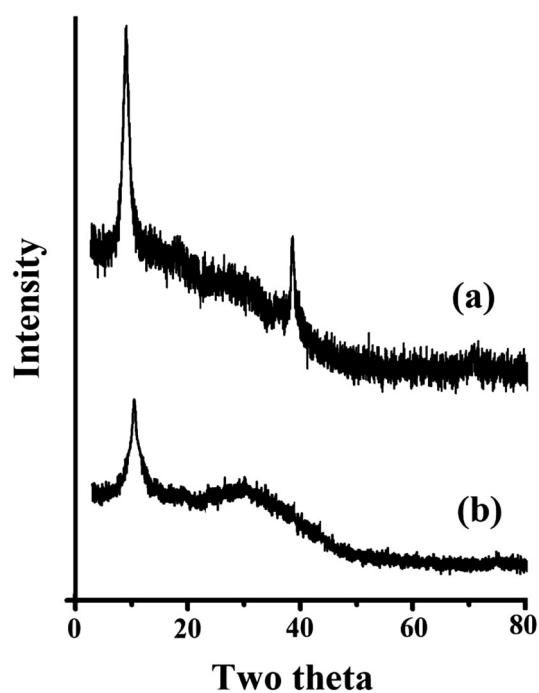


Fig. 6 XRD of (a) GO and (b) m-rGO

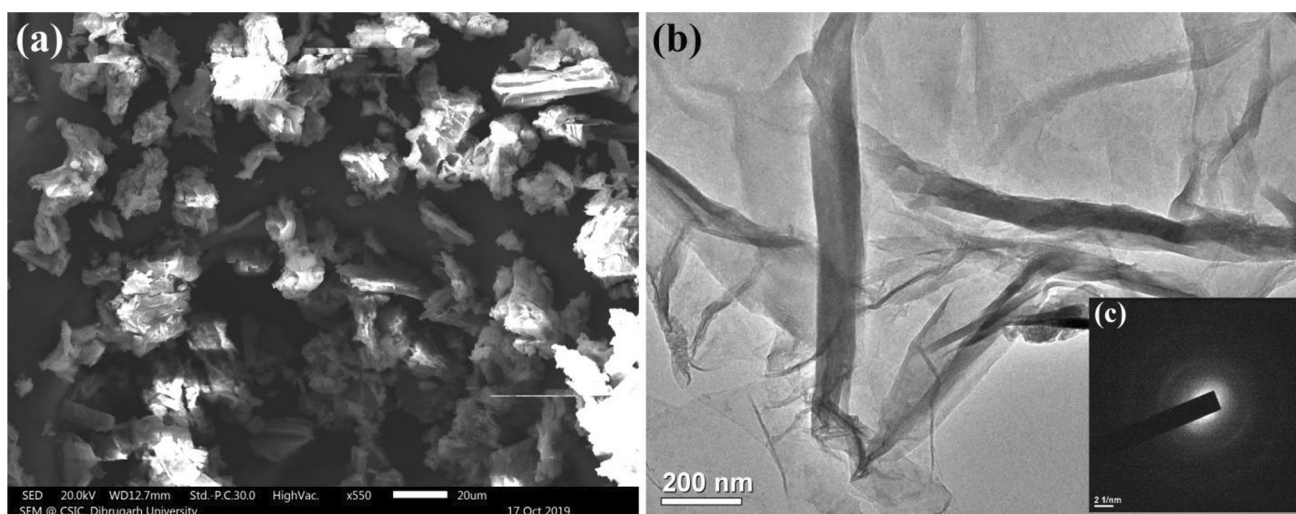


Fig. 7 a SEM image, b TEM image and c SAED pattern of m-rGO

The thermal stability of m-rGO and GO were studied (Fig. 8) and around 100 °C the minute weight indicated the elimination of residue water molecules present in the samples. In GO (Fig. 8a) the initial weight loss at ~ 200 °C is probably due to the loss of oxygen-containing functional groups and the major weight loss around 410–440 °C is due to the pyrolysis of residual oxygen functional groups and ring carbons to yield CO and CO₂ [47]. The thermal stability of m-rGO (Fig. 8b) showed by better than GO and slight weight loss at around 230–250 °C indicates the presence of very less amount of oxygen functional group than that of GO i.e., the higher degree of reduction.

Figure 9 showed the UV–visible spectra obtained for GO and m-rGO by dispersed in distilled water.

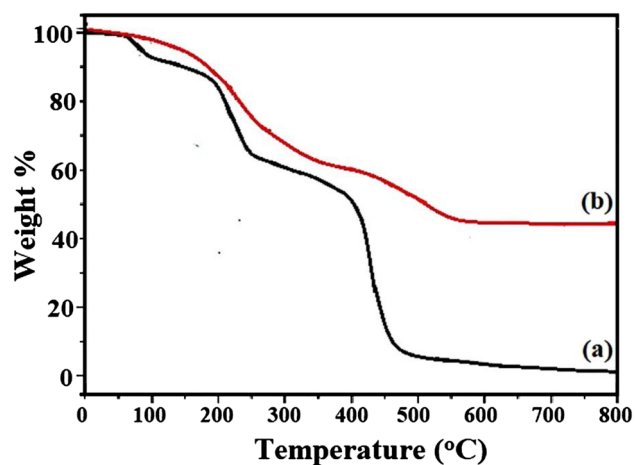


Fig. 8 TGA plot of (a) GO and (b) m-rGO

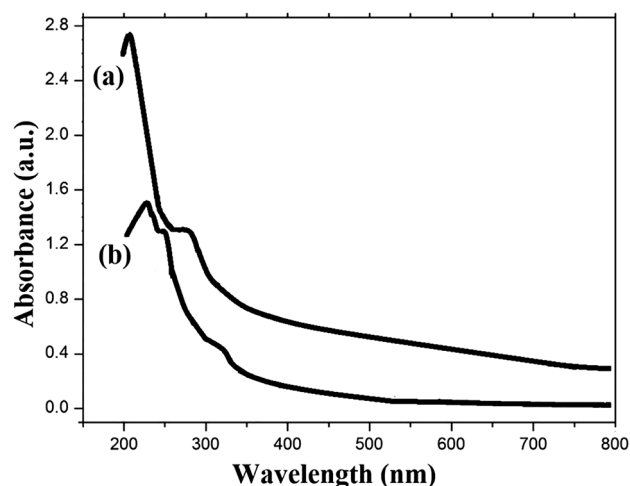


Fig. 9 UV–vis spectra for (a) m-rGO and (b) GO

For GO, the spectra exhibit a maximum absorption peaks at 250 nm with a shoulder peak at 310 nm corresponds to $n-\pi^*$ transition of aromatic C–C bonds and $n-\pi^*$ transition of C=O, respectively [48]. It is clearly noticed that the absorption peak shows a larger red shift in m-rGO (290 nm) which confirm the reduction of GO.

In the Raman spectra of pristine GO (Fig. 10a) and m-rGO (Fig. 10b) showed the decreased in the position of D and G band with intensity ratio I_D/I_G for m-rGO as compared to pristine GO. This small decrease may be due the result of reduction of oxygen moieties in GO. In addition, a small deviation in the centers of D and G bands of m-rGO from GO is also observed which must be due to the presence of less oxygen moieties in reduce graphene oxide.

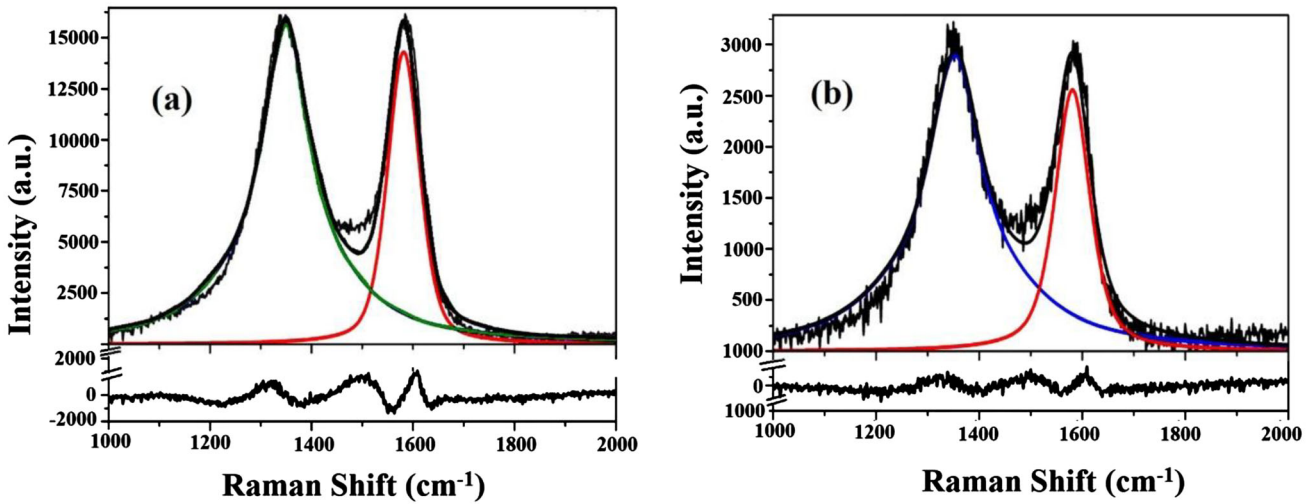


Fig. 10 Raman spectra of a pristine GO and b m-rGO

4 I/V characteristics and methanol gas sensing study

The electrical behavior of the GO and m-rGO were studied with the help of current–voltage characteristics at RT using a Keithley 2400 source meter in the potential span of -10 V to $+10\text{ V}$. The current–voltage response was significantly increased by m-rGO sheet and both GO and m-rGO exhibited semiconducting behavior (Fig. 11).

The gas sensing property of GO and m-rGO were studied using Keithley 2400 source meter by calculating real-time monitoring of Chemiresistive response (i.e., change in resistive and current as a function of time) at RT on exposing to different concentrations of methanol vapors. The sensor

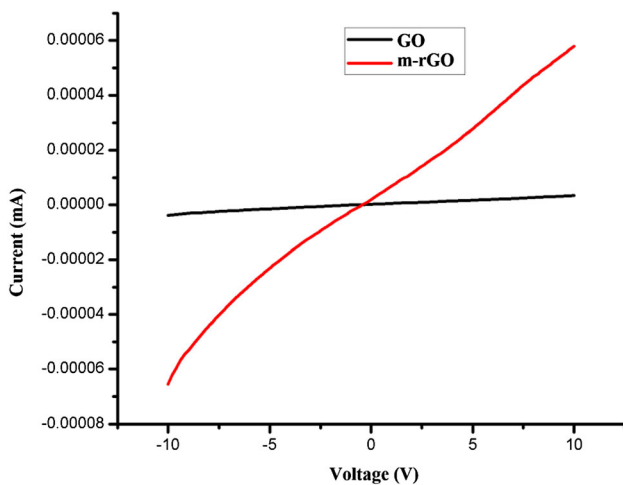


Fig. 11 I-V characteristics of GO and m-rGO

response was studied as the difference between the resistivity of the sensor device after and before exposure to methanol gases with the following equation:

$$\text{Response (\%)} = 100 \times \frac{R - R_0}{R_0}, \quad (1)$$

where, R_0 and R are the initial resistance of sensor in air and in target gas, respectively. The response time is described as the time required reaching the maximum resistance change, whereas the recovery time is described as the time required to reach the initial resistance of the device.

The I-V characteristic and Chemiresistive responses of GO and m-rGO toward methanol gas (500 ppm) at RT are shown in Fig. 12 and found that

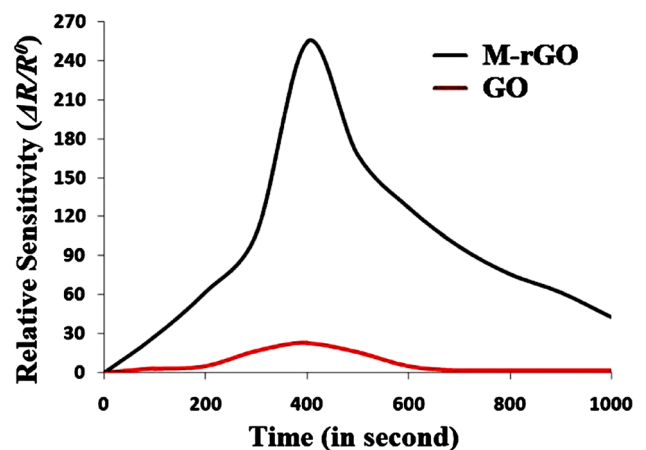


Fig. 12 Relative sensitivity of GO and m-rGO for 500 ppm methanol at room temperature

the sensors' resistance increased dramatically when they were exposed to the methanol gas. Which may be due to switching of p-type to n-type i.e., when gas sensor exposed by methanol they may lead to the surface adsorbed active sites redistribution and also capture the electron from pellet which may increase the sensor resistance.

Since methanol is a highly polar vapor; there is a possibility to hydrogen bonding interactions during adsorption on the sensing material. Also there is a possibility to form π - π interaction in between GO sheets which makes the material more stable in nature (Fig. 13). From the gas-sensing characteristic curves, the increased gas sensitivity of m-rGO due to availability of sufficient oxygen dangling bonds after reduction by green miracle leaf abstract. In addition the better gas sensitivity m-rGO with respect to pristine GO is due to higher defect concentration in m-rGO supported by Raman studies. Therefore these defects may act as a preferential adsorption sites for methanol gas [47].

A histogram of relative sensitivity for 500 ppm methanol of GO *vs.* m-rGO (Fig. 14) indicates relative sensitivity of green-synthesized M-rGO; 254.7% at

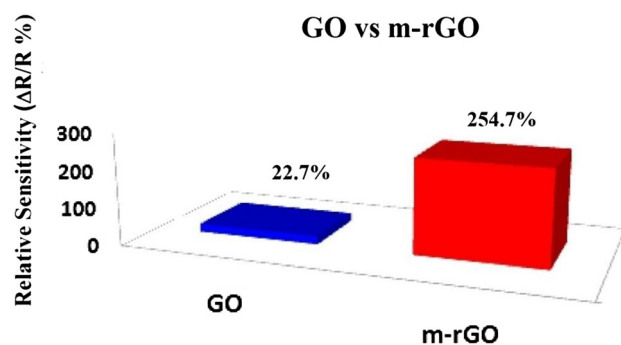


Fig. 14 Histogram of relative sensitivity of GO/m-rGO for 500 ppm methanol

room temperature which is much higher than that of GO (22.7%). Here we have compared our sensitivity result of recent green-synthesized M-rGO with earlier literature works and listed them in Table 1 and from the table it is clear that the methanol gas sensitivity of green-synthesized m-rGO is better than already published results. So finally we conclude that the miracle leaf reduced graphene oxide (m-rGO) is an effective and environment friendly methanol gas-sensing material with high sensitivity.

Fig. 13 Probable interaction of graphene oxide and methanol

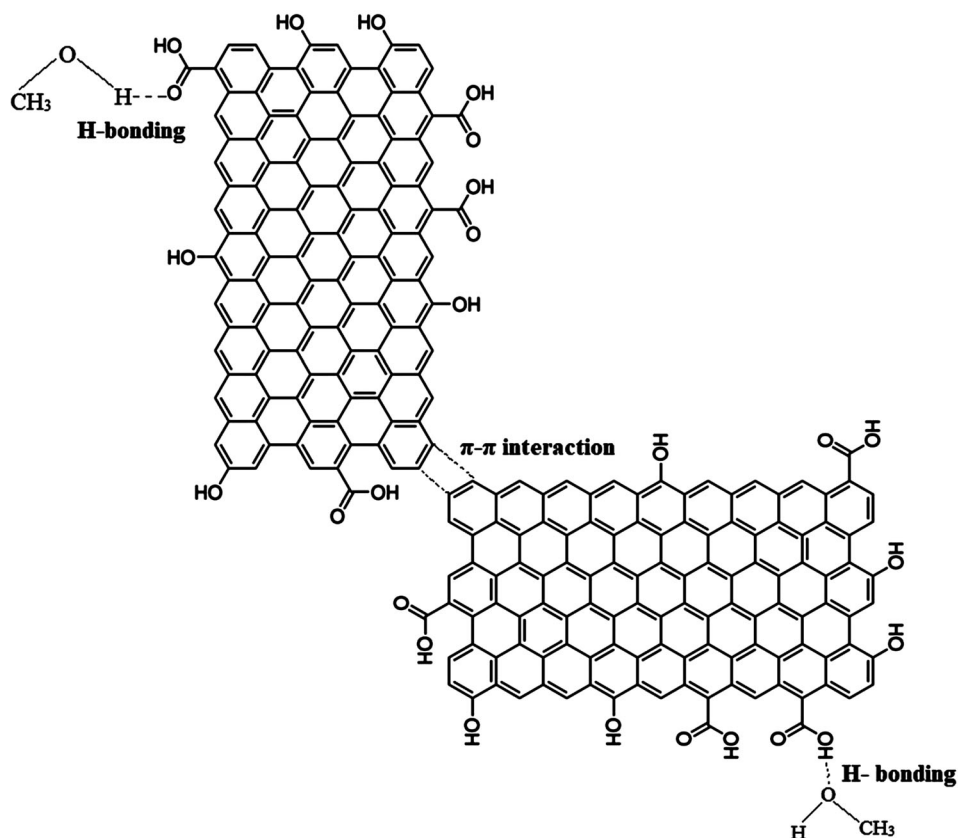


Table 1 Methanol sensitivity comparison with already published research papers

Sample	Sensor	Concentration range (ppm)	Sensitivity (%)	References
GO/polyindole	Methanol	1.14–11.36	7.37	[49]
GO/Polyaniline		100–500	20.9–37	[40]
GO/graphene foam		1500	Very low	[50]
rGO/NiO		100	61.15	[51]
GO/FET		150	127.93	[52]
thermally reduced GO		1500	1.5–2	[53]
m-rGO		500	254.7	Current study
GO		500	22.7	Current study

5 Conclusion

We have prepared graphene oxide (GO) by oxidation of graphite flakes using Hummer's method and then reduced with freshly prepared green reducing agent miracle leaf extracts (m-rGO). The DC electrical conductivity of the m-rGO is much higher in comparison with chemically prepared GO. On the basis of conducting behavior of the material; here we report a comparison study for methanol gas-sensing measurements of m-rGO and GO. FTIR confirm the presence of oxygen functionalities such as (–OH) hydroxyl and (–COOH) carboxylic in GO and also confirm its reduction to form m-rGO by miracle leaf abstract. In addition Raman spectroscopy also confirms reduction of oxygen moieties in m-rGO as the decreased ID/IG ratio for m-rGO as compared to GO. It is observed that the m-rGO is found to be a highly sensitive (% Sensitivity = 254.7) methanol sensor material than that of GO (% Sensitivity = 22.7). The basic mechanism of the interaction between methanol and GO is believed to be hydrogen bonding and π – π interaction. These observations paved the way of applicability of m-rGO to be a potential material for gas sensor and also motivate the researcher for the production of reduced graphene oxide without causing any harm to the environment.

Author contributions

All the authors have significantly contributed in this research work. BP: carried out the synthesis, characterization, and analysis of the compound and wrote the manuscript. SB: assisted in the conceptualization, review, and editing of the manuscript. RB: carried out the characterization part. SK: supervised the entire research work.

Funding

The author S. Bordoloi acknowledges Science and Engineering Research Board (SERB), India for providing research grant [No. SR/WOS-A/CS-161/2016].

Data availability

The authors declare that all the data supporting the findings of this study are available within the article.

Declarations

Conflict of interest The authors declare that they have no conflict of interests.

References

1. K.S. Novoselov, A.K. Geim, S.V. Morozov, D.E. Jiang, Y. Zhang, S.V. Debonis, I.V. Grigorieva, A.A. Firsov, *Science* **306**, 666–669 (2004). <https://doi.org/10.1126/science.1102896>
2. A.K. Geim, Graphene: status and prospects. *Science* **324**, 1530–1534 (2009). <https://doi.org/10.1126/science.1158877>
3. M. Coroş, F. Pogăcean, L. Măgeruşan, C. Socaci, S. Pruneanu, *Front Mater. Sci.* **13**, 23–32 (2019). <https://doi.org/10.1007/s11706-019-0452-5>
4. P. Tambe, *Mater. Today Proc* **49**, 1294–1297 (2022). <https://doi.org/10.1016/j.matpr.2021.06.381>
5. C. Kavitha, *Mater. Today Proc.* **49**, 811–816 (2022). <https://doi.org/10.1016/j.matpr.2021.05.343>
6. C.I. Justino, A.R. Gomes, A.C. Freitas, A.C. Duarte, T.A. Rocha-Santos, *TrAC Trend. Ana. Chem.* **91**, 53–66 (2017). <https://doi.org/10.1016/j.trac.2017.04.003>

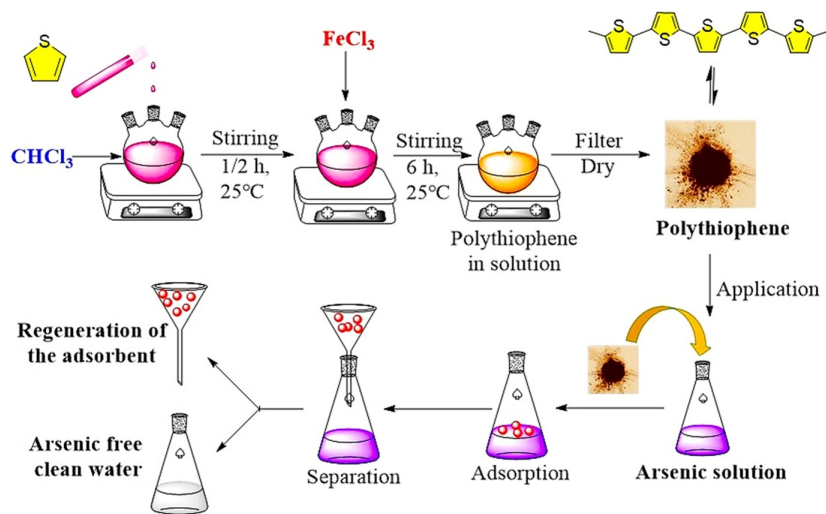
7. S. Sikiru, O.T. Lekan, Y.K. Sanusi, A.A. Adewale, A.A. OJCurr, *Nanosci.* **18**, 336–346 (2022). <https://doi.org/10.2174/1573413717666210702095201>
8. Y. Li, W. Gao, L. Ci, C. Wang, P.M. Ajayan, *Carbon* **48**, 1124–1130 (2010). <https://doi.org/10.1016/j.carbon.2009.11.034>
9. W. Liu, G. Speranza, *ACS Omega* **6**, 6195–6205 (2021). <https://doi.org/10.1021/acsomega.0c05578>
10. S. Konwer, L.J. Barthakur, S.K. Dolui, *J. Mater. Sci. Mater. Elect.* **23**, 837–845 (2012). <https://doi.org/10.1007/s10854-011-0503-x>
11. R. Munoz, C. Gómez-Aleixandre, *Chem. Vap. Depos.* **19**, 297–322 (2013). <https://doi.org/10.1002/cvde.201300051>
12. J.L. Qi, W.T. Zheng, X.H. Zheng, X. Wang, H.W. Tian, *Appl. Surf. Sci.* **257**, 6531–6534 (2011). <https://doi.org/10.1016/j.apsusc.2011.02.069>
13. Q. Huang, J.J. Kim, G. Ali, S.O. Cho, *Adv. Mater.* **25**, 1144–1148 (2013). <https://doi.org/10.1002/adma.201202746>
14. C.K. Chua, M. Pumera, *Chem. Soc. Rev.* **43**, 291–312 (2014). <https://doi.org/10.1039/C3CS60303B>
15. W.S. Hummers Jr., R.E. Offeman, Preparation of graphitic oxide. *J. Am. Chem. Soc.* **80**, 1339–1339 (1958). <https://doi.org/10.1021/ja01539a017>
16. R. Al-Gaashani, A. Najjar, Y. Zakaria, S. Mansour, M.A. Atieh, *Ceram. Int.* **45**, 14439–14448 (2019). <https://doi.org/10.1016/j.ceramint.2019.04.165>
17. A. Lerf, H. He, T. Riedl, M. Forster, J. Klinowski, *Sol. St. Ion.* **101**, 857–862 (1997). [https://doi.org/10.1016/S0167-2738\(97\)00319-6](https://doi.org/10.1016/S0167-2738(97)00319-6)
18. S. Pei, H.M. Cheng, *Carbon* **50**, 3210–3228 (2012). <https://doi.org/10.1016/j.carbon.2011.11.010>
19. J. Zhang, H.Y. Cao, J.Q. Wang, G.D. Wu, L. Wang, *Front. Cell Dev. Biol.* **9**, 616888 (2021). <https://doi.org/10.3389/fcell.2021.616888>
20. A.T. Smith, A.M. LaChance, S. Zeng, B. Liu, L. Sun, *Nano. Mater. Sci.* **1**, 31–47 (2019). <https://doi.org/10.1016/j.nanomater.2019.02.004>
21. J.I. Paredes, S. Villar-Rodil, M.J. Fernández-Merino, L. Guardia, A. Martínez-Alonso, J.M.D. Tascon, *J. Mater. Chem.* **21**, 298–306 (2011). <https://doi.org/10.1039/C0JM01717E>
22. B.S. Dash, G. Jose, Y.J. Lu, J.P. Chen, *Int. J. Mol. Sci.* **22**, 2989 (2021). <https://doi.org/10.3390/ijms22062989>
23. A. Furst, R.C. Berlo, S. Hooton, *Chem. Rev.* **65**, 51–68 (1965). <https://doi.org/10.1021/cr60233a002>
24. H.J. Shin, K.K. Kim, A. Benayad, S.M. Yoon, H.K. Park, I.S. Jung, M.H. Jin, H.K. Jeong, J.M. Kim, J.Y. Choi, Y.H. Lee, *Adv. Funct. Mater.* **19**, 1987–1992 (2009). <https://doi.org/10.1002/adfm.200900167>
25. A. Ambrosi, C.K. Chua, A. Bonanni, M. Pumera, Lithium-aluminum hydride as reducing agent for chemically reduced graphene oxides. *Chem. Mater.* **24**, 2292–2298 (2012). <https://doi.org/10.1021/cm300382b>
26. C.H.A. Wong, M. Pumera, *J. Mater. Chem. C.* **2**, 856–863 (2014). <https://doi.org/10.1039/C3TC31688B>
27. S. Thakur, N. Karak, *Carbon* **50**, 5331–5339 (2012). <https://doi.org/10.1016/j.carbon.2012.07.023>
28. D. Chen, L. Li, L. Guo, *Nanotechnology* **22**, 325601 (2011). <https://doi.org/10.1088/0957>
29. G. Wang, F. Qian, C.W. Saltikov, Y. Jiao, Y. Li, *Nano Res.* **4**, 563–570 (2011). <https://doi.org/10.1007/s12274-011-0112>
30. K. Muthoosamy, R.G. Bai, I.B. Abubakar, S.M. Sudheer, H.N. Lim, H.S. Loh, N.M. Huang, C.H. Chia, S. Manickam, *Int. J. Nanomedicine* **10**, 1505 (2015). <https://doi.org/10.2147/IJN.S75213>
31. Y. Wang, Z. Shi, J. Yin, A.C.S. Appl, *Mater. Interfaces* **3**, 1127–1133 (2011). <https://doi.org/10.1021/am1012613>
32. M. Khan, A.H. Al-Marri, M. Khan, M.R. Shaik, N. Mohri, S.F. Adil, M. Kuniyil, H.Z. Alkathlan, A. Al-Warthan, W. Tremel, M.N. Tahir, *Nanoscale Res. Lett.* **10**, 1–9 (2015). <https://doi.org/10.1186/s11671-015-0987-z>
33. B. Kartick, S.K. Srivastava, *J. Nanosci. Nanotechnol.* **13**, 4320–4324 (2013). <https://doi.org/10.1166/jnn.2013.7461>
34. B. Haghghi, M.A. Tabrizi, *RSC Adv.* **3**, 13365–13371 (2013). <https://doi.org/10.1039/C3RA40856F>
35. F. Tavakoli, M. Salavati-NiaAQAAsari, F. Mohandes, *Mater. Res. Bull.* **63**, 51–57 (2015). <https://doi.org/10.1016/j.materresbull.2014.11.045>
36. C. Li, Z. Zhuang, X. Jin, Z. Chen, *Appl. Surf. Sci.* **422**, 469–474 (2015). <https://doi.org/10.1016/j.apsusc.2017.06.032>
37. M. Khan, A.H. Al-Marri, M. Khan, N. Mohri, S.F. Adil, A. Al-Warthan, M.R.H. Siddiqui, H.Z. Alkathlan, R. Berger, W. Tremel, M.N. Tahir, *RSC Adv.* **4**, 24119–24125 (2014). <https://doi.org/10.1039/C4RA01296H>
38. A. QuaziMajaz, A.U. Tatiya, M. Khurshid, S. Nazim, S. Siraj, *Int. J. Res. Ayurveda Pharm.* **2**, 1478–1482 (2011)
39. A. Bogucka-Kocka, C. Zidorn, M. Kasprzycka, G. Szymczak, K. Szweczyk, *Saudi J. Biol. Sci.* **25**, 622–630 (2018). <https://doi.org/10.1016/j.sjbs.2016.01.037>
40. S. Konwer, A.K. Guha, S.K. Dolui, *J. Mater. Sci.* **48**, 1729–1739 (2013). <https://doi.org/10.1007/s10853-012-6931-z>
41. B. Pegu, S. Bordoloi, R. Boruah, S. Konwer, *Bull. Mater. Sci.* **44**, 1–9 (2021). <https://doi.org/10.1007/s12034-021-02540-0>
42. S. Konwer, R. Boruah, S.K. Dolui, *J. Electron. Mater.* **40**, 2248–2255 (2011). <https://doi.org/10.1007/s11664-011-1749-z>

43. N. Sharma, V. Sharma, Y. Jain, M. Kumari, R. Gupta, S.K. Sharma, K. Sachdev, Synthesis and characterization of graphene oxide (GO) and reduced graphene oxide (rGO) for gas sensing application. *Macromol. Symp.* **376**, 1700006 (2017). <https://doi.org/10.1002/masy.201700006>
44. T. Szabó, O. Berkesi, P. Forgó, K. Josepovits, Y. Sanakis, D. Petridis, I. Dékány, *Chem. Mater.* **18**, 2740–2749 (2006). <https://doi.org/10.1021/cm060258>
45. N.M.S. Hidayah, W.W. Liu, C.W. Lai, N.Z. Noriman, C.S. Khe, U. Hashim, H.C. Lee, *AIP Conference Proceedings*. AIP Publ LLC **1**, 150002 (2017). <https://doi.org/10.1063/1.5005764>
46. N.J. Panicker, P.P. Sahu, *J. Mater. Sci. Mater. Electron.* **32**, 15265–15278 (2021). <https://doi.org/10.1007/s10854-021-06077-0>
47. N. Sharma, R. Vyas, V. Sharma, H. Rahman, S.K. Sharma, K. Sachdev, *Appl. Nanosci.* **10**, 517–528 (2020). <https://doi.org/10.1007/s13204-019-01138-7>
48. J.I. Paredes, S. Villar-Rodil, A. Martínez-Alonso, J.M.D. Tascon, *Langmuir* **24**, 10560–10564 (2008). <https://doi.org/10.1021/la801744a>
49. K. Phasuksom, W. Prissanaroon-Ouajai, A. Sirivat, *RSC Adv.* **10**, 15206–15220 (2020). <https://doi.org/10.1039/D0RA00158A>
50. S. Aslam, T.H. Bokhari, T. Anwar, U. Khan, A. Nairan, K. Khan, *Mater. Lett.* **235**, 66–70 (2019). <https://doi.org/10.1016/j.matlet.2018.09.164>
51. C.A. Zito, T.M. Perfecto, C.S. Fonseca, D.P. Volanti, *New J. Chem.* **42**, 8638–8645 (2018). <https://doi.org/10.1039/C8NJ01061G>
52. A. Hazra, *IEEE Trans. Electron Devices* **67**, 5111–5118 (2020). <https://doi.org/10.1109/TED.2020.3025743>
53. A. Lipatov, A. Varezchnikov, P. Wilson, V. Sysoev, A. Kolmakov, *Nanoscale* **5**, 5426–5434 (2013). <https://doi.org/10.1039/C3NR00747B>

Publisher's Note Springer Nature remains neutral with regard to jurisdictional claims in published maps and institutional affiliations.

Springer Nature or its licensor (e.g. a society or other partner) holds exclusive rights to this article under a publishing agreement with the author(s) or other rightsholder(s); author self-archiving of the accepted manuscript version of this article is solely governed by the terms of such publishing agreement and applicable law.

Metadata of the article that will be visualized in OnlineFirst



Schematic diagram for the synthesis of PTh and adsorptive removal of arsenic from contaminated water.

ArticleTitle	One-Step Synthesis of Polythiophene as a Potential Adsorbent for Removal of <i>As (III)</i> and <i>As (V)</i> from Aqueous Solution	
Article Sub-Title		
Article CopyRight	The Author(s), under exclusive licence to Springer Nature Switzerland AG (This will be the copyright line in the final PDF)	
Journal Name	Water, Air, & Soil Pollution	
Corresponding Author	FamilyName	Gogoi
	Particle	
	Given Name	Ankur
	Suffix	
	Division	Department of Physics
	Organization	JB College
	Address	Jorhat, Assam, 785001, India
	Phone	
	Fax	
	Email	ankurgogoi@gmail.com
	URL	
	ORCID	
Corresponding Author	FamilyName	Konwer
	Particle	
	Given Name	Surajit
	Suffix	
	Division	Department of Chemistry
	Organization	Dibrugarh University
	Address	Dibrugarh, 786004, India
	Phone	
	Fax	
	Email	surajitkonwer@dibru.ac.in
	URL	
	ORCID	http://orcid.org/0000-0002-8878-7076
Author	FamilyName	Chetia

Particle
Given Name **Rupkamal**
Suffix
Division Department of Chemistry
Organization Dibrugarh University
Address Dibrugarh, 786004, India
Phone
Fax
Email
URL
ORCID

Author
FamilyName **Devi**
Particle
Given Name **Shrutipriya**
Suffix
Division Department of Chemistry
Organization Dibrugarh University
Address Dibrugarh, 786004, India
Phone
Fax
Email
URL
ORCID

Author
FamilyName **Bordoloi**
Particle
Given Name **Shreemoyee**
Suffix
Division Department of Chemistry
Organization MDKG College
Address Dibrugarh, Assam, 786001, India
Phone
Fax
Email
URL
ORCID

Author
FamilyName **Pokhrel**
Particle
Given Name **Binod**
Suffix
Division State Water Testing Laboratory
Organization Public Health Engineering and Water Supply Department
Address Itanagar, Arunachal Pradesh, 791111, India
Phone
Fax
Email
URL
ORCID

Author
FamilyName **Shukla**
Particle
Given Name **Nishant**
Suffix
Division Department of Physics
Organization JB College
Address Jorhat, Assam, 785001, India

Division	Department of Physics
Organization	Tezpur University
Address	Tezpur, Assam, 785028, India
Phone	
Fax	
Email	
URL	
ORCID	

Schedule	Received	7 Mar 2023
	Revised	
	Accepted	13 May 2023

Abstract

Abstract:

The present study deals with the adsorption of both *As (V)* and *As (III)* from aqueous solution using pristine polythiophene (PTh). Here PTh was prepared by chemical oxidative polymerization method using FeCl_3 as an initiator and characterized by FTIR, XRD, and SEM-EDX. Batch experiments were conducted to assess the effects of several experimental parameters such as pH, initial *As* concentration, and adsorbent dose on the removal of Arsenic (*As*). At low initial *As* concentration (100 $\mu\text{g/L}$) with pH range 3, 5, and 7, the prepared PTh showed 100% removal efficiency for both *As (III)* and *As (V)*. The adsorption process followed a pseudo-second-order kinetic model with linear regression coefficients (R^2) of 0.9976 and 0.9972 for the adsorption of *As (III)* and *As (V)* respectively. The Langmuir adsorption isotherm model fits well with *As* adsorption by PTh, demonstrating monolayer adsorption on the polymer. According to Langmuir's adsorption isotherm model calculations, PTh showed maximum adsorption capacities of 84.33 and 87.78 $\mu\text{g/g}$ for *As (III)* and *As (V)*, respectively. Feasible and spontaneous adsorption of *As* by PTh is indicated by the negative Gibbs free energy (ΔG°). To validate the *As* adsorption by PTh, DFT simulations were performed and found that the S of the polymer and O of the *As* species are responsible for the adsorption of *As* by PTh. Additionally, it can be shown that there is a Van-der-Waal type of interaction between hydrogen and oxygen molecules.

Graphical Abstract:

Keywords (separated by '-') Adsorption - Arsenic - Polythiophene - Water treatment

Footnote Information



1 One-Step Synthesis of Polythiophene as a Potential 2 Adsorbent for Removal of As (III) and As (V) from Aqueous 3 Solution

4 Rupkamal Chetia · Shrutipriya Devi ·
5 Shreemoyee Bordoloi · Binod Pokhrel ·
6 Nishant Shukla · Ankur Gogoi · Surajit Konwer

7 Received: 7 March 2023 / Accepted: 13 May 2023
8 © The Author(s), under exclusive licence to Springer Nature Switzerland AG 2023

AQ1 Abstract The present study deals with the adsorption of both As (V) and As (III) from aqueous solution using pristine polythiophene (PTh). Here PTh was prepared by chemical oxidative polymerization method using FeCl₃ as an initiator and characterized by FTIR, XRD, and SEM-EDX. Batch experiments were conducted to assess the effects of several experimental parameters such as pH, initial As concentration, and adsorbent dose on the removal of Arsenic (As). At low initial As concentration (100 µg/L) with pH range 3, 5, and 7, the prepared PTh showed 100% removal efficiency for both As (III) and As (V). The

adsorption process followed a pseudo-second-order kinetic model with linear regression coefficients (R^2) of 0.9976 and 0.9972 for the adsorption of As (III) and As (V) respectively. The Langmuir adsorption isotherm model fits well with As adsorption by PTh, demonstrating monolayer adsorption on the polymer. According to Langmuir's adsorption isotherm model calculations, PTh showed maximum adsorption capacities of 84.33 and 87.78 µg/g for As (III) and As (V), respectively. Feasible and spontaneous adsorption of As by PTh is indicated by the negative Gibbs free energy (ΔG°). To validate the As adsorption by PTh, DFT simulations were performed and found that the S of the polymer and O of the As species are responsible for the adsorption of As by PTh. Additionally, it can be shown that there is a Van-der-Waal type of interaction between hydrogen and oxygen molecules.

Keywords Adsorption · Arsenic · Polythiophene · Water treatment **AQ2** 40

1 Introduction **AQ3** 41

Arsenic pollution in water bodies is a severe problem that causes a variety of health issues; hence, the US Environmental Protection Agency (USEPA) established a maximum allowable level of 10 µg/L in potable water (Mondal et al., 2006). Because of the significant risk of health dangers

A1 R. Chetia · S. Devi · S. Konwer (✉)
A2 Department of Chemistry, Dibrugarh University,
A3 Dibrugarh 786004, India
A4 e-mail: surajitkonwer@dibru.ac.in

A5 S. Bordoloi
A6 Department of Chemistry, MDKG College, Dibrugarh,
A7 Assam 786001, India

A8 B. Pokhrel
A9 State Water Testing Laboratory, Public Health
A10 Engineering and Water Supply Department, Itanagar,
A11 Arunachal Pradesh 791111, India

A12 N. Shukla · A. Gogoi (✉)
A13 Department of Physics, JB College, Jorhat, Assam 785001,
A14 India
A15 e-mail: ankurgogoi@gmail.com

A16 N. Shukla
A17 Department of Physics, Tezpur University, Tezpur,
A18 Assam 785028, India

48 associated with As poisoning in water, As is one of
49 the world's major concerns when it comes to water
50 problems. It is the 20th most abundant element in
51 nature, the 14th most abundant in saltwater, and
52 the 12th most abundant in the human body (Man-
53 dal & Suzuki, 2002).

54 India, Bangladesh, Taiwan, Magnolia, China,
55 Chile, New Zealand, Hungary, Japan, Mexico,
56 and Poland are the primary countries affected by
57 the As issue (Pathan & Bose, 2018; Pucek et al.,
58 2013; Leaper et al., 2021; Yohai et al., 2019). As
59 originates from both natural and anthropogenic
60 sources. Due to its high toxicity, As pollutes our
61 water systems and harms human health in a num-
62 ber of ways. Its excessive concentration in the
63 human body can result in pigmentation changes,
64 hyperkeratosis, neurological problems, muscular
65 weakness, lack of appetite, and nausea in addition
66 to cancers of the skin, lungs, bladder, and kidney
67 (Raj et al., 2021; Horzum et al., 2013; Alam et al.,
68 2018; Paul et al., 2013). The USEPA has estab-
69 lished strict As regulatory standards as a result
70 of these many health risks. However, many other
71 nations throughout the world continue to use the
72 earlier established maximum permitted level of 50
73 $\mu\text{g/L}$ (Fan et al., 2016; Cooper et al., 2010; Zhang
74 et al., 2010; Wu et al., 2011; Assaad et al., 2020;
75 Mondal & Garg, 2017).

76 As is available in the inorganic state as oxides
77 (As_2O_3 , As_2O_5) and sulfides (As_2S_3 , AsS , HAsS_2 ,
78 HAsS_3^{3-}). It exists in -3 , 0 , $+3$, and $+5$ oxida-
79 tion levels, but is most commonly found in triva-
80 lent (As^{3+} , arsenite) and pentavalent (As^{5+} , arse-
81 nate) forms. Arsenate species are mostly found in
82 oxygen-rich aerobic environments, whereas arsenite
83 is found in considerably reduced anaerobic envi-
84 ronments, such as groundwater. Different forms
85 of As species predominate in nature at varying
86 pH and redox potential (E_h) levels, such as when
87 pH is less than roughly 6.7, H_2AsO_4^- predomi-
88 nates. HAsO_4^{2-} predominates at higher pH levels
89 (although H_3AsO_4 and AsO_4^{3-} may be found under
90 very acidic or basic circumstances, respectively).
91 The uncharged H_3AsO_4 predominates under reduc-
92 ing circumstances at pH levels lower than about 9.1
93 (Gupta et al., 2013; Shahyari et al., 2020; Makavi-
94 pour et al., 2019; Bordoloi et al., 2022; Cho et al.,
95 2014; Wen et al., 2015; Dutta et al., 2020).

96 Arsenic-contaminated water can be treated
97 using reverse osmosis, electro-coagulation, mem-
98 brane technology, oxidation, precipitation, coagu-
99 lation, electro-dialysis, and ion exchange tech-
100 nology. However, these treatment systems have
101 several drawbacks, including specialized instru-
102 mentation, difficult handling, excessive processing
103 costs, huge sludge output, and being less efficient
104 at low arsenic concentrations in water. Among all
105 the techniques, adsorption is considered most suit-
106 able technique due to its several advantages such
107 as cost-effectiveness, easy operation, high effi-
108 ciency, low maintenance, and minimum energy
109 requirement. Therefore, the adsorption technique
110 can be used at various scales ranging from house-
111 hold modules to community plants (Siddiqui &
112 Chaudhry, 2017; Yang et al., 2023a; Yang et al.,
113 2022a). Adsorption is a proven technique for
114 removing pollutants from contaminated water, but
115 scientists and engineers working on water research
116 have always been driven by the need to create
117 novel adsorbent materials with high adsorption
118 capacities. Consequently, a diverse range of adsor-
119 bents including ceramics, polymers, and ceramic/
120 polymer hybrids have been developed. Aromatic
121 conjugated polymers, including polyaniline,
122 polypyrrole, and PTh, are among the newcomers
123 in the field of the numerous polymers used to cre-
124 ate adsorbents for treating water pollutants (Dutta
125 & Rana, 2019). Polymers with the ideal skeletal
126 strength, tuneable surface functional groups, envi-
127 ronmentally benign, feasible regeneration, and
128 degradable qualities are suited for adsorbents.
129 Over the past few years, numerous scientific inves-
130 tations have focused heavily on PTh, because it
131 offers distinct features and adaptability, including
132 strong thermal, chemical, and environmental sta-
133 bility. Additionally, PTh is easily synthesized, has
134 good mechanical properties, and provides advan-
135 tages during processing. PTh can also interact with
136 polluting substances like heavy metals because of
137 their optimal molecular structure, surface area,
138 and number of binding sites (Karegar & Khodaei,
139 2022). Additionally, PTh has conjugated double
140 bonds in its backbone and by introducing polarons
141 and bipolarons into the backbone by either oxida-
142 tion or reduction making it a superb intrinsic con-
143 ducting polymer (Ramesan & Suhailath, 2017).

144 The design and synthesis of a selective and sta-
 145 ble adsorbent for heavy metal ion adsorption is still
 146 challenging, as most adsorbents could not exhibit
 147 selectivity towards specific ion in the mixture ion
 148 solution and the mechanism of the selective adsorp-
 149 tion is still unknown. In the present study, PTh is
 150 synthesized by simple oxidative polymerization
 151 using FeCl_3 as oxidant. Thus, produced pristine PTh
 152 is used for As removal from contaminated water. To
 153 the best of our knowledge concerned, this is the first
 154 account of the removal of As from polluted water
 155 with having low As concentration using solely pure
 156 PTh using FeCl_3 as an initiator. To demonstrate the
 157 effectiveness of the sorbent, appropriate analysis of
 158 the produced adsorbent and adsorption experiments
 159 was conducted.

160 2 Materials and Method

161 2.1 Materials

162 All of the chemicals utilized during this study
 163 were of the analytical grade and solutions were
 164 made in double-distilled water. NaAsO_2 and
 165 $\text{Na}_2\text{HAsO}_4 \cdot 7\text{H}_2\text{O}$ were obtained from Loba Che-
 166 mie Pvt. Ltd., Wodehouse Road, Mumbai 40005,
 167 India. Chloroform was purchased from Finar
 168 Chemicals, Gujarat, India. Thiophene monomer
 169 was procured from Spectrochem Pvt. Ltd., Mum-
 170 bai, India. FeCl_3 anhydrous was purchased from
 171 Qualikems Fine Chem Pvt. Ltd., Vadodara, India.
 172 Ethanol was procured from Analytical CSS Rea-
 173 gent, Jiangshu Province. A stock solution of a
 174 concentration of 100 mg/L for both As (III) and
 175 As (V) was prepared by dissolving NaAsO_2 and
 176 $\text{Na}_2\text{HAsO}_4 \cdot 7\text{H}_2\text{O}$ in water.

177 2.2 Synthesis of PTh

178 PTh was synthesized at room temperature (RT)
 179 via a simple oxidative polymerization technique.
 180 Firstly, 2 mL of thiophene monomer was added
 181 to a round bottom flask containing 30 mL chloro-
 182 form and stirred for 30 min. After that, anhydrous
 183 FeCl_3 (4 g) was added and allowed to stir (300
 184 rpm) at RT. After some time, a black-colored pre-
 185 cipitate was observed which confirms the forma-
 186 tion of PTh. Subsequently, the aforesaid mixture

was stirred for 6 h for complete polymerization of
 thiophene into PTh. Finally, the precipitate was fil-
 tered and washed with ethanol and distilled water.
 The product was dried overnight at 70 °C to get our
 desired PTh.

2.3 Instrumentation

The Fourier transform infrared (FTIR) spectra
 of all the samples were observed using spectrum
 IR, Perkin Elmer, USA. The surface morphol-
 ogy of all the samples and elemental analysis was
 done by scanning electron microscope (SEM),
 JEOLJSM-IT300, Japan. The XRD pattern of
 all the samples was obtained using Bruker D8
 Advance, USA. As concentration was evaluated
 using atomic absorption spectrometer (Thermo
 Scientific AAS, AA 303, USA).

2.4 Batch Experiment

The removal efficiency and the adsorption capac-
 ity (q_e) of the adsorbent at equilibrium were deter-
 mined using Eqs. (1) and (2) respectively, where q_e
 is the adsorption capacity (mg/g). C_i and C_e are the
 initial and equilibrium concentrations (mg/L) of the
 adsorbate, respectively. Again, V and W represent
 the solution volume (L) and adsorbent mass (g),
 respectively.

$$q_e = \frac{C_i - C_e}{W} \times V \quad (1)$$

$$\text{Removal efficiency}(\%) = \frac{C_i - C_e}{C_i} \times 100 \quad (2)$$

Adsorption isotherms (Langmuir and Freundlich)
 were used to investigate the equilibrium adsorp-
 tion properties. Equation (3) stands for Langmuir's
 isotherm.

$$\frac{1}{q_e} = \frac{1}{K_L q_{\max}} \frac{1}{C_e} + \frac{1}{q_{\max}} \quad (3)$$

where q_{\max} denotes the maximum adsorption capac-
 ity (mg/g) and K_L (L/mg), which represents the Lang-
 muir's isotherm constant and displays the binding
 affinity between As and the adsorbent.

Equation 4 was used to get the separation factor (R_L).

$$R_L = \frac{1}{1 + C_i \times K_L} \quad (4)$$

where R_L is the dimensionless Langmuir constant, which indicates the adsorption possibilities might be either favorable ($0 < R_L < 1$) or unfavorable ($R_L > 1$), linear ($R_L = 1$), or irreversible ($R_L = 0$).

The Freundlich's isotherm is represented by Eq. (5).

$$\text{Log}q_e = \text{Log}K_f + \frac{1}{n}\text{Log}C_e \quad (5)$$

K_f is the Freundlich's constant, which is used to measure the adsorption capacity. Also $1/n$ represents the adsorption intensity. The value of $1/n$ reveals ($0.1 < 1/n < 0.5$) indicates that the adsorption process is either favorable or ($1/n > 2$) unfavorable.

Evaluation of the rate of *As* adsorption by PTh employs pseudo first-order and second-order kinetic models. The pseudo-first order is shown in Eq. (6).

$$\ln(q_e - q_t) = \ln q_e - K_1 t \quad (6)$$

where q_t is the adsorption capacity (mg/g) at time t , and K_1 (min^{-1}) is the equilibrium rate constant.

Pseudo 2nd order rate equation is represented by Eq. (7).

$$\frac{1}{q_e} = \frac{1}{K_2 q_e^2} + \frac{1}{q_e} \quad (7)$$

The equilibrium rate constants are K_2 ($\text{g mg}^{-1} \text{min}^{-1}$). R^2 values for linear coefficient regression are utilized to predict the isotherm and kinetic model that best describes the adsorption process.

Thermodynamic characteristics such as entropy change (ΔS), enthalpy changes (ΔH), and the Gibbs free energy changes (ΔG) are critical in determining industrial uses of adsorbents. The ΔG° is a crucial thermodynamic parameter that determines adsorbent's properties throughout the adsorption process. The following formulae were used to evaluate these thermodynamic parameters (Eqs. 8–10).

$$K_T = \frac{q_e}{C_e} \quad (8)$$

$$\ln K_T = \frac{\Delta S^\circ}{R} + \frac{\Delta H^\circ}{RT} \quad (9)$$

$$\Delta G^\circ = \Delta H^\circ - T\Delta S^\circ \quad (10)$$

where R denotes the ideal gas constant, T is the temperature in Kelvins, and K_T denotes the thermodynamic equilibrium constant.

3 Characterization

3.1 FTIR Analysis

The chemical structure of the produced products was evaluated using FTIR spectroscopy (Fig. 1). For pure PTh, absorption peaks appeared at 694 cm^{-1} and 789 cm^{-1} corresponding to C-H ring deformation and C-S stretching respectively. The absorption peak at 1122 cm^{-1} and 1032 cm^{-1} both corresponds to C-H in plane deformation. The absorption peaks at 1417 cm^{-1} and 1640 cm^{-1} may be assigned to C=C ring stretching and C=C ring vibration respectively. Absorption peaks for C-H aromatic stretching and C-H alkene stretching were found at 2919 cm^{-1} and 2836 cm^{-1} respectively (Arabahmadi & Ghorbani,

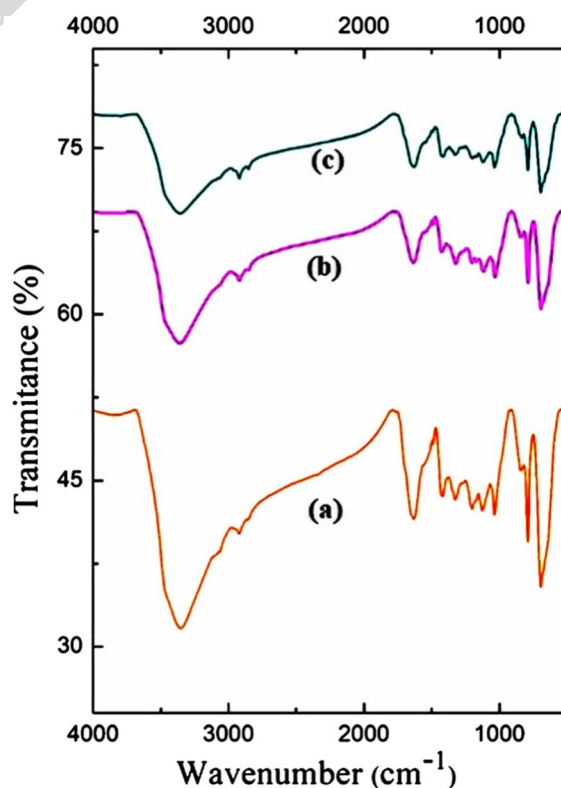


Fig. 1 FTIR plot for a pristine PTh, b PTh after adsorption of *As* (V), and c PTh after adsorption of *As* (III)

AQ4

286 2017a; Singh et al., 2021). FTIR spectra for PTh after
287 adsorption of As (III) and As (V) were also recorded.
288 The spectrum shows that there is no significant
289 change in position of the peaks and similar to the
290 peaks earlier found for pure PTh. This signifies the
291 high stability of PTh even after treating with As con-
292 taminated water.

293 3.2 XRD Analysis

294 The X-ray diffraction (XRD) studies of the prepared
295 PTh and PTh after adsorption of As (III) and As (V)
296 were carried out in the 2θ range from 10 to 80° . A
297 typical XRD pattern for all three samples is shown
298 in Fig. 2. For all the three samples, peaks were
299 observed at about $2\theta = 24^\circ, 33^\circ, 35^\circ,$ and 40° which
300 are characteristic peak of conducting amorphous

PTh (Sakthivel & Boopathi, 2014). Similar peaks 301
were found at similar 2θ value for PTh after adsorp- 302
tion of As (III) and As (V) which signifies that there 303
is no change in the structure of PTh after adsorption 304
of As (III) and As (V). 305

3.3 SEM Analysis 306

The SEM image of pristine PTh (Fig. 3a) shows a 307
randomly aggregated granular structure of a few 308
micrometers and this granular morphology vanishes 309
and a smooth surface with porous structure mor- 310
phology is observed after adsorption of As (III) and 311
As (V) indicating the successful loading of As on the 312
surface of PTh (Fig. 3b and c). 313

The energy-dispersive X-ray (EDX) spectroscopy 314
(Fig. 4) shows us the presence of S and C 315

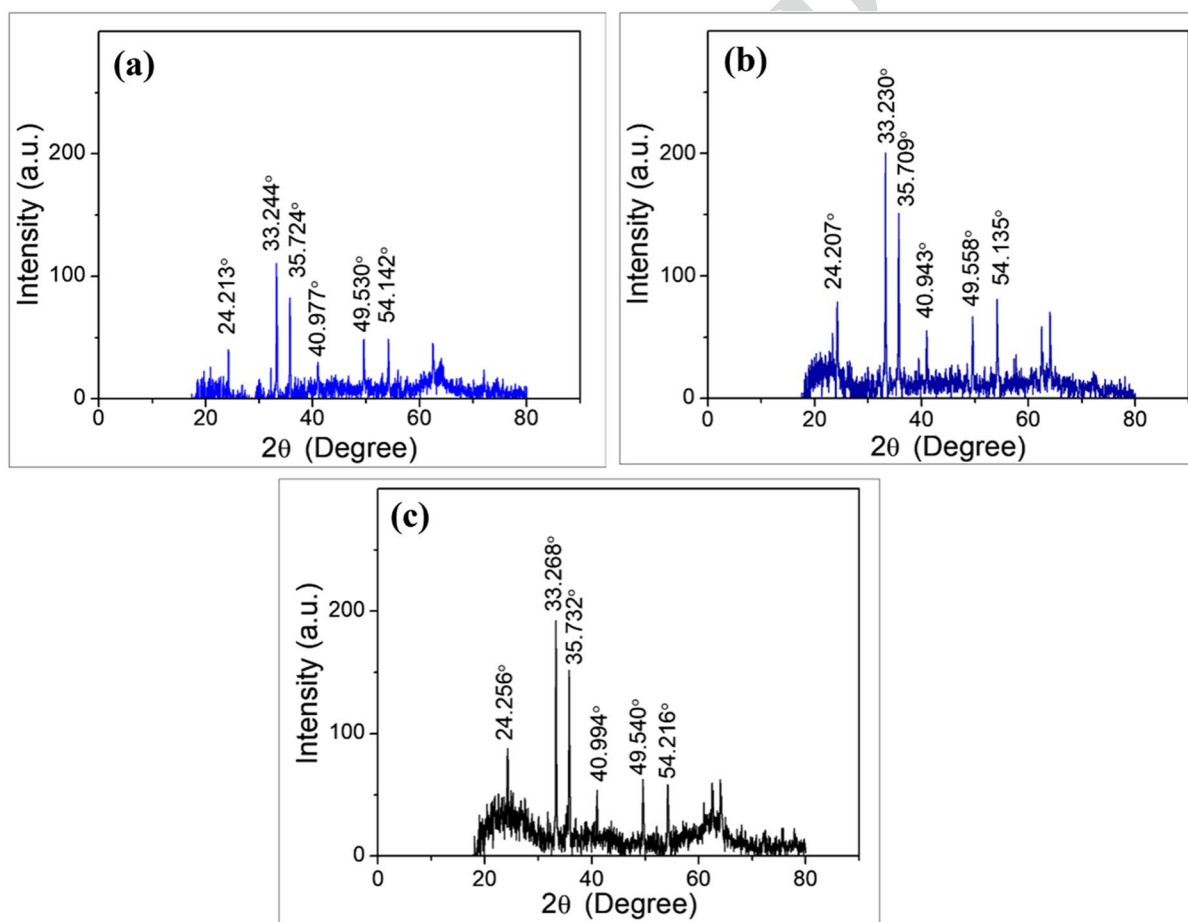


Fig. 2 XRD analysis of **a** pure PTh before adsorption, **b** PTh after adsorption of As (III), and **c** PTh after adsorption of As (V)

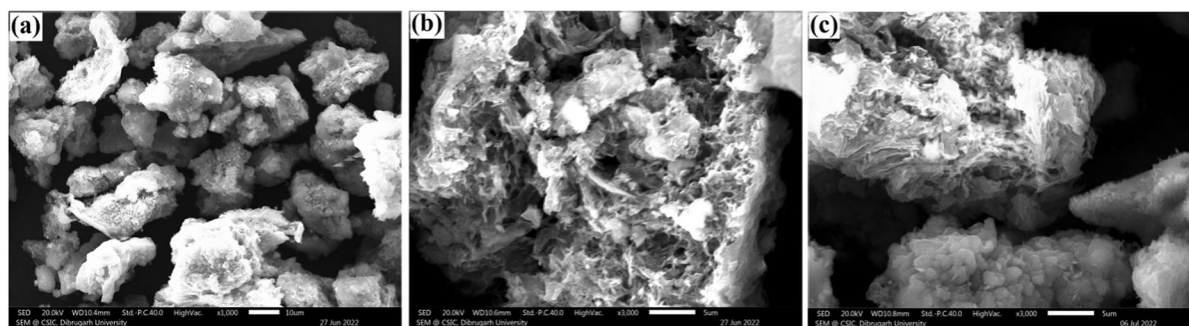


Fig. 3 SEM image of a pure PTh, b As (III) loaded PTh, and c As(V) loaded PTh

AQ5

316 which are the constituents of PTh structure. Also,
 317 the presence of Fe and Cl indicates that excess of
 318 FeCl₃ has been used as oxidant for the preparation
 319 of PTh and that Cl present in polymeric structure
 320 as counter ion to maintain electrical neutrality. In
 321 Fig. 4(b) and (c), peaks for As are found, which
 322 confirms the adsorption of As by PTh surface.

323 4 Results and Discussion

324 4.1 Effect of Adsorbent Dose

325 The amount of the adsorbent indicates its capac-
 326 ity to adsorb any heavy metal ion under experi-
 327 mental conditions, making it a crucial parameter
 328 in the removal of heavy metal ions from aqueous
 329 solutions. To carry out this experiment, different
 330 amounts of PTh (0.2 g/L, 0.5 g/L, 0.8 g/L, 1.0
 331 g/L, and 2 g/L) were used for As removal from
 332 the solution. The concentration of As was fixed
 333 (500 µg/L) and pH of the solution was maintained
 334 at 7 by addition of 0.1 M HCl and 0.1 M NaOH
 335 solution. Replicate test has been carried out for
 336 three times and average percentage removal is
 337 plotted against adsorbent dose with error bar of
 338 standard deviation. From Fig. 5, it is clearly seen
 339 that percentage removal increases with increase
 340 in adsorbent dose which may be due to increase
 341 in binding sites with increase in adsorbent dose
 342 (Yang et al., 2022b; Yang et al., 2023b; Yang
 343 et al., 2019). The adsorbent amount 1.0 g/L and

2.0 g/L possess almost same removal efficiency 344
 for both As species; therefore, we have consid- 345
 ered 1.0 g/L as optimum adsorbent dose and 1.0 346
 g/L of PTh can effectively remove both As spe- 347
 cies with removal percentage of 92.4% and 95.4% 348
 for As (III) and As (V) respectively. 349

4.2 Effect of Initial As Concentration 350

To investigate the effect of initial As concentration, a 351
 batch experiment was performed using a fixed dosage 352
 of 1 g/L of adsorbent at varying initial As (V) and As 353
 (III) concentrations of 100 µg/L, 300 µg/L, 500 µg/L, 354
 700 µg/L, and 1000 µg/L. The experiments were con- 355
 ducted with a fixed solution volume (100 mL), pH 356
 was maintained at 7 by the addition of 0.1 M HCl 357
 and 0.1 M NaOH solution, and a contact time of 24 358
 h replicate tests were conducted for three times and 359
 average percentage removal is plotted against initial 360
 As concentration with error bar of standard deviation. 361
 Figure 6 clearly shows that as the initial concentration 362
 increased, the removal of As decreased. The observed 363
 continuous reduction in the percentage removal of As 364
 (III) and As (V) with adsorbate loadings might result 365
 in the saturation of the adsorbent's binding sites. At 366
 higher concentrations, this might also be ascribed to 367
 the adsorbent active site saturation. For both As (III) 368
 and As (V) 100%, the removal efficiency was obtained 369
 when initial As concentration was 100 µg/L. For As 370
 (V), when initial As concentration was 300 µg/L, after 371
 adsorption equilibrium, the residual concentration 372
 was reduced to 9.0 µg/L, which is as low as recom- 373
 mended by the WHO. 374

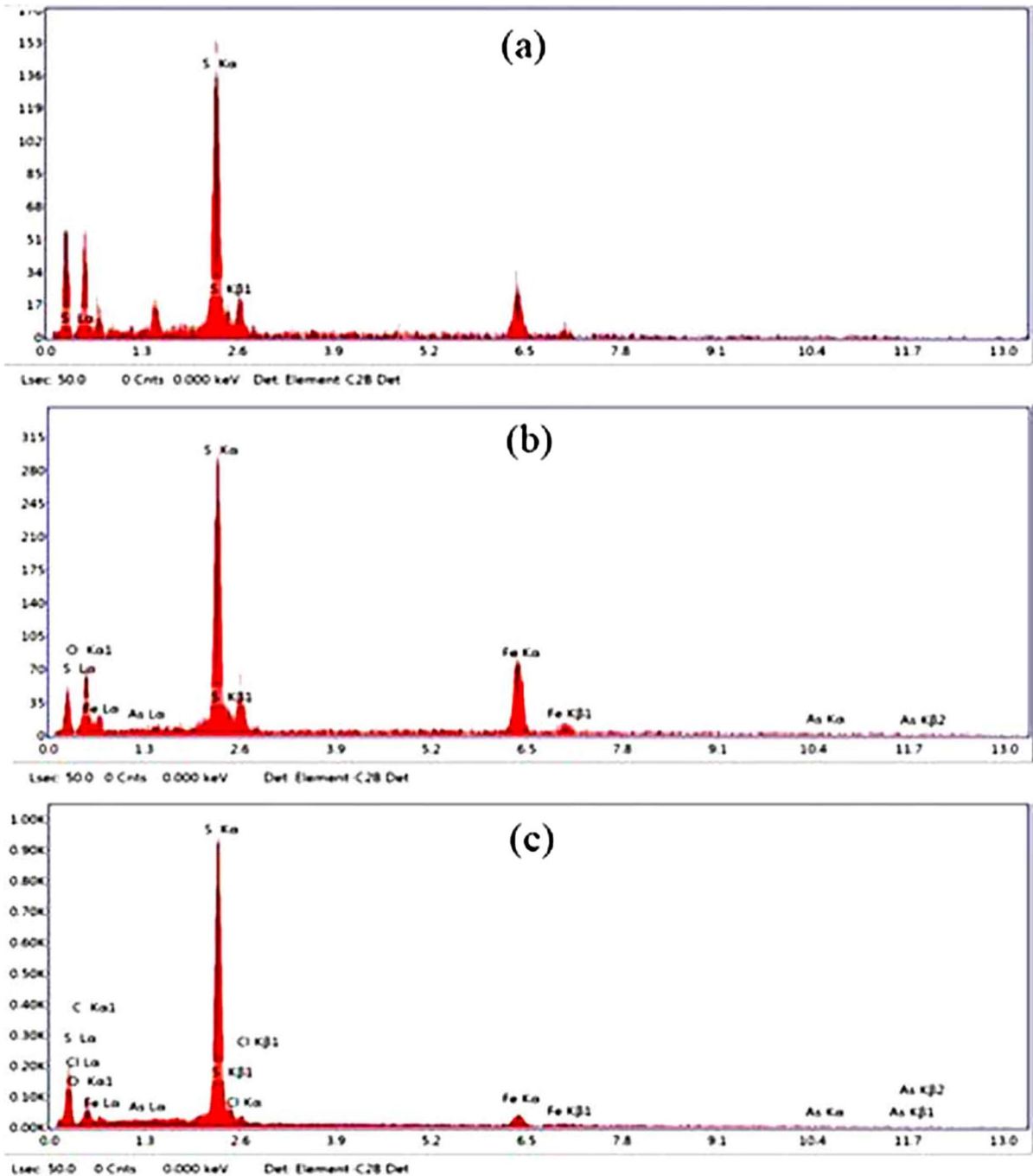


Fig. 4 EDX spectra for **a** PTh, **b** As (V) loaded PTh, and **c** As (III) loaded PTh

375 4.3 Effect of pH of Solution

376 The impact of pH on As (V) and As (III) adsorp-
 377 tion by PTh was investigated by altering the solu-
 378 tion pH from 3.0 to 10.0. The pH of the solutions

was adjusted using 0.1 M HCl or 0.1 M NaOH, 379
 and the starting concentrations of As (V) and As 380
 (III) were set at 100 µg/L. Other parameter such 381
 as adsorbent dose (1.0 g/L), contact time (24 h), 382
 and solution volume was taken as constant. From 383

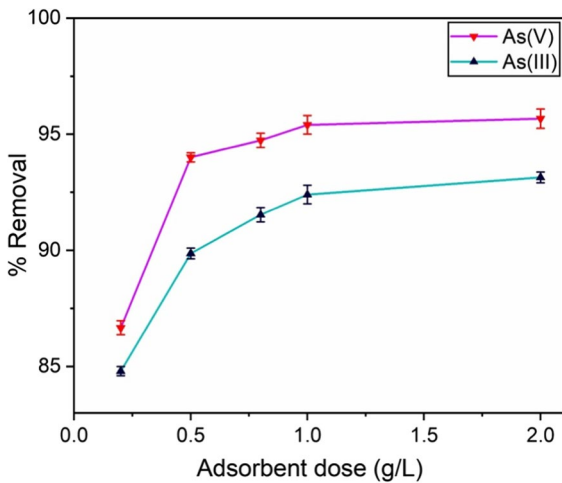


Fig. 5 Plot of % removal of *As* (V) and *As* (III) vs. adsorbent dose in g/L at pH 7

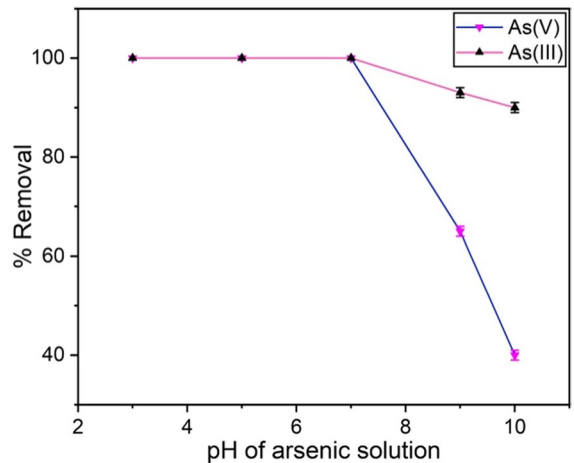


Fig. 7 Effect of initial solution pH on the removal of *As* (V) and *As* (III) (initial *As* concentration = 100 µg/L, adsorbent dose = 1.0 g/L)

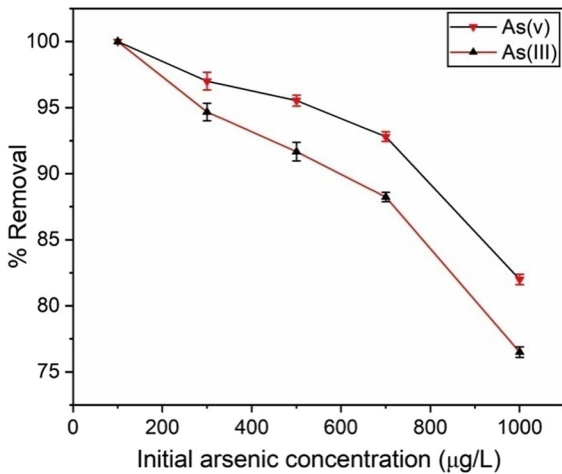


Fig. 6 Plot of % removal of *As* (V) and *As* (III) against initial *As* concentration in µg/L at pH = 7

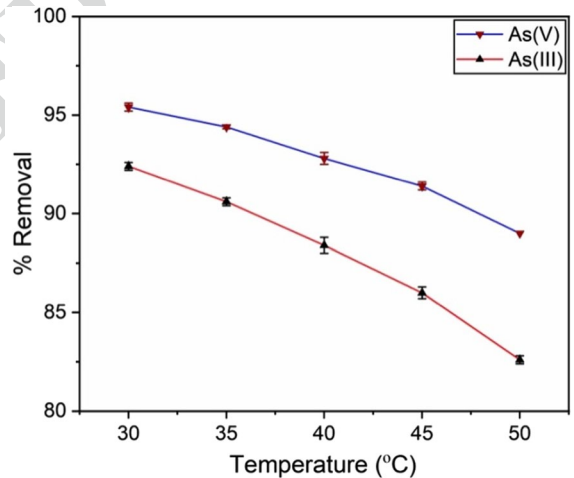


Fig. 8 Effect of temperature on *As* removal (initial *As* concentration = 500 µg/L, adsorbent dose = 1.0 g/L)

384 Fig. 7, it is clearly seen that for both *As* (III) and
 385 *As* (V), % removal decreases after pH 7. Until pH
 386 7, 100% removal was obtained for both *As* (V)
 387 and *As* (III). The electrical charge on the adsorbent
 388 surface and adsorbed ions vary when the pH
 389 of the solution changes. In other words, adsorbent
 390 surface properties are extremely pH-dependent
 391 (Arabahmadi & Ghorbani, 2017b). PTh possesses
 392 positive zeta potential at lower pH (pH < 8.5)
 393 and exhibits negative zeta potential at higher pH
 394 (pH > 8.5) (Murugavel & Malathi, 2016).

In the acidic pH range, the most prevalent *As* (V) species are $H_2AsO_4^-$ and $HAsO_4^{2-}$; therefore, at lower pH, these negative ions quickly adsorbed on positive surface of PTh, showing greater adsorption in lower pH range. But at higher pH (> 7), PTh surface gets negatively charged resulting rapid decline in removal at higher pH due to repulsion between negatively charged surface of PTh and negative adsorbate. H_3AsO_3 is the main species of *As* (III) which dissociates into negative species after pH 9.2. Therefore, for *As* (III), a decrease in removal percentage was observed at higher pH.

406 4.4 Effect of Temperature

407 To study the effect of temperature on As removal, we
 408 varied the temperature in the range of 30-50 °C dur-
 409 ing adsorption and (Fig. 8). The adsorption process at
 410 varying temperatures was carried out at constant pH
 411 (pH = 7), constant adsorbent dose (1 g/L), constant
 412 contact time (24 h), and constant initial As concentra-
 413 tion ($C_i = 500 \mu\text{g/L}$). All these experiments were rep-
 414 licated for three times with error bar of standard devi-
 415 ation. With the increase in temperature, % removal
 416 decreases for both As (III) (from 92.4 to 82.6%) and
 417 As(V) (from 95.4 to 89%). Table 1 shows the calcu-
 418 lated values for the thermodynamic parameters for
 419 the As sorption process. The values of ΔH° , ΔS° , and
 420 ΔG° were calculated from Vant Hoff's plot (Fig. 9).
 421 The negative ΔH° value implies that As sorption onto
 422 PTh is exothermic; thus, the lower temperature pro-
 423 motes the process. The negative values of ΔS° indi-
 424 cated that no major change occurred in the adsor-
 425 bent's internal structures during adsorption. Finally,
 426 the negative ΔG° at all temperatures indicates the
 427 spontaneous character of the adsorption (Nyamunda
 428 et al., 2019; Karimi et al., 2019).

429 4.5 Effect of Co-Existing Anion

430 A natural water system contains a wide range of
 431 different types of compounds and in particular, the
 432 presence of different anions may impact the adsorp-
 433 tion of arsenate and arsenite on a material. As a
 434 result, we choose some typical anions in water and
 435 investigated how they affected the adsorption of As.
 436 The effects of excess anions on the adsorption of

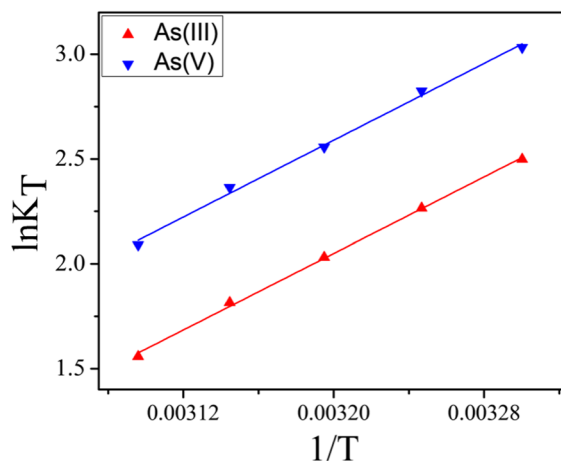


Fig. 9 Vant Hoff's plot for As removal

arsenate on materials were examined and the PO₄³⁻, SO₄²⁻, and CO₃²⁻ ions were chosen as coexisting ions and all the tests were replicated for three times. Figure 10 makes it abundantly evident that neither the sulfate ion nor the carbonate ion has a large impact on the adsorption of As by PTh. Phosphate has significantly reduced the As removal efficiency from 95.4 to 87 % and 92.4 to 82% for As (V) and As (III) respectively. When PO₄³⁻ is present, it competes with As ions for the adsorption sites of the adsorbent. This is because, PO₄³⁻ has similarities with As anions in structure as phosphorus and As are located at the same group of the periodic table (Bae et al., 2020). Therefore, we got a significant decline in percentage removal when PO₄³⁻ present as coexisting anion in As solution (Fig. 10).

Table 1 Values of different thermodynamic parameters

Adsorbent	Adsorbate	Tempera- ture (°C)	R ²	ΔH° KJmol ⁻¹	ΔS° Jmol ⁻¹	ΔG° KJmol ⁻¹
PTh	As (III)	30	0.99778	-37.9235	-104.317	-6.2927
		35				-5.8019
		40				-5.2848
		45				-4.7993
		50				-4.1826
	As (V)	30	0.99496	-38.1209	-100.4584	-7.6380
		35				-7.2334
		40				-6.6523
		45				-6.2486
		50				-5.6145

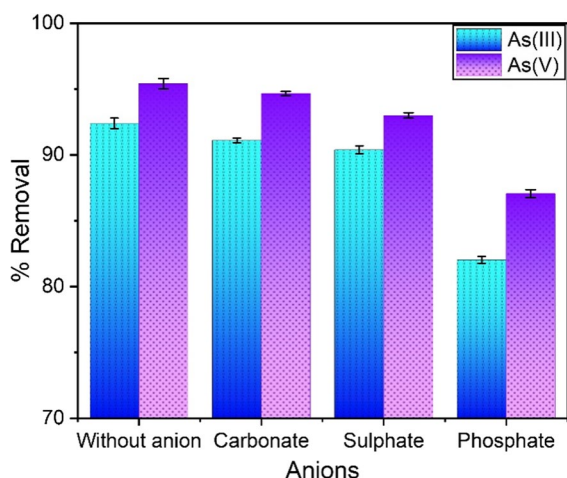


Fig. 10 Effect of co-existing anions on As adsorption [adsorbent dose = 1.0 g/L, As concentration = 500 µg/L, anion concentration = 500 µg/L, contact time = 24 h]

453 4.6 Adsorption Kinetics

454 To study the kinetics of adsorption of As by PTh,
 455 batch experiments were carried out at different
 456 time intervals (1 h, 3 h, 6 h, 12 h, and 24 h) keep-
 457 ing other parameters constant. In order to deter-
 458 mine the kinetic parameter for As adsorption on
 459 PTh, pseudo 1st order and pseudo 2nd order models
 460 were utilized. Figure 11 displays the fitting of two
 461 kinetic models to the As (III) and As (V) equilibrium
 462 data and Table 2 displays the findings of the corre-
 463 sponding kinetic parameters. Because it displayed
 464 a greater value of the linear regression coefficient
 465 when compared to the pseudo 1st order model, it
 466 was found that a pseudo 2nd order kinetics was the
 467 best-fitted model for describing the kinetics of As
 468 (III) and As (V) adsorption by PTh. The pseudo 2nd-
 469 order kinetic model is more favorable since there
 470 is a logical consistency between the calculated and
 471 experimental adsorption capacity (q_e) values.

472 4.7 Adsorption Isotherm

473 An adsorption isotherm gives important information
 474 on adsorption capacity, binding affinity, and the sur-
 475 face properties of the adsorbent, which aids in under-
 476 standing the adsorbate-adsorbent binding mechanism.
 477 In this work, the adsorption behavior of PTh for As
 478 (III) and As (V) adsorption was investigated using two

theoretical models, Langmuir and Freundlich's iso-
 479 therms, as demonstrated in Fig. 12. 480

481 Freundlich's isotherm supports the idea that
 482 adsorption happens on the heterogeneous surface of
 483 the adsorbent, whereas Langmuir's isotherm explains
 484 the monolayer adsorption of contaminants onto the
 485 adsorbent's surface having a finite number of adsorp-
 486 tion sites. The findings in Table 3 show that Lang-
 487 muir's isotherm was the most closely matched since
 488 its linear regression [$R^2 = 0.9934$ for As (III) and
 489 0.9977 for As (V)] coefficient was found to be greater
 490 than that of Freundlich's adsorption isotherm [$R^2 =$
 491 0.93656 for As (III) and 0.91679 for As (V)]. Lang-
 492 muir's adsorption model confirms the monolayer
 493 adsorption of As species on PTh. The maximum
 494 adsorption capacity for PTh, calculated from Lang-
 495 muir's adsorption isotherm model, was found to be
 496 84.33 and 87.78 µg/g for As (III) and As (V) removal
 497 respectively. The separation factor (R_L) values for
 498 both As (III) and As (V) are below one, favoring the
 499 adsorption phenomena.

500 4.8 Adsorption Mechanism

501 Sulfur has a high affinity for As species (Samah et al.,
 502 2020; Fisher et al., 2008; Herath et al., 2019). There-
 503 fore, high removal % of As by PTh is obtained which
 504 may be due to the complex formation between As
 505 species and sulfur atom of PTh chain. Arsenate spe-
 506 cies are negatively charged at a wide range of pH;
 507 therefore, these negatively charged species may get
 508 attached to the positively charged surface of PTh
 509 through electrostatic attraction. The EDX spectra of
 510 PTh after treating with As (III) and As (V) confirm the
 511 presence of As in polymeric structure. This adsorp-
 512 tion process is supported by kinetic model and iso-
 513 therm model.

514 Moreover, chloride ion is present as counter ion in
 515 polymeric structure, which might get exchanged with
 516 negative As species. Similar interaction was shown by
 517 R. Ansari and A. F. Delavar (2010) in case of poly
 518 3-methyl thiophene synthesized on sawdust, where
 519 negative Cr (VI) species ($HCrO_4^-$) got exchanged
 520 with chloride ion present in the polymeric structure
 521 (Ansari & Delavar, 2010). Overall, As adsorption by
 522 PTh may be due to several factors which ultimately
 523 enhances the As adsorption on PTh. Plausible mecha-
 524 nism is depicted in Fig. 13.

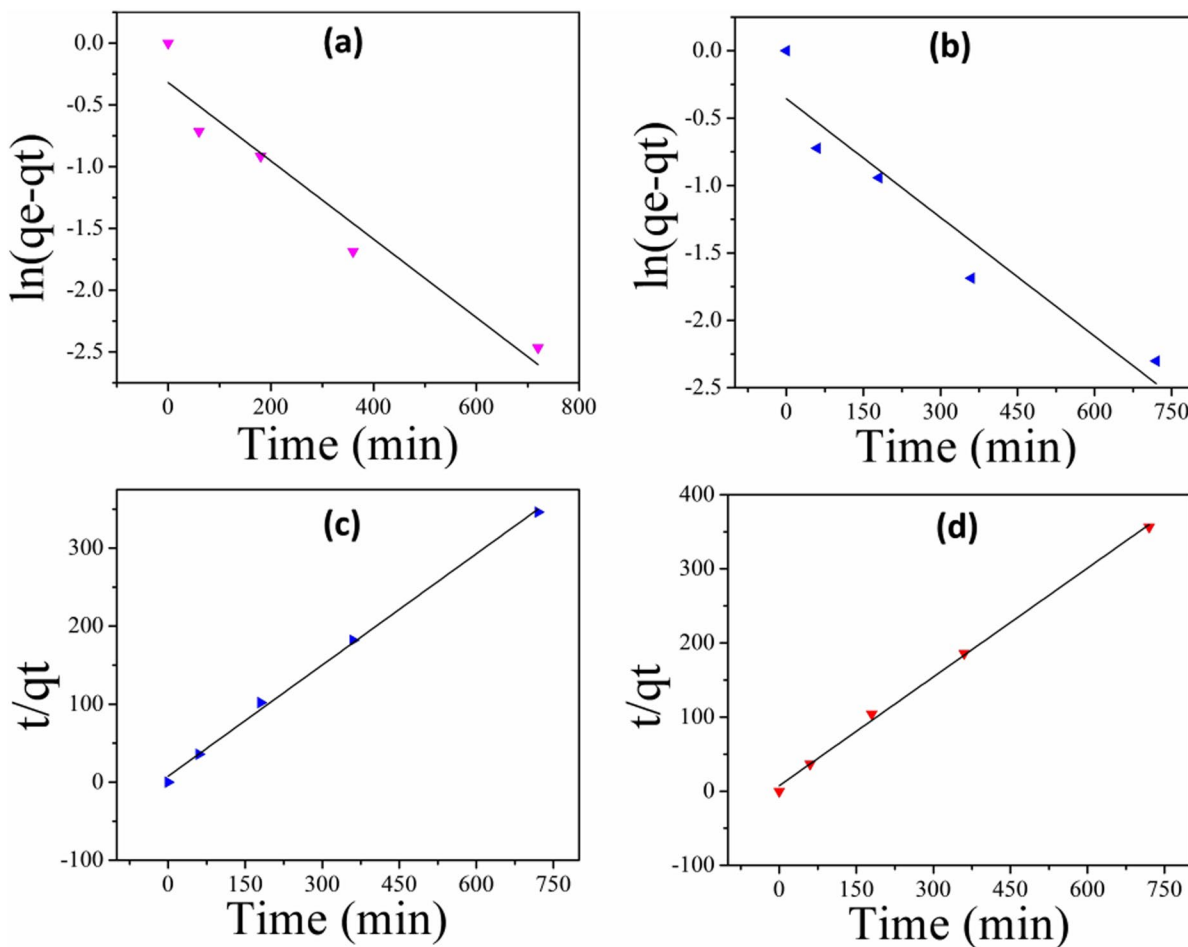


Fig. 11 Pseudo 1st order kinetic model **a** for As (V), **b** for As (III); pseudo 2nd order model **c** for As (V) and **d** for As (III)

Table 2 Kinetic parameters for As (III) and As (V) adsorption on PTh

Order of the reaction	Parameters	As (III)	As (V)
Pseudo 1st order	$q_{e^{exp}}$ (mg/g)	2.12	2.165
	$q_{e^{cal}}$ (mg/g)	0.700613	0.726469
	K_1 (min^{-1})	-4.1×10^{-6}	-4.4×10^{-6}
	R^2	0.8862	0.9203
	Pseudo 2nd order	$q_{e^{exp}}$ (mg/g)	2.12
$q_{e^{cal}}$ (mg/g)		2.043736	2.104554
K_2 ($\text{g mg}^{-1} \text{min}^{-1}$)		0.559101	0.574306
R^2		0.9976	0.9972

525 A further investigation was carried out through
 526 DFT calculations to verify the proposed mecha-
 527 nism of adsorption of As by PTh. The ground state
 528 geometry was optimized using the Kohn-Sham
 529 density functional theory with the B3LYP hybrid

density exchange functional with the 6-311G 530
 basis set. This adiabatic connection method func- 531
 tional includes fractions of exact Hartree-Fock 532
 exchange energy, calculated as a function of the 533
 Kohn-Sham molecular orbitals. Furthermore, the 534

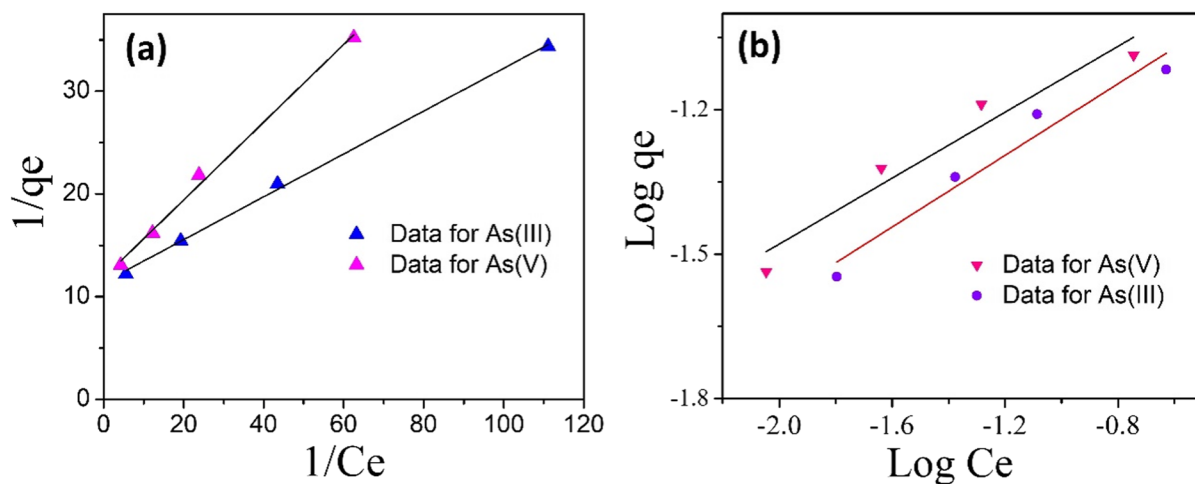


Fig. 12 Adsorption isotherm model for As (III) and As (V), a Langmuir and b Freundlich

Table 3 Adsorption isotherm parameter for the removal of As (III) and As (V) by PTh

Adsorption isotherm model	Parameters	As (III)	As (V)
Langmuir's adsorption isotherm	q_{max} (mg/g)	0.08433	0.08778
	K_L (L/mg)	31.3492	54.6523
	R_L	0.05997	0.0353
	R^2	0.9934	0.9977
	Freundlich's adsorption isotherm model	K_f	0.141706
	$1/n$	0.37169	0.34217
	R^2	0.93656	0.91679

Fig. 13 Plausible mechanism for As adsorption by PTh

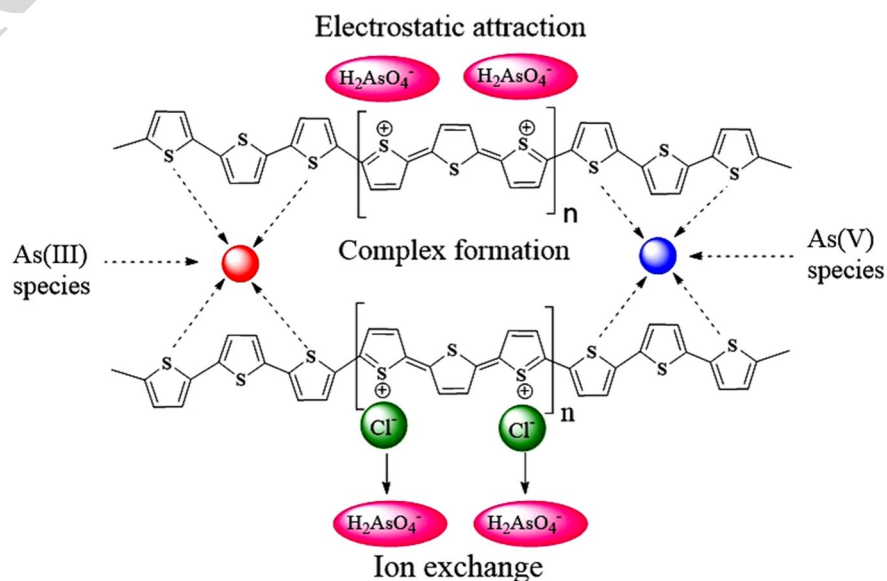
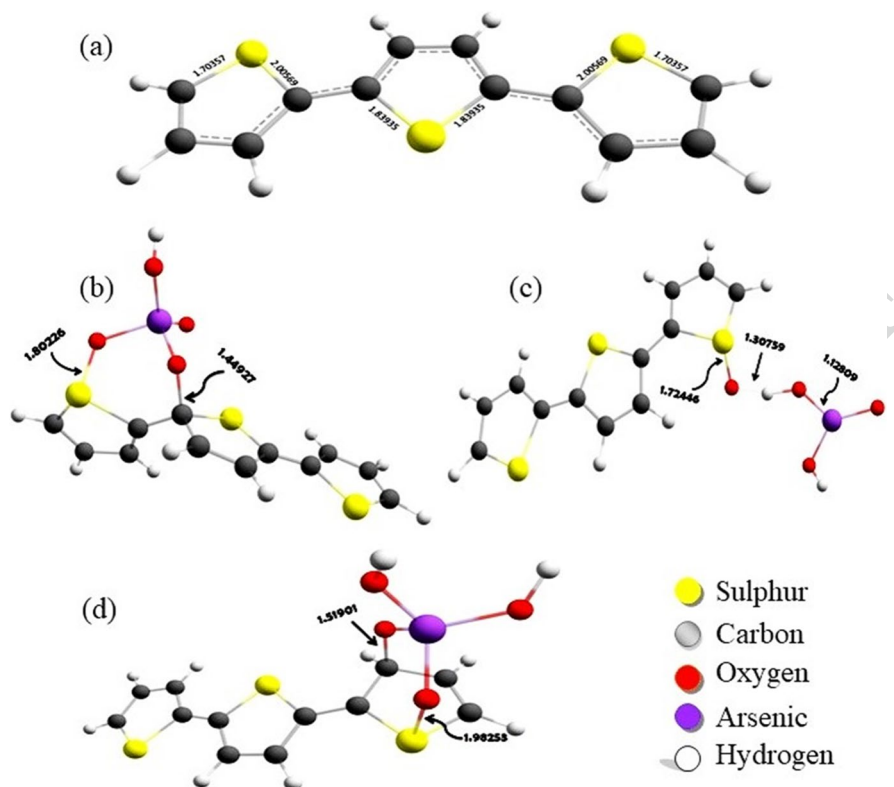


Fig. 14 Optimized structure of **a** polythiophene (+4), **b-c** H_2AsO_4^- adsorbed on the surface of PTh, **d** HAsO_4^{2-} adsorbed on the surface of PTh. (The color code for each element has been shown)



stationary points were then characterized through the computation of vibrational frequencies in the absence of any dispersion factors using the same level of theory. Figure 14a shows the optimized structure of PTh in +4 state with delocalized electrons. The adsorption of H_2AsO_4^- and HAsO_4^{2-} is confirmed from Fig. 14(b), (c), and (d). The optimized geometry of the molecule shows that when H_2AsO_4^- or HAsO_4^{2-} comes in the vicinity of PTh through electrostatic attraction, the positively charged sulfur attracts the negatively charged oxygen. This attraction causes As to be adsorbed by PTh through sulfur–oxygen binding. It can be further observed that there is an existence of Van-der-Waal type of interaction too existing between hydrogen and oxygen molecules. Similar kind of trend can also be showed for As (III). The computational treatment thus verifies the experimental investigation. It also justifies the physicochemical interpretation of the observation texted.

4.9 Reusability Test for the Adsorbent

The regeneration is an essential aspect to make the adsorbent a sustainable and affordable material for water purification applications. Here, 1 g/L of PTh was treated with As (III) and As (V) solution (500 $\mu\text{g/L}$) for 24 h. PTh was then separated and dried in oven for 3 h at 50 °C. Subsequently, the residual concentration was measured. The desorption of As (III) and As (V) adsorbed PTh was done by treating them with 100 mL of 0.1 M NaOH solution at 30 °C for 3 h. The desorbed adsorbents were collected and washed with deionized water for several times. After then, the adsorbents were dried in oven for reuse. Similarly, this process of adsorption and desorption is carried out for five times and for each time the residual As concentration is evaluated. From Fig. 15, it is seen that the percentage removal decreases with repetition of adsorption and desorption cycle. For As (V), the percentage removal decreases as 95.4 to 65 %

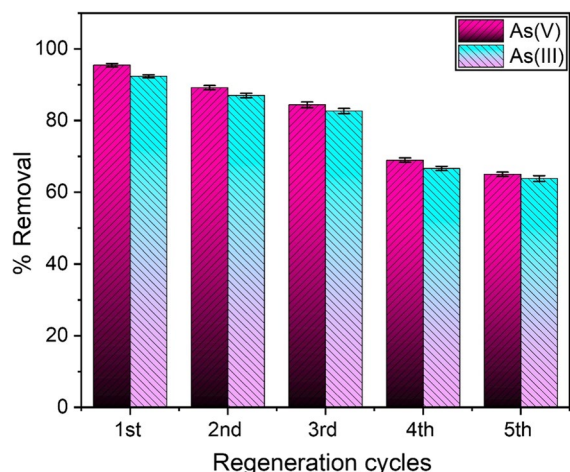


Fig. 15 Reusability of PTh [As concentration = 500 µg/L, adsorbent dose = 1 g/L, contact time = 24 h, pH =7]

574 from the 1st to 5th cycle respectively. For As (III), the
 575 percentage removal decreases as 92.4 to 63.8% from
 576 the 1st to 5th cycle respectively.

577 **5 Conclusion**

578 We have successfully synthesized PTh through oxida-
 579 tive polymerization using ferric chloride as an
 580 oxidant and studied for the removal of arsenic from
 581 aquatic solutions. The % removal of As by PTh
 582 increases with increase in adsorbent dose from 0.2 to
 583 1 g/L and maximum adsorption was found to be up to
 584 92.4% and 95.4% for As (III) and As (V) respectively.
 585 PTh showed 100% removal efficiency for both As
 586 (III) and As (V) when the initial As concentration was
 587 100 µg/L, although the % of As removal decreases
 588 gradually on decreasing the initial As concentration.
 589 The maximum arsenic removal (100 % removal) was
 590 obtained at acidic and neutral pH and % removal
 591 decreases after pH 7. The spontaneous nature of the
 592 adsorption of As by PTh is indicated by the nega-
 593 tive ΔG° at all experimental temperatures and lower
 594 temperature favors the adsorption since the negative
 595 ΔH° value suggests that As sorption onto PTh is an
 596 exothermic process. The presence of common ions,
 597 viz., SO_4^{2-} and CO_3^{2-} , have negligible effect on As
 598 adsorption while PO_4^{3-} ion showed a significant
 599 effect on As adsorption by PTh since PO_4^{3-} competes
 600 with As anions for binding sites. The adsorption of

As on PTh was fitted well to the pseudo-2nd-order
 kinetic model with the experimental data and obeyed
 Langmuir’s adsorption isotherm model indicating
 the monolayer adsorption of the adsorbents. The
 hypothesized mechanism for the adsorption of As by
 PTh was further investigated using DFT simulations
 and found that the positively charged sulfur of PTh
 attracts the negatively charged oxygen of $H_2AsO_4^-$ or
 $HAsO_4^{2-}$ through electrostatic attraction. DFT calcu-
 lation also revealed that hydrogen and oxygen mol-
 ecules interact in a way similar to Van-der-Waal inter-
 actions which enhance the adsorption of As on PTh.
 Due to its high absorption capacity, effective As
 removal efficiency, easy synthesis, high stability, and
 cost-effectiveness, PTh could be considered large-
 scale filtrate adsorbent for the removal of arsenic
 from the aqueous solution.

Data Availability The authors can confirm that all relevant
 data are included in the article and/or its supplementary infor-
 mation files.

Declarations

Conflict of Interest The authors declare no competing inter-
 ests.

References

Alam, M. M., Rashed, M. A., Rahman, M. M., Rahman, M.
 M., Nagao, Y., & Hasnat, M. A. (2018). Electrochemical
 oxidation of As (III) on Pd immobilized Pt surface: kine-
 tics and sensing performance. *RSC Advances*, 8(15), 8071–
 8079. <https://doi.org/10.1039/C7RA12576C>
 Ansari, R., & Delavar, A. F. (2010). Removal of Cr (VI) ions
 from aqueous solutions using poly 3-methyl thiophene
 conducting electroactive polymers. *Journal of Polymers
 and the Environment*, 18, 202–207. <https://doi.org/10.1007/s10924-010-0199-7>
 Arabahmadi, V., & Ghorbani, M. (2017a). Pb (II) removal
 from water using surface-modified polythiophene-coated
 rice husk ash nanocomposite. *Inorganic and Nano-Metal
 Chemistry*, 47(12), 1614–1624. <https://doi.org/10.1080/24701556.2017.1357589>
 Arabahmadi, V., & Ghorbani, M. (2017b). Pb (II) removal
 from water using surface-modified polythiophene-coated
 rice husk ash nanocomposite. *Inorganic and Nano-Metal
 Chemistry*, 47(12), 1614–1624. <https://doi.org/10.1080/24701556.2017.1357589>
 Assaad, N., Sabeh, G., & Hmadeh, M. (2020). Defect control
 in Zr-based metal–organic framework nanoparticles for
 arsenic removal from water. *ACS Applied Nano Materials*,
 3(9), 8997–9008. <https://doi.org/10.1021/acsanm.0c01696>

- 650 Bae, J., Kim, S., Kim, K. S., Hwang, H. K., & Choi, H. (2020).
651 Adsorptive removal of arsenic by mesoporous iron oxide
652 in aquatic systems. *Water*, 12(11), 3147. <https://doi.org/10.3390/w12113147>
- 653 Bordoloi, S., Chetia, R., Borah, G., & Konwer, S. (2022).
654 Removal of As (III) and As (V) from water using reduced
655 GO-Fe⁰ filled PANI composite. *Journal of Applied Water
656 Engineering and Research*, 10(2), 117–128. [https://doi.
657 org/10.1080/23249676.2021.1948361](https://doi.org/10.1080/23249676.2021.1948361)
- 658 Cho, K., Shin, B. Y., Park, H. K., Cha, B. G., & Kim, J. (2014).
659 Size-controlled synthesis of uniform akaganeite nanorods
660 and their encapsulation in alginate microbeads for arsenic
661 removal. *RSC Advances*, 4(42), 21777–21781. [https://doi.
662 org/10.1039/C4RA01998A](https://doi.org/10.1039/C4RA01998A)
- 663 Cooper, A. M., Hristovski, K. D., Möller, T., Westerhoff, P., &
664 Sylvester, P. (2010). The effect of carbon type on arsenic
665 and trichloroethylene removal capabilities of iron (hydr)
666 oxide nanoparticle-impregnated granulated activated carbons.
667 *Journal of Hazardous Materials*, 183(1-3), 381–
668 388. <https://doi.org/10.1016/j.jhazmat.2010.07.036>
- 669 Dutta, K., & Rana, D. (2019). Polythiophenes: An emerging
670 class of promising water purifying materials. *European
671 Polymer Journal*, 116, 370–385. [https://doi.org/10.1016/j.
672 eurpolymj.2019.04.033](https://doi.org/10.1016/j.eurpolymj.2019.04.033)
- 673 Dutta, S., Manna, K., Srivastava, S. K., Gupta, A. K., & Yadav,
674 M. K. (2020). Hollow polyaniline microsphere/Fe₃O₄
675 nanocomposite as an effective adsorbent for removal of
676 arsenic from water. *Scientific Reports*, 10(1), 4982. [https://
677 doi.org/10.1038/s41598-020-61763-z](https://doi.org/10.1038/s41598-020-61763-z)
- 678 Fan, C. S., Tseng, S. C., Li, K. C., & Hou, C. H. (2016). Elec-
679 tro-removal of arsenic (III) and arsenic (V) from aqueous
680 solutions by capacitive deionization. *Journal of Hazard-
681 ous Materials*, 312, 208–215. [https://doi.org/10.1016/j.
682 jhazmat.2016.03.055](https://doi.org/10.1016/j.jhazmat.2016.03.055)
- 683 Fisher, J. C., Wallschläger, D., Planer-Friedrich, B., & Hol-
684 libaugh, J. T. (2008). A new role for sulfur in arsenic
685 cycling. *Environmental Science & Technology*, 42(1),
686 81–85. <https://doi.org/10.1021/es0713936>
- 687 Gupta, A., Yunus, M., & Sankaramakrishnan, N. (2013).
688 Chitosan-and iron-chitosan-coated sand filters: A cost-
689 effective approach for enhanced arsenic removal. *Indus-
690 trial & Engineering Chemistry Research*, 52(5), 2066–
691 2072. <https://doi.org/10.1021/ie302428z>
- 692 Herath, I., Bundschuh, J., & Bhattacharya, P. (2019). Sulfur-
693 arsenic interactions and formation of thioarsenic com-
694 plexes in the environment. In Y. Zhu, H. Guo, P. Bhat-
695 tacharya, A. Ahmad, J. Bundschuh & R. Naidu (Eds.),
696 *Environmental arsenic in a changing world* (pp. 210–211).
697 CRC Press. <https://doi.org/10.1201/9781351046633>
- 698 Horzum, N., Demir, M. M., Nairat, M., & Shahwan, T. (2013). Chi-
699 tosan fiber-supported zero-valent iron nanoparticles as a novel
700 sorbent for sequestration of inorganic arsenic. *RSC Advances*,
701 3(21), 7828–7837. <https://doi.org/10.1039/C3RA23454A>
- 702 Karegar, M., & Khodaei, M. M. (2022). The modified polythio-
703 phene-Cu NPs composites for Pb (II) ions removal from
704 aqueous solution. *Journal of Applied Polymer Science*,
705 139(2), 51489. <https://doi.org/10.1002/app.51489>
- 706 Karimi, P., Javanshir, S., Sayadi, M. H., & Arabyarmoham-
707 madi, H. (2019). Arsenic removal from mining efflu-
708 ents using plant-mediated, green-synthesized iron
709 nanoparticles. *Processes*, 7(10), 759. [https://doi.org/10.
710 3390/pr7100759](https://doi.org/10.3390/pr7100759)
- 711 Leaper, S., Avendaño Cáceres, E. O., Luque-Alled, J. M.,
712 Cartmell, S. H., & Gorgojo, P. (2021). POSS-function-
713 alized graphene oxide/PVDF electrospun membranes
714 for complete arsenic removal using membrane distilla-
715 tion. *ACS Applied Polymer Materials*, 3(4), 1854–1865.
716 <https://doi.org/10.1021/acsapm.0c01402>
- 717 Makavipour, F., Pashley, R. M., & Rahman, A. M. (2019).
718 Low-level arsenic removal from drinking water. *Global
719 Challenges*, 3(3), 1700047. [https://doi.org/10.1002/
720 gch2.201700047](https://doi.org/10.1002/gch2.201700047)
- 721 Mandal, B. K., & Suzuki, K. T. (2002). Arsenic round the
722 world: A review. *Talanta*, 58(1), 201–235. [https://doi.
723 org/10.1016/S0039-9140\(02\)00268-0](https://doi.org/10.1016/S0039-9140(02)00268-0)
- 724 Mondal, M. K., & Garg, R. (2017). A comprehensive review
725 on removal of arsenic using activated carbon prepared
726 from easily available waste materials. *Environmental
727 Science and Pollution Research*, 24, 13295–13306.
728 <https://doi.org/10.1007/s11356-017-8842-7>
- 729 Mondal, P., Majumder, C. B., & Mohanty, B. (2006). Labo-
730 ratory based approaches for arsenic remediation from
731 contaminated water: Recent developments. *Journal of
732 Hazardous Materials*, 137(1), 464–479. [https://doi.org/
733 10.1016/j.jhazmat.2006.02.023](https://doi.org/10.1016/j.jhazmat.2006.02.023)
- 734 Murugavel, S., & Malathi, M. (2016). Structural, photoconduc-
735 tivity, and dielectric studies of polythiophene-tin oxide
736 nanocomposites. *Materials Research Bulletin*, 81, 93–100.
737 <https://doi.org/10.1016/j.materresbull.2016.05.004>
- 738 Nyamunda, B. C., Chivhanga, T., Guyo, U., & Chigondo, F.
739 (2019). Removal of Zn (II) and Cu (II) ions from indus-
740 trial wastewaters using magnetic biochar derived from
741 water hyacinth. *Journal of Engineering*, 2019. [https://doi.
742 org/10.1155/2019/5656983](https://doi.org/10.1155/2019/5656983)
- 743 Pathan, S., & Bose, S. (2018). Arsenic removal using “green”
744 renewable feedstock-based hydrogels: Current and future
745 perspectives. *ACS Omega*, 3(5), 5910–5917. [https://doi.
746 org/10.1021/acsomega.8b00236](https://doi.org/10.1021/acsomega.8b00236)
- 747 Paul, S., Das, N., Bhattacharjee, P., Banerjee, M., Das, J. K.,
748 Sarma, N., Sarkar, A., Bandyopadhyay, A. K., Sau, T.
749 J., Basu, S., Banerjee, S., Majumder, P., & Giri, A. K.
750 (2013). Arsenic-induced toxicity and carcinogenicity: A
751 two-wave cross-sectional study in arsenicosis individu-
752 als in West Bengal, India. *Journal of Exposure Science &
753 Environmental Epidemiology*, 23(2), 156–162. [https://doi.
754 org/10.1038/jes.2012.91](https://doi.org/10.1038/jes.2012.91)
- 755 Prucek, R., Tucek, J., Kolařík, J., Filip, J., Marušák, Z.,
756 Sharma, V. K., & Zbořil, R. (2013). Ferrate (VI)-induced
757 arsenite and arsenate removal by in situ structural incor-
758 poration into magnetic iron (III) oxide nanoparticles.
759 *Environmental Science & Technology*, 47(7), 3283–3292.
760 <https://doi.org/10.1021/es3042719>
- 761 Raj, S. K., Sharma, J., & Kulshrestha, V. (2021). Facile synthe-
762 sis of reusable graphene oxide composite magnetic beads
763 for removal of arsenic (III). *SPE Polymers*, 2(1), 74–85.
764 <https://doi.org/10.1002/pls2.10031>
- 765 Ramesan, M. T., & Suhailath, K. (2017). Role of nanoparticles
766 on polymer composites. In R. K. Mishra, S. Thomas, &
767 N. Kalarikkal (Eds.), *Micro and nano fibrillar composites
768 (MFCs and NFCs) from polymer blends* (pp. 301–326).
769

770 Woodhead Publishing. <https://doi.org/10.1016/B978-0->
 771 [08-101991-7.00013-3](https://doi.org/10.1016/B978-0-08-101991-7.00013-3)

772 Sakthivel, S., & Boopathi, A. (2014). Synthesis and prepara- 816
 773 tion of polythiophene thin film by spin coating method. 817
 774 *International Journal of Science and Research (IJSR)*, 818
 775 *141*, 97–100 Retrieved from [https://www.ijrsr.net/conf/](https://www.ijrsr.net/conf/ETPTA/MjJQgRVRQVEeMTQx.pdf)
 776 [ETPTA/MjJQgRVRQVEeMTQx.pdf](https://www.ijrsr.net/conf/ETPTA/MjJQgRVRQVEeMTQx.pdf)

777 Samah, N. A., Rosli, N. A. M., Manap, A. H. A., Aziz, Y. F. 819
 778 A., & Yusoff, M. M. (2020). Synthesis & characterization 820
 779 of ion imprinted polymer for arsenic removal from water: 821
 780 A value addition to the groundwater resources. *Chemical* 822
 781 *Engineering Journal*, *394*, 124900. [https://doi.org/10.](https://doi.org/10.1016/j.cej.2020.124900)
 782 [1016/j.cej.2020.124900](https://doi.org/10.1016/j.cej.2020.124900)

783 Shahryari, T., Vahidipour, F., Chauhan, N. P. S., & Sargazi, G. 823
 784 (2020). Synthesis of a novel Zn-MOF/PVA nanofibrous com- 824
 785 posite as bioorganic material: Design, systematic study and 825
 786 an efficient arsenic removal. *Polymer Engineering & Science*, 826
 787 *60*(11), 2793–2803. <https://doi.org/10.1002/pen.25510>

788 Siddiqui, S. I., & Chaudhry, S. A. (2017). Iron oxide and its 827
 789 modified forms as an adsorbent for arsenic removal: A 828
 790 comprehensive recent advancement. *Process Safety and* 829
 791 *Environmental Protection*, *111*, 592–626. [https://doi.org/](https://doi.org/10.1016/j.psep.2017.08.009)
 792 [10.1016/j.psep.2017.08.009](https://doi.org/10.1016/j.psep.2017.08.009)

793 Singh, R., Bajpai, A. K., & Shrivastava, A. K. (2021). CdSe 830
 794 nanorod-reinforced poly (thiophene) composites in 831
 795 designing energy storage devices: Study of morphology 832
 796 and dielectric behavior. *Polymer Bulletin*, *78*, 115–131. 833
 797 <https://doi.org/10.1007/s00289-020-03104-8>

798 Wen, Z., Dai, C., Zhu, Y., & Zhang, Y. (2015). Arsenate removal 834
 799 from aqueous solutions using magnetic mesoporous iron 835
 800 manganese bimetal oxides. *RSC Advances*, *5*(6), 4058– 836
 801 4068. <https://doi.org/10.1039/C4RA09746G>

802 Wu, X. L., Wang, L., Chen, C. L., Xu, A. W., & Wang, X. K. 837
 803 (2011). Water-dispersible magnetite-graphene-LDH com- 838
 804 posites for efficient arsenate removal. *Journal of Materi- 839
 805 als Chemistry*, *21*(43), 17353–17359. [https://doi.org/10.](https://doi.org/10.1039/C1JM12678D)
 806 [1039/C1JM12678D](https://doi.org/10.1039/C1JM12678D)

807 Yang, X., Shao, X., Tong, J., Zhou, J., Feng, Y., Chen, R., Yang, 840
 808 Q., Han, Y., Yang, X., Wang, L., Ma, X., Fan, Z., Song, Z., 841
 809 Zimmerman, A. R., & Gao, B. (2023a). Removal of aque- 842
 810 ous eriochrome Blue-Black R by novel Na-bentonite/hickory 843
 811 biochar composites. *Separation and Purification Technology*, 844
 812 *123209*. <https://doi.org/10.1016/j.seppur.2023.123209>

813 Yang, X., Wan, Y., Zheng, Y., He, F., Yu, Z., Huang, J., Wang, 845
 814 H., Ok, Y. S., Jiang, Y., & Gao, B. (2019). Surface func- 846
 815 tional groups of carbon-based adsorbents and their roles 847
 in the removal of heavy metals from aqueous solutions: A 848
 critical review. *Chemical Engineering Journal*, *366*, 608– 849
 621. <https://doi.org/10.1016/j.cej.2019.02.119>

Yang, X., Wang, L., Shao, X., Tong, J., Zhou, J., Feng, Y., 850
 Chen, R., Yang, Q., Han, Y., Yang, X., Ding, F., Meng, Q., 851
 Yu, J., Zimmerman, A. R., & Gao, B. (2022b). Character- 852
 istics and aqueous dye removal ability of novel biosorb- 853
 ents derived from acidic and alkaline one-step ball milling 854
 of hickory wood. *Chemosphere*, *309*, 136610. [https://doi.](https://doi.org/10.1016/j.chemosphere.2022.136610)
[org/10.1016/j.chemosphere.2022.136610](https://doi.org/10.1016/j.chemosphere.2022.136610)

Yang, X., Wang, L., Tong, J., Shao, X., Chen, R., Yang, Q., 855
 Li, F., Xue, B., Li, G., Han, Y., Yang, X., Zimmerman, A. 856
 R., & Bin Gao, B. (2022a). Synthesis of hickory biochar 857
 via one-step acidic ball milling: Characteristics and titan 858
 yellow adsorption. *Journal of Cleaner Production*, *338*, 859
 130575. <https://doi.org/10.1016/j.jclepro.2022.130575>

Yang, X., Wang, L., Tong, J., Shao, X., Feng, Y., Zhou, J., Han, 860
 Y., Yang, X., Ding, F., Zhang, J., Li, Q., Li, G., Zimmer- 861
 man, A. R., & Gao, B. (2023b). Alkaline ball-milled pea- 862
 nut-hull biosorbent effectively removes aqueous organic 863
 dyes. *Chemosphere*, *313*, 137410. [https://doi.org/10.](https://doi.org/10.1016/j.chemosphere.2022.137410)
[1016/j.chemosphere.2022.137410](https://doi.org/10.1016/j.chemosphere.2022.137410)

Yohai, L., Mejía, H. G., Procaccini, R., Pellice, S., Kunjali, 864
 K. L., Dutta, J., & Uheida, A. (2019). Nanocomposite 865
 functionalized membranes based on silica nanoparticles 866
 cross-linked to electrospun nanofibrous support for arse- 867
 nic (v) adsorption from contaminated underground water. 868
RSC Advances, *9*(15), 8280–8289. [https://doi.org/10.](https://doi.org/10.1039/C8RA09866B)
[1039/C8RA09866B](https://doi.org/10.1039/C8RA09866B)

Zhang, K., Dwivedi, V., Chi, C., & Wu, J. (2010). Graphene 869
 oxide/ferric hydroxide composites for efficient arsenate 870
 removal from drinking water. *Journal of Hazardous Mate- 871
 rials*, *182*(1-3), 162–168. [https://doi.org/10.1016/j.jhazmat.](https://doi.org/10.1016/j.jhazmat.2010.06.010)
[at.2010.06.010](https://doi.org/10.1016/j.jhazmat.2010.06.010)

Publisher's Note Springer Nature remains neutral with regard to jurisdictional claims in published maps and institutional affiliations.

Springer Nature or its licensor (e.g. a society or other partner) holds exclusive rights to this article under a publishing agreement with the author(s) or other rightsholder(s); author self-archiving of the accepted manuscript version of this article is solely governed by the terms of such publishing agreement and applicable law.

Journal:	11270
Article:	6372

Author Query Form

Please ensure you fill out your response to the queries raised below and return this form along with your corrections

Dear Author

During the process of typesetting your article, the following queries have arisen. Please check your typeset proof carefully against the queries listed below and mark the necessary changes either directly on the proof/online grid or in the 'Author's response' area provided below

Query	Details Required	Author's Response
AQ1	Please check if the Affiliations "1, 2, 3, 4, and 5" are presented correctly.	
AQ2	Please check if the captured keywords are correct.	
AQ3	Please check if the section headings are assigned to appropriate levels.	
AQ4	Please confirm if the author names are presented accurately and in the correct sequence (given name, middle name/initial, family name).	
AQ5	Figures 3, 4, 14 contains poor quality of text in image. Otherwise, please provide replacement figure file.	
AQ6	Reference: Reference [Arabahmadi and Ghorbani, (2017a)] has the same content with Reference [Arabahmadi and Ghorbani, (2017a)]. Can an alternative reference be provided to avoid repetition? If not, please delete the duplicate reference and renumber subsequent references in ascending numerical order.	